Study of hydrogen pellet ablation cloud via spatially resolved spectral measurement

SEGUINEAUD Guilaume

Doctor of Philosophy

Department of Fusion Science
School of Physical Sciences
SOKENDAI (The Graduate University for Advanced Studies)

Study of hydrogen pellet ablation cloud via spatially-resolved spectral measurement

SEGUINEAUD Guillaume

SOKENDAI
The Graduate University for Advanced Studies

Submitted to the **Department of Fusion Science**
in partial fulfillment of the requirements for the degree of

Doctor of Philosophy

2015-2018

Abstract

Spatially-resolved measurements of the ground state neutral density (n_{a}^{1}), the electron density (n_{e}) and the electron temperature (T_{e}) have been conducted in a hydrogen pellet ablation cloud. Spatial-resolution is achieved thanks to the narrow band-shaped field-of-view (FOV) of the optics of the observation system. Some photons emitted by the ablation cloud are collected by the optics and send to a visible spectrometer. Each obtained spectrum can be associated to a slice of the recorded ablation cloud of a certain volume (V_{s}). It is possible to derive the profiles of n_{a}^{1}, n_{e} and T_{e} along the ablation cloud by analyzing the experimental spectra with a spectral model. Results obtained from least-squares fitting show that the profiles behave accordingly to the consensus to the exception of T_{e} which is lower than what is usually expected from an ablation cloud. The present study provides a new approach based on passive spectroscopy to study and understand the internal structure of pellet ablation clouds.

Nowadays, the Magnetic Confinement Fusion (MCF) is considered as a solution to our continuously increasing energetic needs. In MCF devices, plasmas are contained into a magnetic trap and heated to very high temperatures for the so-called nuclear fusion processes to take place. However, from our current understanding, it is also necessary to inject fuel pellets into the plasmas to ensure that the fusion processes occur as optimally as possible. When a pellet interacts with the plasma of a MCF device, it tends to diffuse its content in the region directly surrounding it. This phenomenon referred to as the pellet ablation process and can be quantified into what is referred to as the deposition profile. Under optimal conditions, most of the deposited particles reach the core region of the plasma where the fusion process is supposed to be the most active. However, current estimations of pellets deposition profiles do not predict an optimal delivery to the plasma core of big sized reactor projects such as the International Thermonuclear Experimental Reactor.

Therefore, to improve the potency of the pellet ablation process, it is necessary to understand how it works accurately. While it is possible to get a broad picture of how pellets behave once they are injected into a MCF device, theoretical models and experimental observations have yet to be fully reconciled. This becomes evident when the behavior of pellets is observed at a local scale where the theoretical models struggle to explain what is experimentally observed. This conclusion is especially true in the region of plasma directly surrounding ablating pellets. Ablating pellets and their direct vicinity are com-

monly referred to as ablation cloud or plasmoids. The study of an ablation cloud is easier than the study a pellet because, contrarily to the latter, the former is actually a plasma that emits light. Up until a few years ago, technological advancements only allowed to observe the most intense region of a targeted plasmoid. Thankfully, improvements that have been achieved in terms of higher resolutions and faster acquisition rates made it possible for researchers to have access to the inner structure of ablation clouds and offered the opportunity to challenge some of the commonly accepted theoretical models. Indeed, improvements of the diagnostics apparatus lead the research on plasma fusion in general to go through what could be referred to as a “Local Thermodynamic Equilibrium” plasma crisis. Studies conducted on fuel pellet ablation clouds are not exempt from it. Local Thermodynamic Equilibrium (LTE) is a condition which is often considered in plasmas. The LTE condition contains a set of approximations which allow plasmas to be characterized more easily than if they had to be treated by a more general approach. Some criteria need to be fulfilled in order for the LTE condition to be applied. It is also possible to apply the LTE condition only partially depending on how many of these criteria are valid. In the past, a first study showed that it is possible to consider plasmoids as being into what is referred to as a “Complete LTE” state (CLTE). This is an interesting state to consider, because it easily gives access to a lot of information about the plasma studied. When valid, the CLTE condition allows for the atom density of all of the population levels to be derived everywhere in an ablation cloud at any recorded time and, ultimately, reconstruct the deposition profile of a plasmoid from the moment it is formed to the moment it is fully ablated. Eventually, a second study based on the premise that plasmoids are in CLTE led to the derivation of an unexpected T_e profile. In concept, ablating fuel pellets are cold blocks of particles that are dissolved by interacting with a much hotter surrounding environment. Under such circumstances, it is normal to think that the temperature in a plasmoid must be lower at its core than at its edges. However, the opposite has been derived in the second study. From these results, a question has been raised about whether the CLTE condition is valid everywhere in the considered plasmoids or not. Indeed, the supposition that the CLTE condition is valid in ablation clouds has only been verified from the observations of their global temporal behavior through the observation of the evolution of the in time the most intense region of plasmoids in function of time. Moreover, these previous studies were only able to observe ablation clouds that did not penetrate deeply into the plasma they were injected into. Consequently, the idea that the CLTE condition may not apply at every point in time and space seems to be a natural question to ask.

The main goal of this thesis is to to verify if the CLTE condition can be used to derive the profile of the parameters in plasmoids that are located in the core region of the Large Helical Device (LHD) plasma. It will be shown that it tends not to be the case, and that it is required to use another method. A new variation of the spectral model used in the first study is introduced. In addition, a new observation system has been designed, built and installed in LHD. This is why a thorough explanation of the new diagnostics system based on a spatially-resolved spectral measurement is also given in this thesis. That apparatus has been developed to collect spectroscopic data along the main direction of elongation of any targeted plasmoid. Data obtained with this observation system can be used to derive the integrated distribution profile of the different plasmoid parameters along a one-dimensional axis. This observation system presents itself as a sort of conceptual bridge between the two previously mentioned studies. Unless the first study which observed the global temporal behavior of a plasmoid, this system can study the light emitted from plasmoids at a local scale. Unless the second study which required the CLTE condition to work, this new system is not restricted by it. Also, in contrast with both studies, the present one focuses on plasmoids that are not located in the edge region but in the core region of the LHD plasma.

The studied pellet injections have been conducted during the 19th experiment campaign in LHD. The LHD is a superconducting MCF experimental device of heliotron type located in Toki, Japan. The LHD is recognized for the stability of its steady-state operating mode and the quality of its plasma confinement. It is equipped with a pellet injection system that already had the opportunity to prove itself in the past. All of these advantages make the LHD an ideal platform to test out whether the CLTE condition can be applied in plasmoids or not. Another relevant detail to point out is that the results obtained by the two previously mentioned studies have also been conducted in LHD. During this 19th experiment campaign, numerous configurations of pellet injections have been used. Also, for the first time in LHD, deuterium and deuterium/hydrogen plasmas experiments have been carried out in addition to the usual hydrogen plasma experiments. Of course, both deuterium and hydrogen pellets have been injected as well.

The new observation system consists of a visible spectrometer that is sent photons that have been collected by optics composed of a cylindrical lens and an optical fiber. These optics take advantage of the beam-shaping properties of cylindrical lenses by creating a narrow band-shaped FOV whose width is about 14 mm. The spectrometer is a two components system. The first component is a toroidal grating for flat-field polychromators and the second one is a dual line camera. Although the spectrometer has been designed so that no adjustments are needed, it is possible to fine-tune its grating. Due to the fast velocity of the plasmoids, about 1000 m/s, a fast acquisition rate is required to conduct spatially-resolved measurements. In that sense, the use of a line camera is advantageous. Its quick data processing rate allows the spectrometer to output one detailed spectrum every 14 μs. No entrance slit, intermediate mirror or any additional lenses are used to ensure the highest brightness possible. Simultaneous recordings with a fast camera are also conducted to visually confirm that spatially-resolved measurements are correctly achieved. The wavelength range measurements are done at is focused on the Balmer series emission lines of a hydrogen plasma. Plasma parameters such as n_{a}^{1}, n_{e} and T_{e} are derived from the spectra by fitting them with a spectral modeling code. The spectral model used is based on the precept that the photons emitted by the plasmoids are principally the product of Stark-broadened Balmer transitions and a radiative continuum that is the product of radiative recombination and radiative attachment processes. The lineshapes of the spectra are calculated from the convolution of the Stark-broadened lines and an instrumental function. The intensity of the lines are calculated from either the Saha-Boltzmann equation or a collisional-radiative model in respect of the chosen approach. The choice of the approach to use is made following the supposition that a studied plasma is in CLTE or not. The main difference between the CLTE and non-CLTE approaches is that n_{a}^{1} is considered as an independent variable in the second approach. Data obtained from the plasmoid produced by the sixth and last injected pellet of a LHD discharge have been analyzed. Comparison between the spectral data of the spectrometer and the imaging data of the fast camera confirms that it is possible to attribute a slice of plasmoid to each spectrum. Such results indicate that spatially-resolved spectral measurements can be conducted with the new observation system. Moreover, least squares fittings of the spectra with the new spectral model indicate that it is possible to derive the plasma parameters from the plasmoid with enough accuracy to observe its internal structure. Another important result found from the study of this plasmoid is that the CLTE approach does not allow to correctly explain the spectra. However, the spectra can be fitted more accurately when the non-CLTE approach is supposed. Qualitatively, the derived profiles of n_{a}^{1} and n_{e} are bell shaped with a slight dip visible near the central region of the plasmoid. The profile of T_{e} is the lowest in the central region of the plasmoid and is slightly higher toward its edges. As for the profile of V_{s}, it is found to be small toward the edges and asymmetrically distributed along the body of the plasmoid. Quantitatively, the obtained results are in agreement with what can be found in other simulations and similar experiments to the exception of the values of T_{e} which stand out from the rest of the results. The derived n_{e} profile ranges from $1 \times 10^{23}\,\mathrm{m}^{-3}$ to almost $2 \times 10^{23}\,\mathrm{m}^{-3}$ while n_{a}^{1} swings from $1 \times 10^{26}\,\mathrm{m}^{-3}$ to $4 \times 10^{26}\,\mathrm{m}^{-3}$. The V_{s} values obtained are close to $1 \times 10^{-9}\,\mathrm{m}^{3}$. As for T_{e}, its profile is close to $0.4\,\mathrm{eV}$ in the main body and slightly increases toward the edges. An interesting feature observed is the opposing trends of n_{e} and n_{a}^{1} with respect to T_{e} and V_{s}. The complexity of the spectral model makes it difficult to assess the margin of error of the results. Yet, results are encouraging as they provide a new plausible path of interpretation for ablation clouds and pellet injections in MCF devices from both a practical and theoretical point-of-view.

This thesis is divided into six chapters. The first chapter introduces the thesis. The second chapter presents the new approach proposed by the study, the observation system based on this new approach and the implementation of the observation system into the framework of the LHD. The third chapter gives the details of the method used to calibrate the experimental data as well as the way the data is processed in order for it to be analyzable. The fourth chapter exposes the methodology and results that confirm that the new observation system can successfully conduct spatially-resolved spectral measurements. The fifth chapter presents the spectral model developed to study plasmoids and two different declinations of the model which are used to analyze the experimental data. Experimental results and comments of the results are also included in the fifth chapter. The sixth chapter concludes the thesis.

Acknowledgement

First of all, I would like to thank the Japanese government for the generous support they gave me in form of the MEXT scholarship. I would also like to express my gratitude to the Graduate University for Advanced Studies (SOKENDAI) for accepting me with helping hands as a graduate student into their three years program. Thanks are also due to all of the administrative and academic and technical staff of the NIFS, who gave me more attention that I could have hoped for. I have been given the opportunity to participate actively to the 19th experimental campaign of the LHD. An important campaign that saw the first deuterium experiments to ever be conducted in LHD. Being able to carry out my own experiments with the experimental setup that has been collaboratively designed, built and installed on LHD, must have been one of the most enriching experience I have ever been offered to live these past few years.

I take this opportunity to thanks all of the people that have been involved in the development of the said experimental setup and rewarded me with constructive comments and remarks. I am mainly talking about Dr. G. Motojima, Dr. Y. Narushima, Dr. R. Sakamoto, Dr. I. Murakami, Dr. S. Morita as well as Dr. K. Fujii and his seminar students of Kyoto University. I am also talking about the unnamed professorial and technical staff of the NIFS for their considerable support into this endeavor.

I want to present my extreme gratitude to my supervisor, the Dr. Motoshi Goto without whom nothing of this would have been possible. Thank you for your patience and for teaching me so many things which I am sure, will be very useful in the future. Also, I am sorry for the trouble I may have caused you in so many occasions. I sincerely hope that what has been produced from this work will, in some way, be of use to you.

This acknowledgement could not be complete without mentioning my colleagues, Liu Yang, Junki Morimoto, Shishir Purohit, Jie Huang, Le Trang, Takeru Ohgo, Makoto Ohno and, especially, Nilam Nimavat with whom shared incredible adventures as a graduate student inside and outside of the NIFS. Thank you all for bringing me motivation when I needed it the most. Thank you for all the intellectual and material support you unconditionally offered me.

I would also like to extend my gratitude to the administrative staff members of both the NIFS and SOKENDAI with whom I had long and direct interactions and for whom certain are not working here anymore. I am thinking about Kameyama-san, Hayashi-san, Irino-san, Ando-san, Urushihara-san, Masuda-san and every other person with whom I might have interacted in one way or another.

Contents

List of Figures

Chapter 1

Introduction

It is generally agreed upon by the research community on Magnetic Confinement Fusion (MCF) that the pellet injection process is an important but yet to be fully understood tool. Pellet injections can be employed in a wide range of applications. Particularly, an application of primordial interest revolves around the ability of certain type of pellets to provide fuel to the background plasma they are injected into. This fueling potency can be quantified by measuring the so-called deposition rate of a pellet as it progresses into the background plasma. That is why reliable and non-intrusive diagnostics are required to obtain such measurements. Because of the extreme conditions usually found in background plasmas and the nature of the pellet injection process itself, passive spectroscopic approaches are preferred to analyze the light emitted from ablation clouds such as the ones found in the Large Helical Device (LHD). In addition, it is also necessary to build an appropriate spectral model to analyze the data. As for every model used in data analysis, a certain degree of interpretation is needed to build a spectral model that could explain the light emitted by ablation clouds. Due to the complexity of the interactions that occur in ablation clouds, it is not evident to identify perfectly all the processes that are involved during their lifetime. As such, it is customary to process any obtained data with very restrictive approximations. Results found by the most current models usually give reasonably good estimations about the ablation clouds and their interaction with the background plasma. However, the gap of inconsistencies between the experimental results and the commonly accepted theoretical models keeps increasing since the arrival of more accurate acquisition methods. For the purpose of this thesis, a particularly concerning inconsistency, is put into focus. The inconsistency in question hints that the way ablation clouds behave internally may not be as simple and consistent as previously supposed.

This introductory chapter is divided into two sections. The first section introduces the concept of fuel pellet injection and the process of pellet ablation. This section also presents some trivia about the LHD and its fuel pellet injection system. The second section introduces two pellet experiments that have been conducted in LHD. These experiments are at the root of the problematic treated in this thesis. The problematic itself and the methods proposed to resolve it are also presented.

1.1 Pellet injection experiments and study of fuel pellet ablation clouds

In this section, the concept of pellet injection is briefly defined both historically and technically. Also, the process of pellet ablation is partially introduced. Finally, the fuel pellet injection system employed in LHD during the study conducted in this thesis is mentioned.

Pellet injection and ablation cloud

The idea to inject pellets into MCF devices to refuel them has supposedly been introduced for the first time by Spitzer in 1954 [1]. And it took almost twenty more years to implement the technology, collect experimental data and process them both theoretically [2] and experimentally [3].

Although the concept of pellet injection has a broad range of applications, only the fueling aspect is considered in this thesis for both the sake of simplicity and availability. Fuel pellets are composed of the same component than the plasma they are trying to feed. In MCF devices, the fusion plasmas produced are made of hydrogen isotopes. There are more than one way to produce a fuel pellet. One way a fuel pellet can be created is via a cryogenic process, where a gas of hydrogen isotope is injected into a barrel and is cooled down until the gas turns into a frozen ice pellet of dimensions specific to the barrel it is in and the amount of gas used. The obtained ice pellet is then injected in the background plasma of a MCF device usually via a pneumatic process. As soon as an injected pellet enters into contact with the background plasma, it will start to ablate due to the environing heat. The physics behind the pellet ablation process is complex and is still heavily under investigation [4]. When ablating, the matter diffused by the pellet does not immediately thermalize with the background plasma. This leads to the formation of a cloud formed by successive layers of ionized plasma, the layer of plasma the closest to the pellet core being the less ionized. These successive layers act as a protective shield for the pellet core, and briefly lengthen the life expectancy of the pellet in the background plasma. The pellet core and its surrounding layers can be referred to as an ablation cloud, a plasmoid, or also, an ablatant. The expansion of an ablation cloud is not infinite. The shape and size of an expanded ablation cloud depends on different parameters. But both theory and experiment tends to agree that the direction toward which an ablation cloud will be the most expanded is along the direction of the magnetic field line it is on.

In ideal cases, an ablation cloud expands until it reaches a spheroid shape (generally prolate) as represented in figure 1.1. Such shape is sometimes referred to as “cigar-shaped”. The green arrows represent the direction of the magnetic field whereas the light-blue arrow represents the velocity vector of the ablation cloud. It can be seen from the figure that these differently colored arrows do not point toward the same direction. This is, for most situations, always the case as the angle of injection of a pellet has to be in such way that some of its content can be delivered the core of the background plasma. The deep-blue arrows represent the velocity vector at which the ablation cloud expands.

The deep-orange arrows represent the pseudo-velocity vector at which the expansion of the cloud is prevented. When the deep-orange and the deep-blue vectors are of same amplitude, its expansion is stopped. At this stage, the ablation cloud is considered to be in a pseudo-stable state, where its minor and major radii noted r_o and Z_o, respectively, do not grow further unless some other external intervention occurs. The clear-orange arrow represents a drift velocity vector that will not be explained here. For more information, please refer to ref. [4, 5]. The figure 1.1 is only a simplified representation of what is

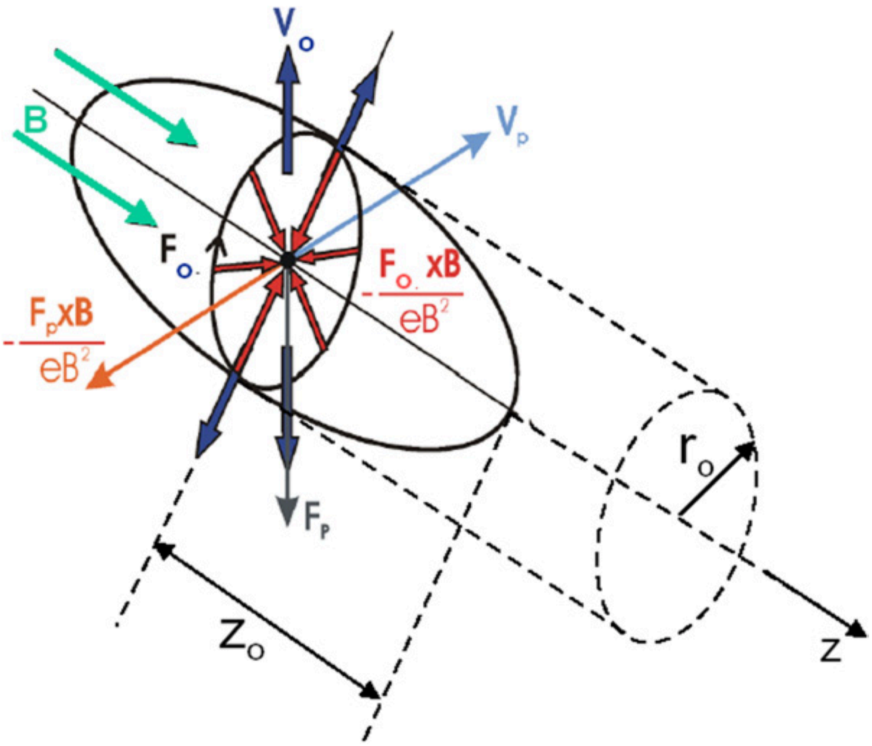

Figure 1.1: Illustration of a spheroid-shaped ablation cloud [source: Topical Review on "Pellet injection experiments and modelling" by B. Pegourie (2007)]

really supposed to be an ablation cloud based on the so-called neutral gas shielding (NGS) model. There exists more than one ablation cloud model such as an extension of the NGS model called neutral gas plasma shielding (NGPS) model just to name one. Although it is knowingly incomplete, the NGS model is still considered as one of the most convenient method for analysis purposes by most of the research community [6]. It is common to find this model at the center of studies centered around pellet-plasma interaction(s) [7]. Under such situations, ablation clouds are most often seen as ablatants influencing the behavior and configuration of the background plasma they are injected in. However, for this thesis, wish has been to take an approach that puts ablation clouds at the center of the attention, and consider them more as plasmoids being perturbed by a background plasma. This is a subtle change of point-of-view, with few consequences, but that the author thought to be important to precise.

Fuel pellet injection in LHD

The LHD is a MCF device of heliotron type that is located at the National Institute of Fusion Science (NIFS), Toki (Japan). It is build around a double helicoidal superconducting magnetic coils that can produce magnetic field strengths of up to 3 T. With a vacuum chamber of 30 m^3, it has a major radius R and minor radius r of 3.9 m and 0.6 m, respectively. The LHD is not unknown to fuel pellet injection experiments. Since its inauguration, it has already been equipped many generations of pellet injectors [8, 9]. Moreover, many experimental results have also been produced from them [10, 11].

For the 2017 LHD experimental campaign, fuel pellet injection experiments have seen the introduction of the option to inject deuterium pellets in substitution to the usual hydrogen ones. Fuel pellet injection are conducted on the diagnostics wall 3-O of the LHD as shown in figure 1.2.

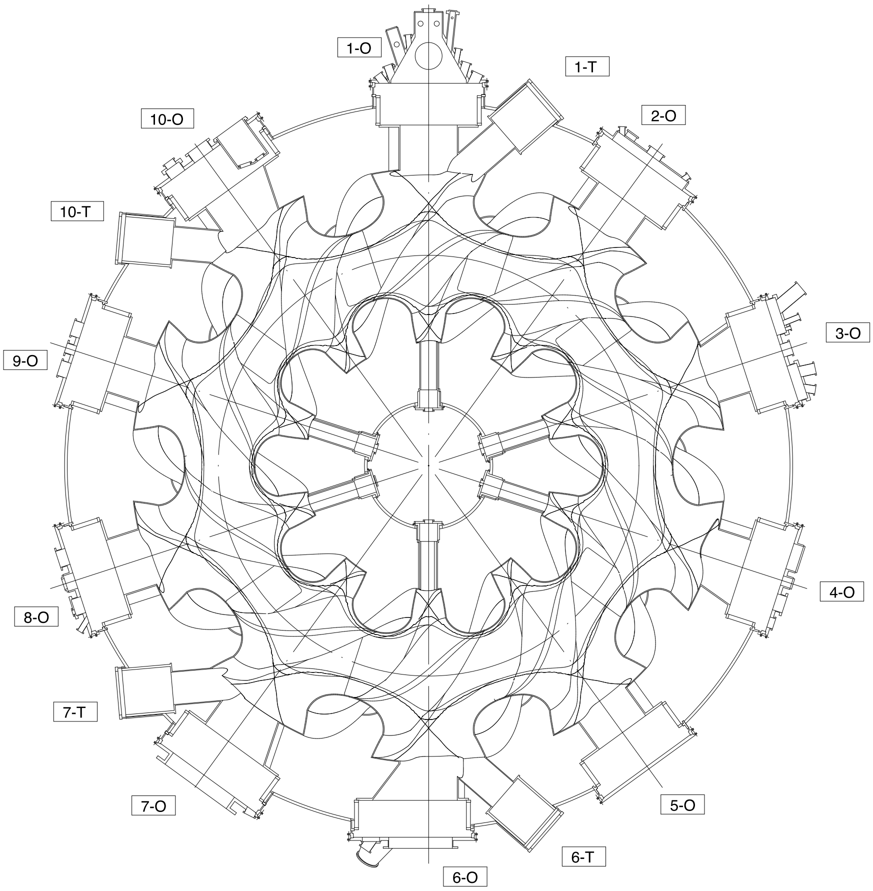

Figure 1.2: Top view of the schematics of the LHD with focus on the diagnostics walls [source: provided to the author by Dr. G. Motojima]

Figure 1.3 shows the side view of the fuel pellet injection system used in the 2017 LHD experimental campaign where the injection pellets is done on the equatorial plane of the vacuum vessel in such a way that the unperturbed trajectory of the pellets goes through the plasma core (plasma indicated by the colored region inside the vacuum vessel). What is not observable on figure 1.3 however is that the pellets are not injected on a parallel line with the radial axis. Indeed, as confirmed by figure 1.4 that shows the top view of the same configuration, the pellet gun actually is injecting pellet at an angle of about 6° (blue dash-dotted line) with the radial axis represented by the normal of the diagnostics port (continuous line). In addition, figure 1.4 also shows where the pellet trajectory is supposed to cross the core plasma under a specific configuration of the LHD. One of the mode of operation the LHD that is often used is when the magnetic field axis is set at $R_{\mathrm{ax}} = 3.6$ m. It corresponds to a plasma configuration where the magnetic coils are set so that the plasma is contained and confined around a main magnetic field line located at a major radius of 3.6 m from the center of the LHD. The area surrounding the point of intersection between the trajectory of the pellet and the main magnetic field line is designed as the area of interest of the measurements that are conducted in this study. For simplicity, this area will be referred to as X_{cross} from now on.

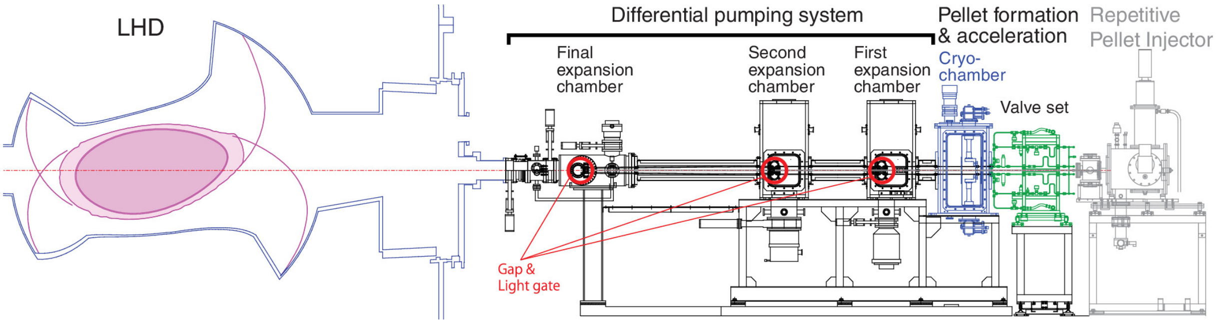

Figure 1.3: Side view of the schematics of the fuel pellet injection system in LHD [source: "Twenty barrel in situ pipe gun type solid hydrogen pellet injector for the large helical device" by R. Sakamoto *et al.* (2013)]

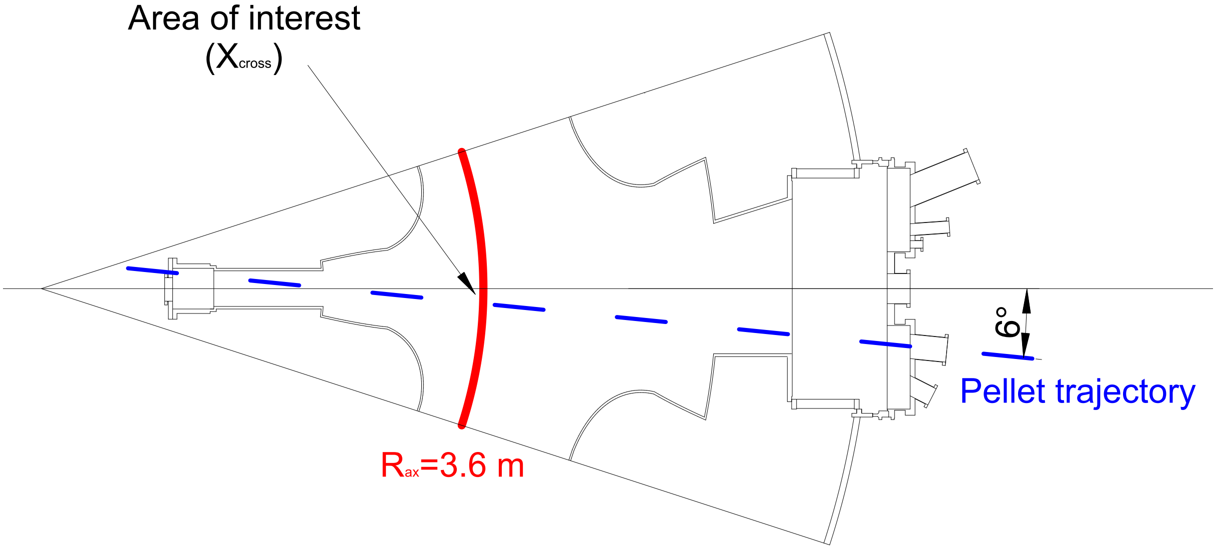

Figure 1.4: Top view of the schematics of the fuel pellet injection trajectory in LHD

1.2 Toward a new experimental method to study fuel pellet ablation clouds

In this section, the context of this thesis is explained with the introduction of two specific experiments that have been conducted in LHD. Also, the main problematic of this study is introduced as well as an introspective on how crucial this work may be for the future of the research on pellet ablation.

First experiment: temporal observation

This story begins from a paper published about the study of the evolution of the spectra emitted from a plasmoid in LHD [12]. A fuel pellet is injected in the vacuum vessel of the LHD and starts to ablate as it reaches the background plasma. The light emitted from the plasmoid created by the ablating pellet is observed with a visible spectrometer. The position of the observation port and the optics used by the observation system are such that it is possible to spectroscopically observe the evolution of the light emitted from the most intense region of the plasmoid from the beginning to the end of its lifetime in the background plasma. The spectra obtained after the plasmoid is completely thermalized with the background plasma can then be analyzed via a least squares fitting method to extract information about the plasmoid.

In this case, the spectral model used to fit the spectra considers both the emission lines and the continuum radiation for the fitting method. Most importantly, the spectral model supposes that the plasmoid was in what is referred to as Complete Local Thermodynamic Equilibrium (CLTE). As a stricter version of the more well known Local Thermodynamic Equilibrium (LTE), the CLTE condition, if confirmed, allows one to derive the neutral density profile of the plasmoid relatively simply. For more information about how it is so, please refer to chapter 5 and/or ref. [13]. Via the neutral density profile of a plasmoid, it is possible to estimate the deposition profile of the pellet in the background plasma. Ultimately, this knowledge could help improve the methods of pellet injection up to a point where they are able to provide MCF devices with fusible matter as efficiently as possible.

Figure 1.5 shows an example of fitted spectrum taken for $t_{\mathrm{rel.}} = 352\ \mu\mathrm{s}$ is also shown (left figure). The fitting results for the electron temperature T_{e} and density n_{e}, as well as the estimated volume V of the ablation cloud in function of time is also shown (right figure). These three parameters are, with the neutral density n_{H} (not shown here), the input parameters of the spectral model used to fit the obtained spectra. In the left figure, the symbols P_A, P_R and P_B represent the radiative continuum contributions and correspond to the radiative attachment continuum, the radiative recombination continuum and the bremsstrahlung, respectively. The H_α, H_β and $\mathrm{H}_\gamma$emission lines have been fitted with a stark broadening code. In this spectral model, the opacity of the plasma has also been taken into account for the spectral line near 656 nm (i.e. H_α) where it has been estimated to be significant. In reference [12], the neutral density has been derived from two different methods. In a first time, n_{H} has been directly derived from fitting the spectra via the con-

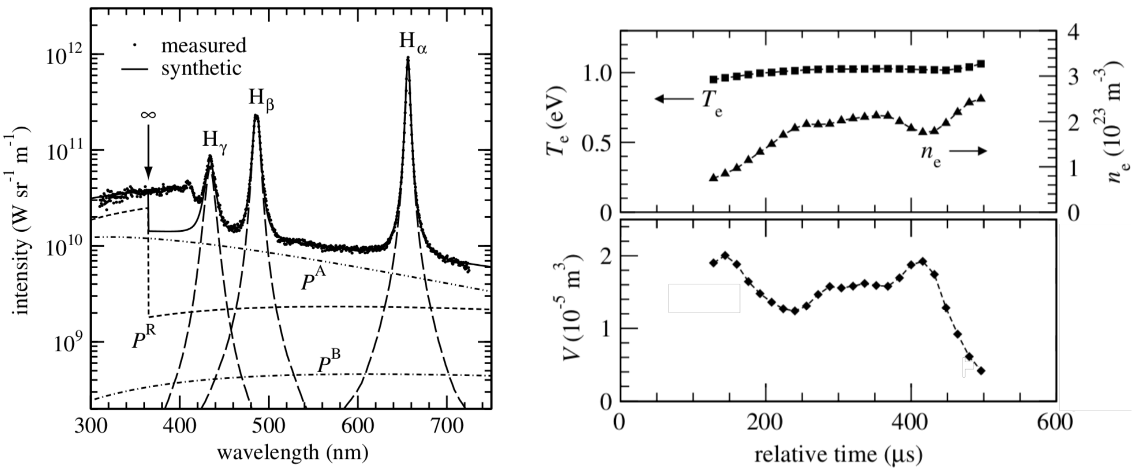

Figure 1.5: Fitting results for hydrogen pellet ablation cloud under CLTE condition (left spectrum corresponds to $t_{\text{rel.}} = 352\ \mu$s) [source: "Experimental verification of complete LTE plasma formation in hydrogen pellet cloud" by M. Goto *et al.* (2007)]

tribution of the radiative attachment continuum. In a second time, it has been estimated from the CLTE condition, where the so-called Saha-Boltzmann equation is applied to the ground state density. Comparison showed that the n_{H} obtained from these two methods matched. Results found in this experiment indicate that it is reasonable to consider that the plasmoid is in Complete Local Thermodynamic Equilibrium.

Second experiment: spatio-temporal observation(s)

Results found in the first experiment can be traced back to a second experiment [14]. The goal of this second experiment can be roughly explained by the wish to obtain more detailed profiles of plasmoids thanks to the imaging capability of a fast camera as well as the ingenious combination of fiberscopes and filters. Same as before, a fuel pellet is injected in the vacuum vessel of the LHD and starts to ablate as it reaches the background plasma. However, this time, instead of looking at the ablation process with a visible spectrometer, a set of fiberscopes equipped with filters are used. When the light collected by these fiberscopes is projected onto the CCD of a fast camera, it becomes possible to observe a full image of the plasmoid and not only its (supposedly) most intense region. Like so, it becomes possible to obtain a spatio-temporal observation of any detected plasmoid, for specific wavelength ranges that can be selected in function the filters used. The ability to obtain such detailed profiles of plasmoid can help the research community to have a better insight on the phenomena that occur in a plasmoid.

In the same spirit as the first experiment, plasmoids are considered to be in CLTE. This condition is actually required for the measurement method to be possible. Indeed, contrarily to the first experiment, this second one does not collect the full spectra of plasmoids. Instead, a series of fiberscopes equipped with filters collect photons in very selective wavelength regions. Two regions are of main interest. The first region corresponds to a portion of the radiative continuum located between H_α and H_β. The second region corresponds to H_β itself. The data collected by this imaging diagnostics does not allow for much spectroscopic interpretation as only an integrated signal is obtained for each wavelength region observed. However, what is lost in spectral resolution is gained in spatial definition. Ultimately, this approach does not only provide a way to improve our understanding of how plasmoids visually behave, but it can also serve as a way to monitor them "directly" and not only via the spectra they produce.

The figure 1.6 taken from the second experiment shows pictures of the distribution gradients of two plasma parameters found in a plasmoid. The picture has been extracted while the short lived plasmoid of about 0.4 ms was in its mid-life period, close to the 0.209 ms time stamp. The observed plasmoid is of prolate shape and its maximum longitudinal elongation (i.e. following the magnetic field lines) can be estimated to be of about 20 cm. Such plasmoid corresponds to what is typically obtained when pellets are injected into the LHD. The figure to the left represents the electron density distribution profile inside the plasmoid and the figure to the right represents the electron temperature distribution profile. It can be seen from the electron density distribution profile that the central region of the plasmoid is more than one order of magnitude denser than the edge regions. This is to be expected as the pellet acts like a source of matter in the less dense background plasma of the LHD. For comparison, the background plasmas of the LHD can boasts an average electron density of the order of 10^{20} m^{-3} at best, whereas each fuel pellet can pack about 10^{21} particles in less than 10^{-5} m^3 and most measurements in LHD show that the electron density in the produced plasmoid vary between 10^{22} m^{-3} and 10^{24} m^{-3}. It can be seen from the electron temperature distribution profile that the central region of the plasmoid is warmer than the edge regions. However, this results contradicts how ablation clouds are expected to behave. When the electron temperature of the background plasma of the LHD is mentioned, the unit generally used is in the KeV range (near 11 605 000 K). In opposition, the fuel pellets are produced by being brought down to temperatures

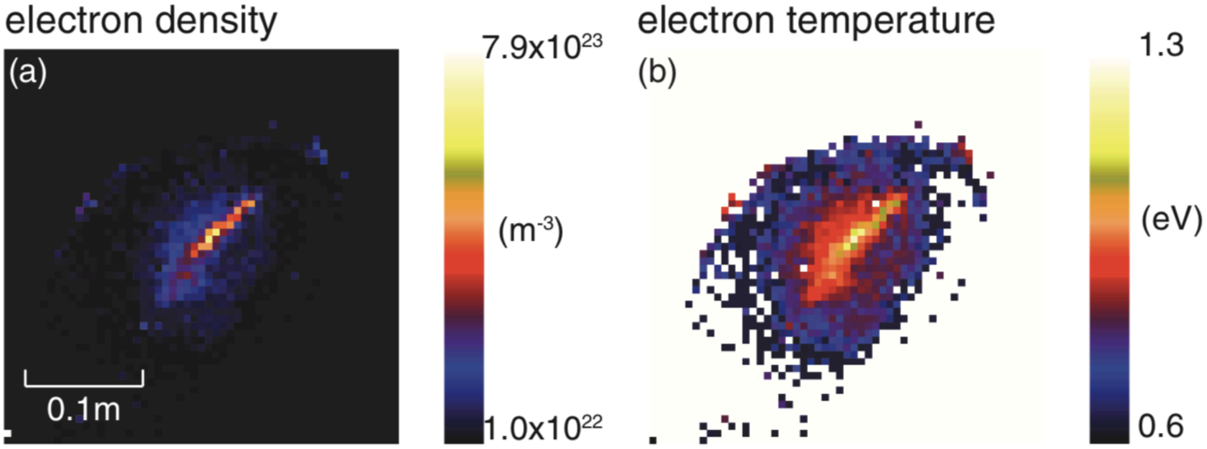

Figure 1.6: Plasma parameter in plasmoid derived from imaging diagnostics in LHD [source: "Imaging spectroscopy diagnosis of internal electron temperature and density distributions of plasma cloud surrounding hydrogen pellet in the large helical device" by G. Motojima *et al.* (2012)]

close to 10 K, and the electron temperature found in plasmoids usually is the eV range (1000 times colder than the background plasma).

If the notion that a plasmoid is a pellet surrounded by increasingly ionized layers of plasma that act as a shield is kept in mind, it would seems counter-intuitive to find higher temperatures in the central region of the plasmoid, where the solid core is supposed to be. The opposite, more intuitive behavior is correctly illustrated by the results shown in figure 1.7. In this study [15], a slightly different approach is taken. Contrarily to the two previous experiments, this one does not attempt to directly measure the plasma parameters of the plasmoids. Instead the analysis is purely based on the analysis of the intensity profile of plasmoids with an ablation cloud model. A fast camera is still at the center of the observation system but no complicated arrangement of filters is used. As such, only data related to the intensity profiles of plasmoids are recorded. To extract information from the obtained data, synthetic intensity profiles are produced by an ablation cloud model and compared to the experimentally obtained ones. When a match is found, the plasma parameters given in the model to produce the similar intensity profile are considered to be close to the experimental case. When the focus is put on T_e and n_e, it

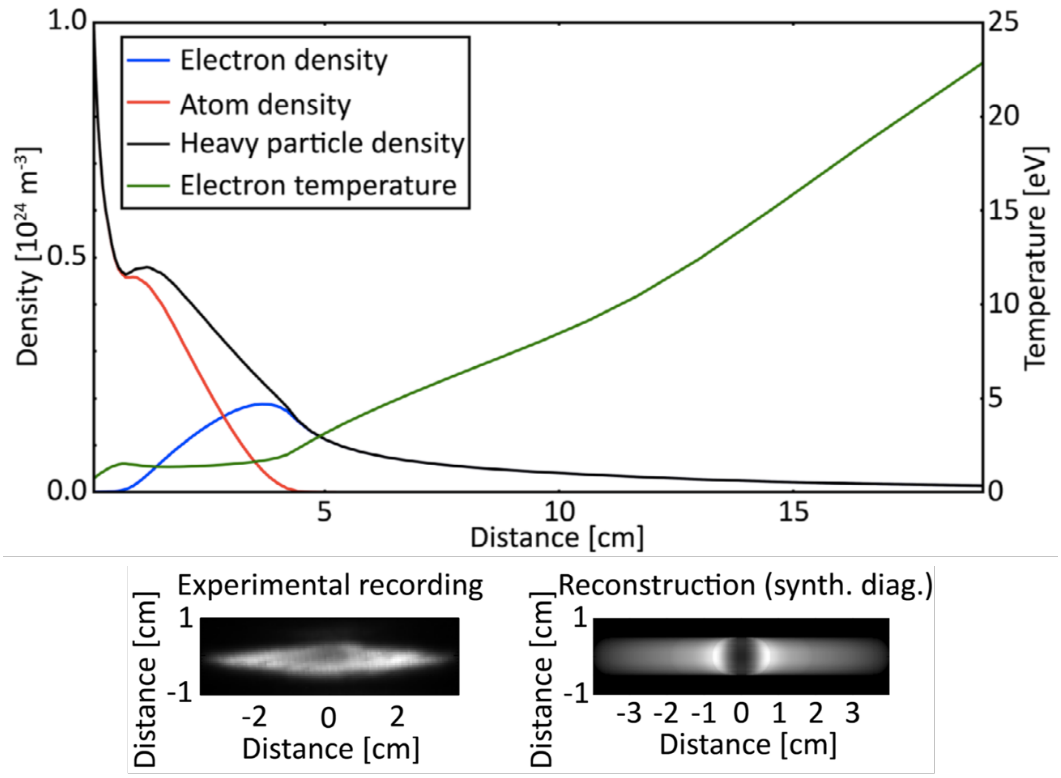

Figure 1.7: Synthetic diagnostic of hydrogen pellet intensity profile using a theoretical ablation cloud model. [source: "Pellet cloud characterisation, scaling and estimation of the material- and temperature distribution inside the cloud" by G. Cseh *et al.* (2017)]

can be seen that the results obtained are somewhat different from the second experiment. A clear dip is observed in n_e and, more importantly, the behavior of T_e is completely different. Not much more can be said from this comparison. Indeed, due to the different experimental conditions between this experiment and the second one, no real quantitative analysis can be done. One point that can be treated is the behavioural difference related to n_e might be attributed to a difference in resolution of the imaging devices used. In fact, such behavior has also been observed [16] with the observation system used in the second experiment, albeit not as smoothly as the one showed in figure 1.7. This point will however be treated further into this thesis. Another point that can, and must be treated is the clear difference observed between the profiles of T_e. The reason for this divergence is not clearly understood. Although the experimental conditions are not the same, it should not results to such fundamental difference.

A plausible reason for the unexpected T_e profiles extracted from [14] is that the use of the CLTE condition may not be appropriate. The main argument behind this explanation is linked to the requirements needed for a plasma to be in CLTE in the first place. In most cases, only the value of n_e is considered when the validity of the LTE condition is put into question. However, in certain cases, the value of T_e may actually be of importance. A more detailed explanation of this argument is given in chapter 5. Also, for those in need for more information, the reference [17] shall provide additional elements needed to understand the rationale behind the argument developed here.

The need for a third experiment: spatial observation

As a follow up for the two experiments [12] and [14], a third experiment is proposed. The principal goal of this third experiment is to test whether the CLTE condition can be invalid in at least one ablation cloud. The idea is still to observe a plasmoid as it moves through the background plasma of the vacuum vessel with an observation device. However, this time, the observation system relies on a localized spectroscopic approach to collect spectra from within the plasmoid. Such approach differs from the first experiment where the focus is to obtain the temporal behavior of the plasmoid. This approach also differs from the second experiment in the sense that only the spatial capability is kept. The temporal capability is lost to the benefit of a greater amount of information contained into the collected data. Also, the real advantage of this method (as well as the ones used in the first and second experiments) over the one used to obtain the results shown in fig. 1.7, is that the plasma parameters in the plasmoids are derived from direct measurements and not from the synthetic reconstructions of their intensity profile. Ultimately, answers provided by this third experiment should give another insight about how ablation clouds behave in the background plasma of a MCF device, and help the research community to build more accurate models.

Prior to this thesis, the LHD did not have the capability to produce the data required for this third experiment. As a matter of fact, prior to this thesis, there was no observation system capable to meet the need of this third experiment. This is the reason why the specifics of a new observation method is also introduced in this thesis. Experimental approaches to directly characterize plasmoids at a local scale are nothing new. As the second experiment indicates, such feat is already doable. Moreover, attempts to spatially profile plasmoids have already been attempted as can be attested in studies conducted in the tokamak T10 [18, 19] many years ago. However, these experiments appear to be similar to what has been conducted in the second experiment both experimentally and theoretically. Surprisingly, the results obtained from these analyses are different from the second experiment and give electrons temperature profiles that are in agreement with the consensus. Force is to say that the plasmas produced in T10 must be different than the ones produced in LHD. In any case, with things as they are, it seems that the question will stay unanswered if only results given by imaging diagnostics are the only source of experimental data. As mentioned previously, most, if not all of the direct measurements done from imaging diagnostics rely on the so-called (C)LTE condition(s) to work. Of course, the possibility that another kind of misshape occurred in the second experiment should also be considered, but, in order to discard any doubt about the (C)LTE condition(s), investigating the matter by using as many point-of-views as possible is advised. This is done via spectroscopic approach that is similar to what has been done in the first experiment [12]. Spectra are collected with a spectrometer and analyzed with a more spectral model that is more complete than the ones used in the other types of experiments.

In fact, the onus is knowingly put on the LTE condition because of what has already been concluded from the observation of other kind of plasmas obtained in MCF devices. Overall, plasmas can be classified into two categories which are defined in function of how dense the plasma considered is. When the density is low, plasmas are considered to be in the so-called coronal regime. When a coronal "equilibrium" is reached in a plasma, the rate of decay of the excited particles dominates over the rate of collisions. In the opposite case, when the density is high, plasmas are considered to be in the so-called Local Thermodynamic Equilibrium, or LTE. When in LTE, the rate of collisions between the excited particles becomes higher than the rate of decay. There is also what is referred to as the Complete LTE, or CLTE, that has been mentioned earlier in this introduction. More will be told about the CLTE in chapter 5. For now, suffice to say that, when a plasma is in CLTE, its particles found in the ground state can also be included into the calculations. Plasmas produced by MCF devices are usually considered to be in the dense plasmas category, and, for a long time, the LTE condition has been used to process them. In reality, it appears that the plasmas studied are not exactly in LTE, and more complex models are required to analyze them properly. An example of more complex model is the Collisional Radiative (CR) model. More about this model will be mentioned in chapter 5. For those who cannot wait, reference [20] gives a short introduction on how the model works, as well as where it stands compared to coronal and LTE based models. An extensive amount of information about the CR model can be found here [17] and here [21]. There can be many reasons as to why a fusion plasma is not in LTE, none of which will directly be treated here. What needs to be kept in mind is the idea that fusion related plasmas are not necessarily in LTE, and, as such, this should also apply in the case of fuel pellet ablation clouds.

As reminded a few times already, before being even able to study the validity of the LTE condition in plasmoids, it is first necessary to collect the experimental data that would allow such analysis. This is where the new proposition of a third experiment comes in. A significant part of this thesis is dedicated to the development (cf. chapter 2), calibration (cf. chapter 3) and testing (cf. chapter 4) of a new observation system. This observation device is designed to collect spectra emitted by “slices” of plasmoids, where each slice corresponds to a section of a plasmoid that would have been split along its direction of elongation. It means that a plasmoid like the one shown in fig. 1.1 is virtually sliced along its z-axis (i.e. along the magnetic field line it is on), and the light emitted by each of these slice is recorded with a spectrometer. The recorded spectra shall then be analyzed with a specifically implemented spectral model (cf. chapter 5) to derive the plasma parameters profiles of the plasmoid (cf. chapter 5). In conclusion, this work will attempt to argue that the old habit to still consider plasmoids as being untouched by the LTE crisis known to most of the other fields of the research on MCF plasmas is not viable anymore.

Chapter 2

Experimental method

Prior to this thesis, the LHD has already been the host of various experiments related to the study of fuel pellet injections. However, the current work relies on data that can not be obtained by what has already been done in LHD. A requirement to extract the plasma parameters from the internal structure of any plasmoid is to collect data of the said plasmoid at a very local scale. Moreover, not only the data has to be spatially specific, it needs to be format specific as well. If only a spatial measurement of ablation cloud is required, one of the fast camera installed in LHD should be sufficient. For this new study, the data collected has to be of detailed spectra of section of plasmoids. The use of an imaging diagnostics is therefore not adapted in this case. As such, a new observation system designed around the use of a spectrometer had to be deployed.

A conventional spectrometer is inherently incapable of collecting localized spectroscopic data by itself. To do so, a peculiar arrangement of optics is used to select the photons that will be analyzed before they reach the spectrometer. The main idea behind this optical system is to observe the light emitted by a specific region of the vacuum vessel of the LHD, to discard most of it and to let only a narrow vertical band-shaped portion of photons goes through an optical fiber. When correctly setup, this optical system shall be able to collect photons that are emitted by ablation clouds in such a way that each of these recorded frames can be associated to a section of plasmoid. The name given for this newly developed approach of observation is spatially-resolved spectral measurement, or SRSM.

This second chapter is divided into three sections. The first section introduces the concept of the observation system. It details what is meant by spatially-resolved spectral measurement and explains how it should be achieved in LHD. The second section introduces the specification of the observation system that has been developed accordingly to the expectations of the first section. The two modules which compose the observation system are fully described. The third section delves into the technicalities of how the observation system has been implemented into the framework of the LHD.

2.1 A novel approach for the study of fuel pellet ablation clouds

In this section, the concept behind a spatially-resolved spectral measurement is presented. An emphasis is put on identifying the limitations of the current setup, their consequence(s), and the way(s) they can be corrected and/or mitigated.

2.1.1 Experimental concept

The idea is to hash a targeted plasmoid into virtual slices and to produce a spectrum for each of these slice for spectroscopic analysis purposes. The approach taken to obtain such spatial-resolution capability relies on a specific, yet simple combination of optical components. However, the complexity of the task does not stem so much from the equipment used, but more from the nature of the experiment. Firstly, the pellet injection process itself is very quick. When a fuel pellet is injected into the vacuum vessel of the LHD, it is usually set to move at a velocity of about 1000 m/s. Moreover, the ablation of a fuel pellet only lasts a few hundreds of μs at best. Secondly, the scale that is of interest for this measurement is small. Plasmoids are small objects relatively to the plasma they are in. Although it is quite easy to detect and observe them in their entirety, it is quite a different challenge to only collect the light emitted by small sections at a time. Thirdly, the trajectory and structure of a pellet are to be understood clearly. As briefly explained in the previous chapter, the geometrical aspects associated with a pellet injection is not trivial. The direction a plasmoid propagates to is, in most cases, not the same as the direction it is elongated toward. In addition, the shape and size of plasmoids are not constant in time and are very susceptible to the configuration of the plasma they are in. Hopefully, most of these concerns can be addressed with an adapted experimental setup (i.e. two first points). As for those that cannot be avoided (i.e. third point), adequate timing and conditions will allow for some convenient approximations to be made.

The first point is solved with the use of a spectrometer that has a fast acquisition rate and a long recording time. Nowadays, it is not that hard to come by apparels capable of such feat. With correct hardware, programming and storage space, it has come to a point where the plasmoid velocity variable is of almost no consequence. The second point is mainly addressed via the optics employed by the observation system. The reduced field-of-view (FOV) required to conduct local measurements in plasmoids is created from the combination of a cylindrical lens with an optical fiber. Properties of cylindrical lenses are often used in laser beam shaping applications. Incidentally, these properties can reciprocally be exploited to produce narrow FOVs. The third point presents a bigger challenge to overcome. The observation location and the optics of the are set so that the spatial resolution applies on the main direction of elongation of plasmoids. However, some precautions need to be taken as to what is exactly meant by spatial resolution. It is known already that plasmoids tend to expand the most along the magnetic field lines they transit on. Considering an unperturbed pellet trajectory, this means that the FOV of the observation system has to be oriented as perpendicularly as possible to some specific magnetic field lines of interest. In addition, the magnetic field lines of interest shall be chosen in consideration to the configuration of the background plasma in regards to the state the observed plasmoids is in. In other words, it means that the plasmoids should not change much while they are observed by the diagnostics, otherwise it would not be accurate to say that all of the obtained slices correspond to the "same" plasmoid. The way pellets ablate into the background plasma of a MCF device depends directly on the configuration the latter is in. The main parameters to consider is the surrounding plasma temperature, the more it changes, the most irregularly pellets should ablate. This is why it is key to find a region in the background plasma where the temperature stays as homogeneous as possible. Such homogeneity can, in most cases, be found in the core region of some favorable plasma discharges. Statistical proof of this will not be provided here, but an illustration of this often recurring observation will be given in chapter 4.

Some additional limitations have to be considered. For example, the trajectory taken by a pellet can be modified by external perturbations (i.e. plasma configuration and heating). If the trajectory of a pellet is modified, the interpretation of the collected data may get more complicated, so care needs to be taken to chose the most appropriate pellet injection to study. A reliable way to proceed is to chose a pellet discharge which is known to be less likely to be perturbed by external sources. A study [11] that has already been done about it gives some ideas of which external sources need to be cared for. It has been found that there exists a certain type of plasma discharges in LHD for which the trajectory of plasmoids is less likely to be modified. Figure 2.1 shows two cases where the trajectory of plasmoids can be kept linear (top) and modified (bottom). When the so-called balanced Neutral Beam Injection (NBI) heating is used, plasmoids seem to keep their linear trajectory. The horizontally oriented curves represent the magnetic field lines (top view) while approximate location of the plasmoids is represented with the circles. The graduated oblique lines show the theoretical trajectory of an unperturbed plasmoid. With an asymmetric heating pattern such as a counter-clock-wise NBI, plasmoids tend to get "pushed" away from their unperturbed trajectory. It is supposed that the push is created from the interaction of the NBI on the plasmoid via what is referred to as a rocket effect. Another limitation is that the direction of the magnetic field lines an injected pellet is passing through are not optimal. Ideally, the elongated pellet is perpendicular to the FOV of the optics so that the profile of the slices of plasmoid collected are as flat and contiguous as possible. In fact, the magnetic field lines in the LHD are not parallel between one another. This means that the plasmoids will slightly rotate while being measured. The measurement of such plasmoid will result in sections of plasmoid to change and/or overlap while they go through the FOV of the observation system. With a relatively reasonable rotation angle, such happenstance will not irremediably corrupt the data. It may still be possible to extract information from it, at the price of accuracy. The amount by which a plasmoid rotates is dependent to the distance it travels between the first and last frame of measurement. This distance can be estimated from the knowledge of the plasmoid velocity and time of transit through the FOV of the observation system. Knowledge of the magnetic field lines configuration in LHD is also necessary. Alternatively, the amplitude of such rotation may also be assessed with an imaging diagnostics. The result can change in function of the plasmoid studied so it has to be done in a case-by-case basis.

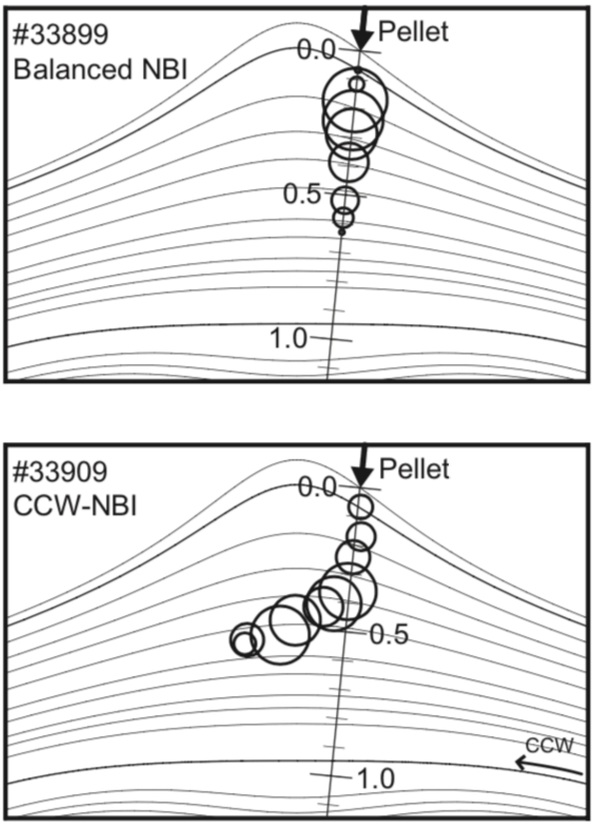

Figure 2.1: Trajectory of plasmoid in function of the heating pattern employed in LHD: balanced NBI vs counter-clock-wise NBI [source: "Observation of pellet ablation behaviour on the Large Helical Device" by R. Sakamoto *et al.* (2004)]

2.1.2 Slices of plasmoid

Up to that point, the exact method used to obtain measurements of slices of plasmoid has been eluded. It is now time to remedy to that omission. As indicated earlier, optical components are responsible for the "spatially-resolved" variable of the system. The idea is to use a plano-convex cylindrical lens to collect the light emitted by plasmoids and to project a part of this light on one end of an optical fiber. The light acceptance cone of the optical fiber and the one-dimensional compressed light collected by the cylindrical lens are such that only slices of plasmoids are processed by the observation system.

Figure 2.2 shows the beam shaping capabilities of a cylindrical lens (left) on three point light sources (right) from the top view perspective. A side view perspective would have been unnecessary because cylindrical lenses theoretically have no resolution power on their plane axis. The three point light sources could be interpreted as three different emission locations at the edges and center of a plasmoid. The photons homogeneously radiated by the light sources are represented with the intensity gradient (whiter equals more photons). In addition to a cylindrical lens, two horizontal walls have been added at the edges of the cylindrical lens to simulate a fixation tube. When they reach the curved side of a cylindrical lens, the photons will get collimated to the other side of the lens to

Figure 2.2: Ray tracing simulation of the beam shaping capability of a cylindrical lens on three discrete light sources. [source: https://ricktu288.github.io/ray-optics/]

form thin lines. In reality, an infinity of light sources that need to be considered so the output of the lens is actually an infinity of lines. However, the present figure illustrates clearly where the beam shaped light rays (flat side of the lens) come from. With an optical fiber, it is possible to select a light source to analyze. For example, it is possible to isolate the central light source from the others by placing an optical fiber on the median axis of the lens. In this example point sources are used but, in reality, some width variable needs to be taken into account. Such width is determined in function of the width and acceptance cone of the optical fiber as well as its distance from the flat side of the lens. As an example, with an optical fiber placed on the median axis of the cylindrical lens and at a reasonable distance from the plane side of the lens, the case shown in fig. 2.2 illustrates how the light emitted from the central region of a plasmoid can be collected. The same concept has been employed to build the observation system used in this thesis.

Figure 2.3 illustrates of how the optics of the observation system work. Plasmoids are hacked into virtual slices when they pass through the field-of-view of the optics thanks to the beam shaping potential of a cylindrical lens (as shown in fig. 2.2) and with the support of an optical fiber. As can be seen from the annotated dimensions, the figure is not to scale. The grayed area going from the optical fiber to the back end side of the vacuum chamber of the LHD represents the effective field-of-view of the observation system. Ablation clouds drawn on the t_1, t_2 and t_3 magnetic field lines of interest represent a plasmoid moving on an unperturbed pellet trajectory at three different timings of the same pellet injection. The circled area annotated by an "X_{cross}" represents the area of interest in which the measurements are conducted. By design, the FOV of the observation system is fixed so the capability to produce spatially-resolved spectral measurements needs at least one more variable to be achievable. Indeed, in order for slices of plasmoid to be obtained, the

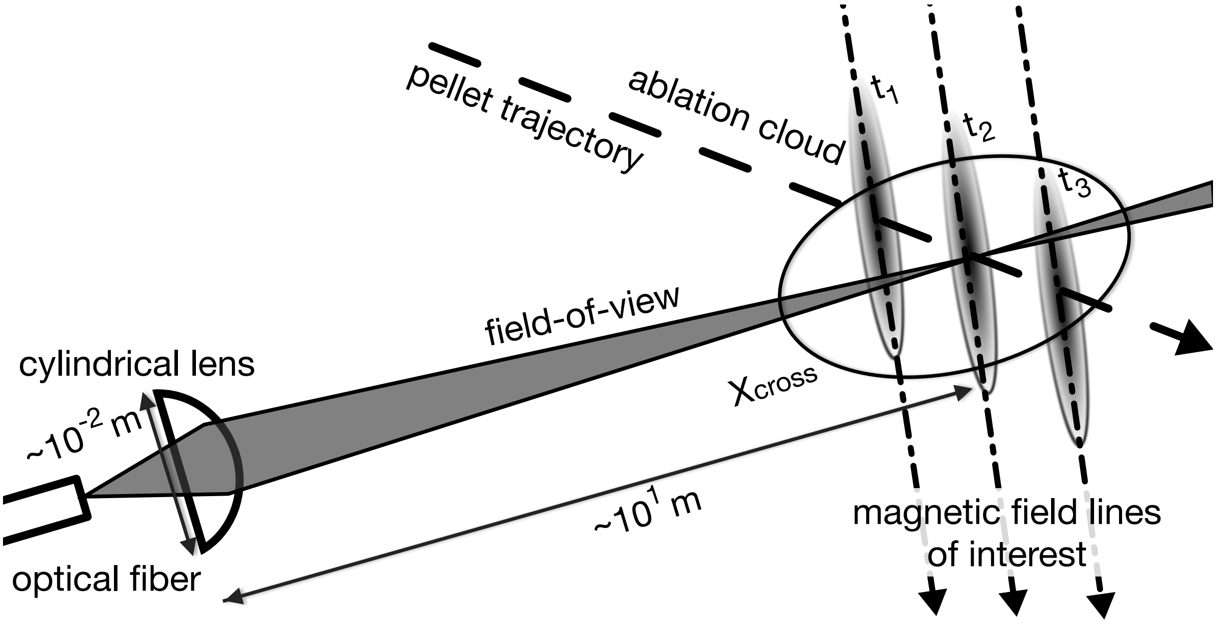

Figure 2.3: Concept for a SRSM-ready observation system (unscaled) [source: "Spatially-resolved electron density measurement in hydrogen pellet ablation cloud" by G. Seguineaud *et al.* (2018)]

plasmoid has to slide through the FOV appropriately. This is of course taken care of by the plasmoid as it moves in the background plasma of the LHD. However, as it has extensively been written already, the manner with which the plasmoids go through the FOV is also important. As thin as the FOV might appears to be in fig. 2.3, it will always possesses a minimum width. This is true even at the center of the X_{cross} region. Incidentally, this minimum width also represents the minimum width of the slices of plasmoid collected by the observation system. Whereas it might be correct to suppose that the width of the slice at the center of X_{cross} is smaller than the ones at its edges, it is usually safe to consider these width as identical for the purpose of this study. The reason behind this is motivated by the fact that the scale of the dimensions involved in the observation are too important for the variation of the width of the slices to matter. A calculation via Thales theorem with dimensions usually found in LHD shows that the difference can be neglected, so can a quick empirical measurement (which is detailed in the next section). Another detail that needs to be pointed out is that no actual image is produced by the optics. It implies that it is not possible to pinpoint where the collected photons exactly come from. The field-of-view of the optics is restricted in one direction due to the use of a cylindrical lens, so the other direction is not modified. Moreover, it is not possible to dissociate the photons once they reach their final destination (i.e. CCD of spectrometer). Consequently, it is not possible to reconstruct any image of the slices of plasmoid. This means that it is also not possible to apply the so-called Abel inversion [22] process to the data as crucial information related to the spatial distribution of the particles inside the slices is lost. The recorded data has to be seen as being an signal integrated over a fixed direction of observation. Data also possess a certain degree of signal integration along the direction parallel to the FOV due to the measurement method itself.

2.2 A new system for Spatially-Resolved Spectral Measurements (SRSM)

In this section, the observation system developed for the purpose of this thesis is described. The observation system is composed of two modules that had to be implemented into the framework of the LHD. These two modules, namely, the optics and the spectrometer, are described.

2.2.1 Optics and width of field-of-view

The optics of the observation system consist of a tube on which a plano-convex cylindrical lens and an optical fiber are mounted. The components selected for this module have been chosen with two criteria in mind. Firstly, the amount of light gathered by the optics needs to be as high high as possible to produce accurate spectra. Secondly, the field-of-view of the optics should be as narrow as possible so that the spectra obtained are spatially-resolved.

Figure 2.4 shows the schematics of the montage used for the observation system with a focus on the cylindrical lens. The optical fiber (left) is placed on the plane side of the cylindrical lens (right), at a distance close to that of the back focal length of the lens. The tube is not drawn to avoid clutter. With an announced clear aperture of 21.5 mm, the cylindrical lens used is a Thorlabs LJ1695RM. The optical fiber used is a multimode fiber which was provided by Dr. M. Goto. With a numerical aperture of 0.2, the resultant acceptance cone of the fiber covers almost completely the clear aperture of the lens that is approximately 44 ± 1 mm away from the entrance of the fiber. Theoretically, the distance between the optical fiber and the back side of the lens should be equal to the diameter of the circle formed by the curvature of the lens. This distance corresponds to the optimal length of the optics so that the width of the FOV is as narrow as possible.

The width of the FOV has been empirically measured. A HeNe laser (632.8 nm) is connected to the back end of the optical fiber and is turned on. Photons are sent to the front end of the optical fiber and projected on the plane side of the cylindrical lens in a conic shape. This conic shape actually corresponds to the acceptance cone of the fiber. Photons going through the lens are refracted and the projection of a narrow band of light can be observed to the other side of the lens. The distance of projection used in the measurement is equal to the distance plasmoids are supposed to reach in LHD (i.e. the aforementioned X_{cross} region). At a distance of projection set to 3600 mm, the width of the projected line is measured at about 14 ± 1 mm. The same measurement has been conducted at 3500 mm and 3700 mm. The same results of about 14 ± 1 mm have been found indicating that the variation of the width in the vicinity of X_{cross} is statistically negligible. With the supposition that that the path taken by the light while going through the lens is reversible, the obtained narrow-lined photons deposition profile must be equivalent to the FOV of the optical system.

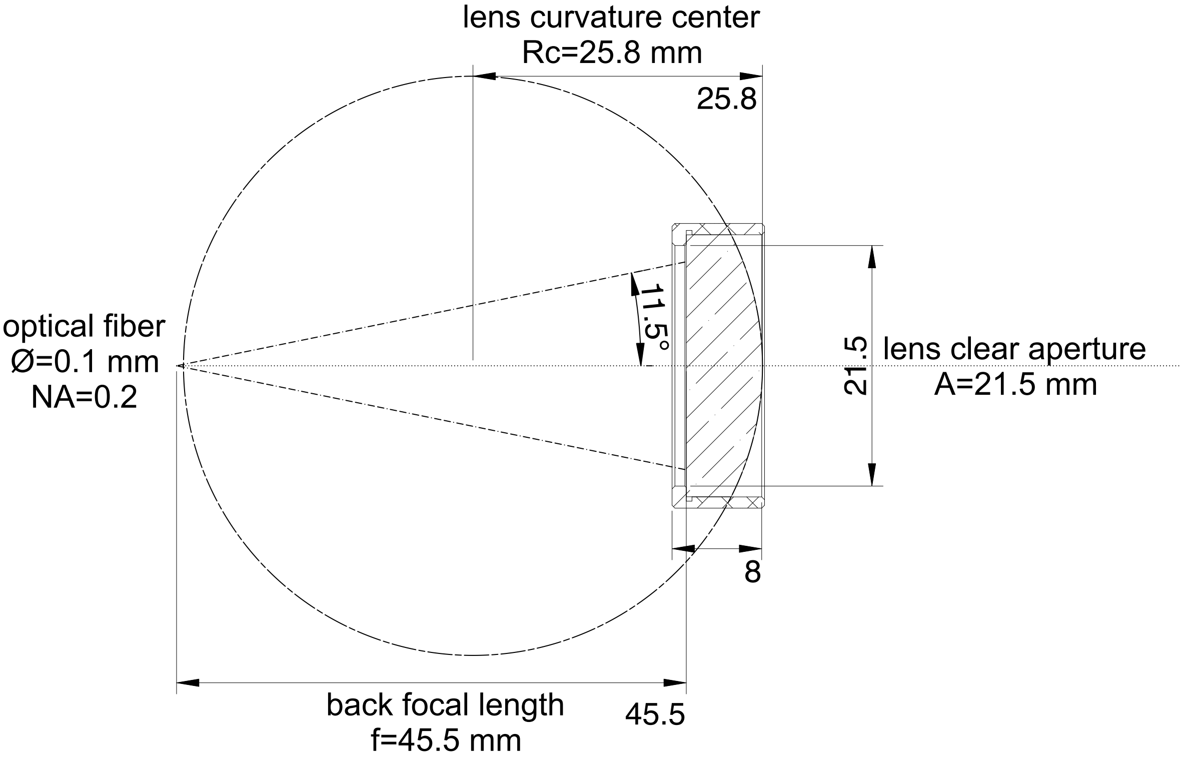

Figure 2.4: Top view of the main optical components for a SRSM-ready observation system

2.2.2 Visible spectrometer and default settings

Under normal conditions, the back end of the optical fiber is connected to a visible spectrometer. This spectrometer has been designed and built especially for the purposes of the experiment. It has been built in the framework of a seminar given by Dr. Keisuke Fujii from Kyoto University.

A top view schematics of the spectrometer is shown in figure 2.5. It is composed of a toroidal mirror grating and a line camera. The camera is fixed on the outer side of the exit wall. The spectrometer casing measures 200 x 170 x 100 mm. Its walls are made from aluminum plates of 8 mm of thickness, except for the top plate which is 2 mm thick. The back side of the optical fiber is directly connected to the entrance wall using a Thorlabs SM1FC adapter plate mounted on a Thorlabs CP02/M slit holder. No entrance slit is actually used as photons are sent on the grating directly from the optical fiber. Position fine-tuning can be adjusted via stages placed under the Shimadzu P0550-01TR grating. The stages for adjustment comprise an Optosigma KKD-60C pivot stage and an Optosigma TSD-601S translation stage. The illumination cone at the back end of the optical fiber covers completely the effective surface of the grating for maximum brightness. To avoid any interference from stray light, the inner walls of the spectrometer have been covered by black revetments (sides and top plate) and a black colored spray (bottom plate). The grating has been specifically designed for flat-field polychromators to diffract any incident light comprised between 340 nm to 900 nm and reflect it on a flattened plane beam. The diffracted light is then projected on the two CCD arrays of a Neopt NCAM2-BLD-04K070CL dual lines camera. The two CCD arrays of the camera are stacked one on the top of another and each CCD array contains 4096 pixels of 7x7 μm. The detector is set to a so-called 2x2binning mode where 4 adjacent pixels are combined into a bigger pixels-block. As a result, the spectrometer acts as if it had one CCD array of 2048 pixels measuring 14x14 μm each. The 2x2binning mode has for advantage to increase the sensitivity of the spectrometer to the price of resolution power. The spectrometer communicates with an acquisition computer via two SDR MiniCameraLink connectors (as can be seen on the back of the camera in fig. 2.5). The acquisition computer is equipped with an AVAL APX-3323 acquisition card and uses a proprietary software to upload any desired profile to the camera. The acquisition card also has a D-SUB 15 pin connector used to retrieve the trigger input sent from the LHD control system when a discharge begin. Data acquisition and exportation is taken care of by a home-made C++ program built around the AcapLib2 library which is available on the website of the manufacturer of the acquisition card.

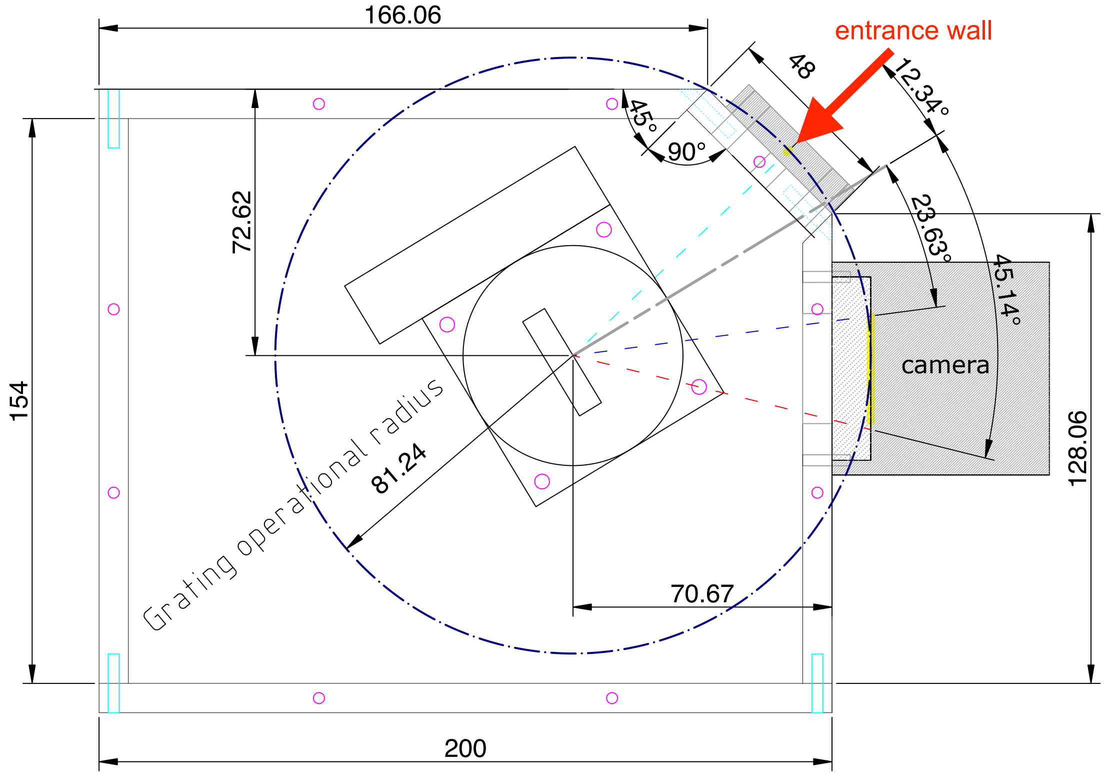

Figure 2.5: Top view of the schematics of spectrometer. The three main components are clearly visible: the optical fiber connected to the entrance port, the grating setup on its fine-tuning stage and the camera fixed to the exit port.

A primary objective of this spectrometer is to output processable data at a rate that is fast enough to catch enough exploitable data-frames. In consequence, the timings of the camera in regard to the acquisition time and the exposure time are set to 11 and 14 μs, respectively. Also, the data output pattern and bit-depth of the detector are set to 4 taps and 12 bits, respectively. Another objective of this spectrometer is to output spectra emitted from slices of plasmoid in a wavelength range that surrounds the Balmer emission lines of hydrogen plasmas. On paper, the camera is able to follow up with its announced 350 nm to 1050 nm operating wavelength range. The grating is not a problem as well with its optimal operating wavelength range announced to be between 340 nm and 900 nm.

As such, the figure 2.6 shows the template of a spectrometer (provided by Shimadzu) capable to observe the first order light emitted from plasmoids. Estimation of the free spectral range of the spectrometer shows that the first order light might overlap with the second order light. This is however not of concern as low brightness levels are expected from the contributions of the second order, especially where the orders overlap. The zeroth order light is not a problem either as it is a specular refraction (i.e. not diffracted) and the angle it is sent at is far from the angles of interests. When observing plasmoids, it is supposed that only the light emitted from a pure hydrogen plasma will be collected.

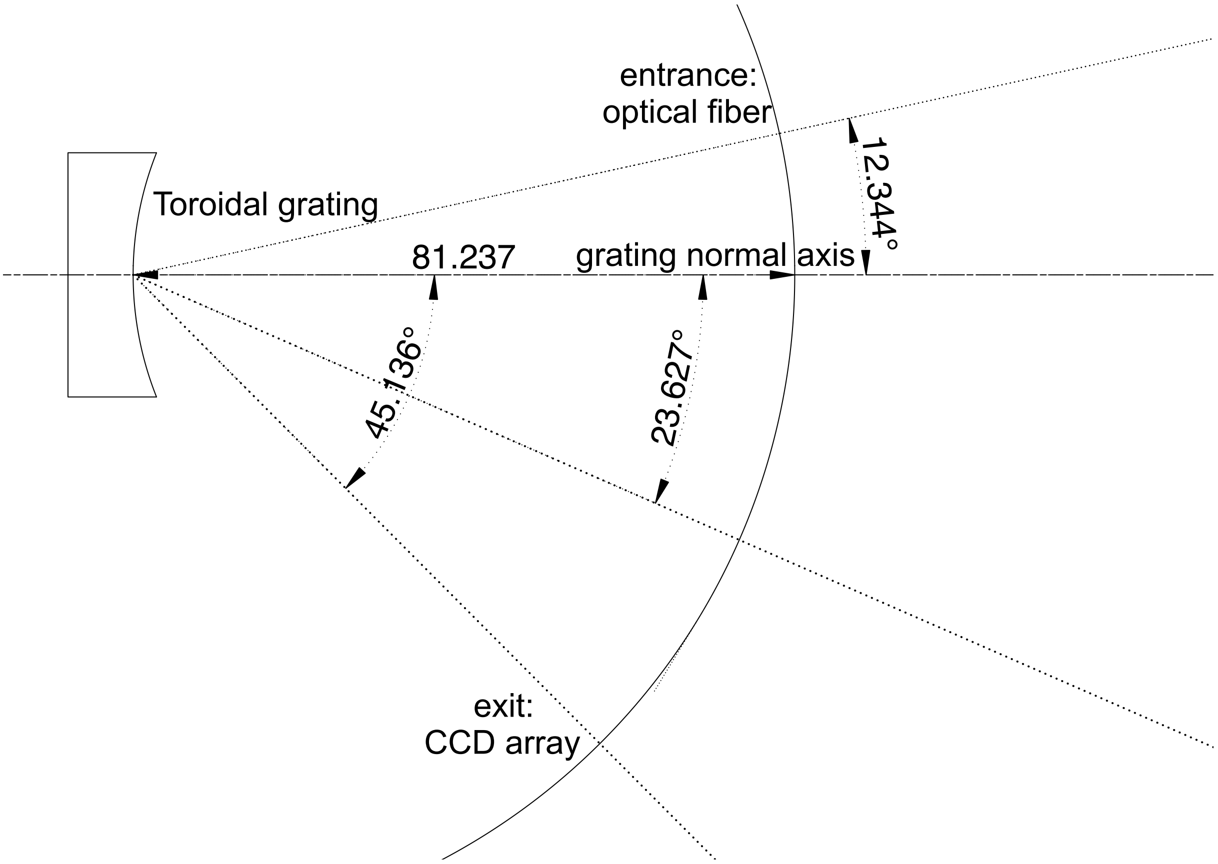

Figure 2.6: Design of spectrometer as recommended by the manufacturer of the grating [source: Shimadzu website or grating manual guide]

Entrance port misalignment

The blueprint used to create the spectrometer is slightly different from the template proposed by the manufacturer of the grating. For simplification purposes, the geometry of the box of the spectrometer has been defined so that the angle between the entrance wall has a 45.0 degrees angle with the exit wall. As shown in figure 2.7, a misalignment of about 1.5 degrees exists between the line-of-sight of the optical fiber and the grating normal axis. Hopefully, such misalignment does not modify the angle of attack of the incident light beams. Moreover, the illumination cone of the optical fiber is still projected on most of the diffracting surface of the grating (there is a 2 mm region around the grating plate which is not covered by grooves).

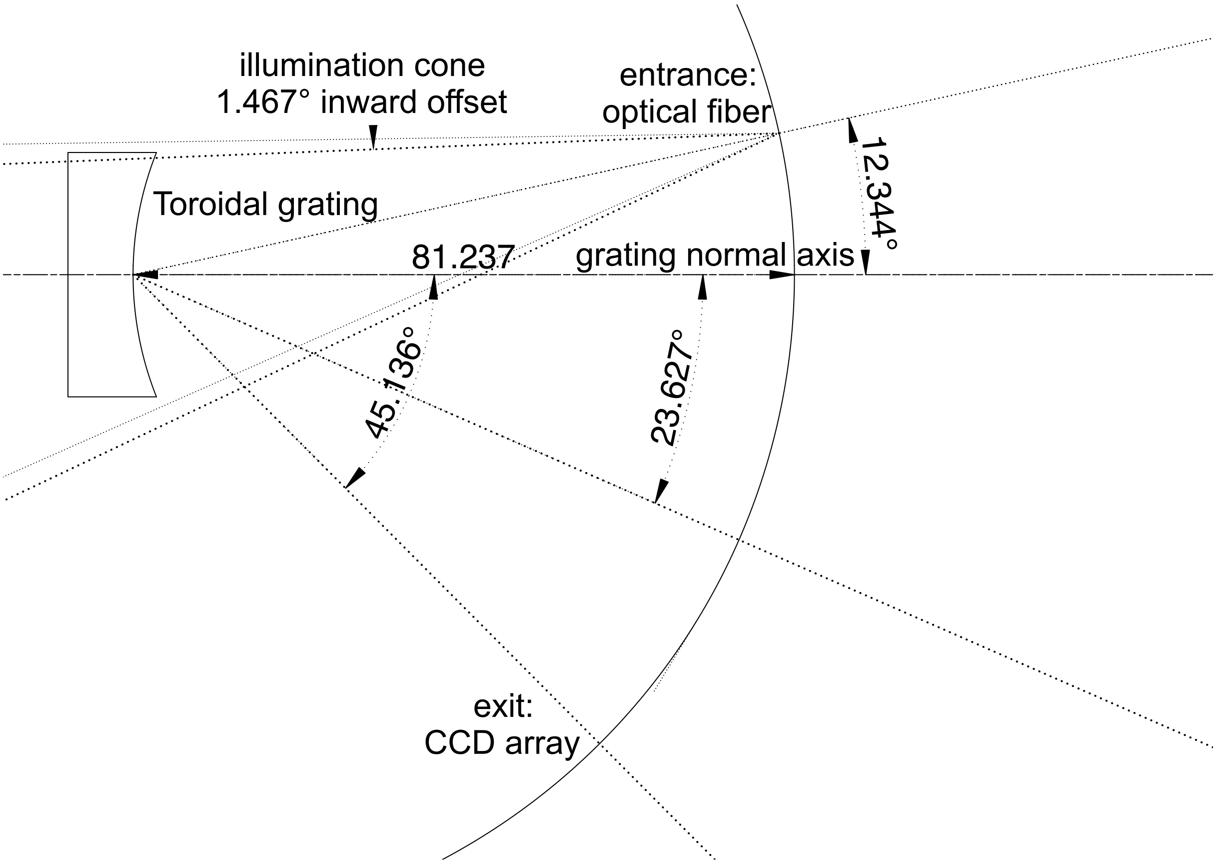

Figure 2.7: Light ray tracing from entrance port to grating of spectrometer with focus on the offset misalignment of the entrance port (unannotated dimensions are given in mm)

Exit port misalignment and fine-tuning

The CCD array of the detector is aligned on the lower end of the projection of the spectrum because this is where the emission lines of interests are most likely to be found. As shown in figure 2.8, the length of the CCD array of the detector is technically long enough to cover all of the emission lines of the Balmer series. If kept as is, the spectrometer should be able to detect correctly the first Balmer emission lines of a hydrogen plasma. However, the detection of the so-called transition to the continuum located toward the latest lines

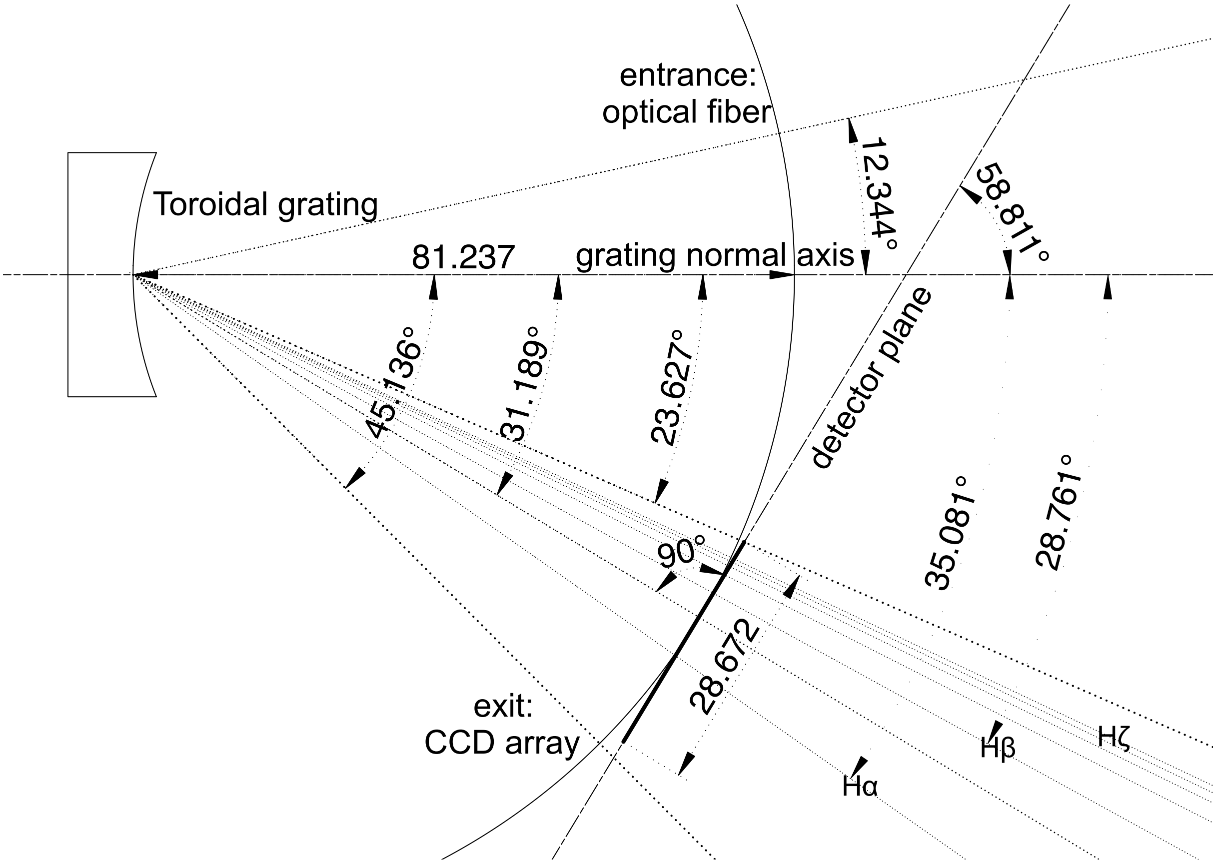

Figure 2.8: Light ray tracing from entrance port to camera CCD of spectrometer with focus on diffraction pattern (unannotated dimensions are given in mm)

might be complicated. To do so, it may be necessary to slide the projected spectrum on the CCD array for it to cover a more appropriate wavelength range.

It is possible to yaw, pitch and roll the grating as well as translate it along the grating normal axis with the stages schematized in figure 2.9. If used, the projection of the spectra on the exit wall can be shifted by a few millimeters outward (i.e. further away from the normal of the grating). The amplitude of the modification can only be very roughly known. If the worst case scenario where the maximum pitch rotation and translation is supposed, i.e. ± 3 degrees and ± 6.5 mm, respectively; the transition to the continuum of the second order still won't reach the Balmer-α line of the first order. As a matter of fact, fine-tuning has been applied almost exclusively on the pitch angle so that the grating is looking between 1.7 and 3.0 degrees more to the outer region of the casing compared to its default location. Normal translation has been slightly changed (less than 1.0 mm) backward to compensate for the roll angle correction (less than 0.4 degrees). Such corrections have been conducted because the projection of the spectral plane on the exit wall was not perfectly aligned with the CCD array of the detector. Other sources of misalignment related to the manufacturing process are neglected because judged to be too small (less than 0.01 mm) to have any contribution.

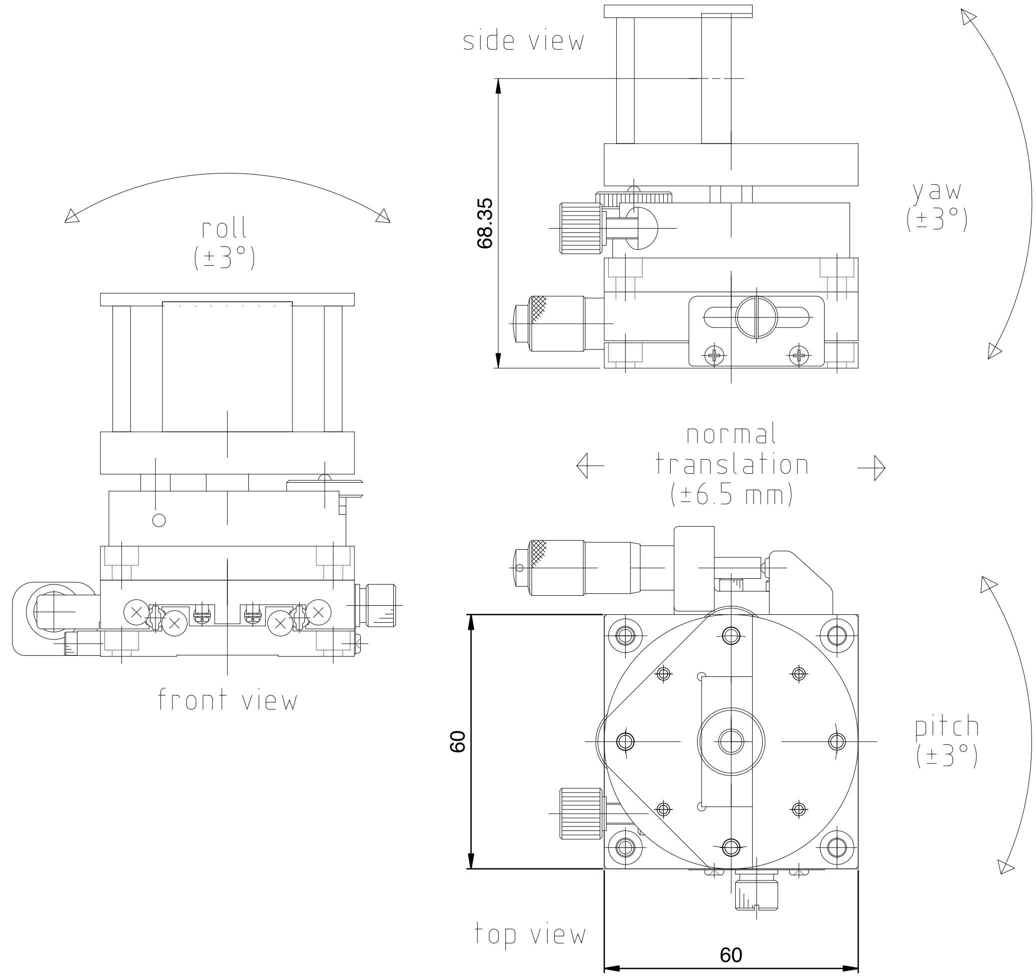

Figure 2.9: Schematics of translation-rotation stages for grating of spectrometer (unannotated dimensions are given in mm)

2.3 Installation of a SRSM-ready observation system in the Large Helical Device

In this section, specifics about the fuel pellet injection experiments in LHD are given. Details of the pellet injection system installed in LHD have already been given in chapter 1, Here, focus is put on the diagnostic wall and the support flange fixed on the observation port used for the experimental setup introduced in the previous section.

2.3.1 Diagnostic wall 3-O

The diagnostics wall of the LHD on which pellet injection experiments are conducted has a series of observation ports that are usable for diagnostics purposes. However, due to some technical restrictions only one port has been judged adapted for the implementation of the observation system. Moreover, Implementing the system into the LHD framework does not only consist in fixing the optics of the system on the observation port. As mentioned previously in this chapter, the spatially-resolved capability of the observation system needs to be taken care of by the optics. It implies that the position of the optics needs to be carefully calculated In addition, an imaging diagnostics has also been added to the system for visual feedback purposes. Its implementation into the ecosystem of the spectroscopic diagnostics is also subject to some restrictions. Data obtained from this imaging diagnostics is generously compiled by Dr. Gen Motojima.

Figure 2.10 shows the top (left) and front (right) views of the diagnostics port 3-O of the LHD. This port is mainly dedicated to experiments related to pellet injection. A focus is put on the observation system developed during this thesis. On the left figure, one

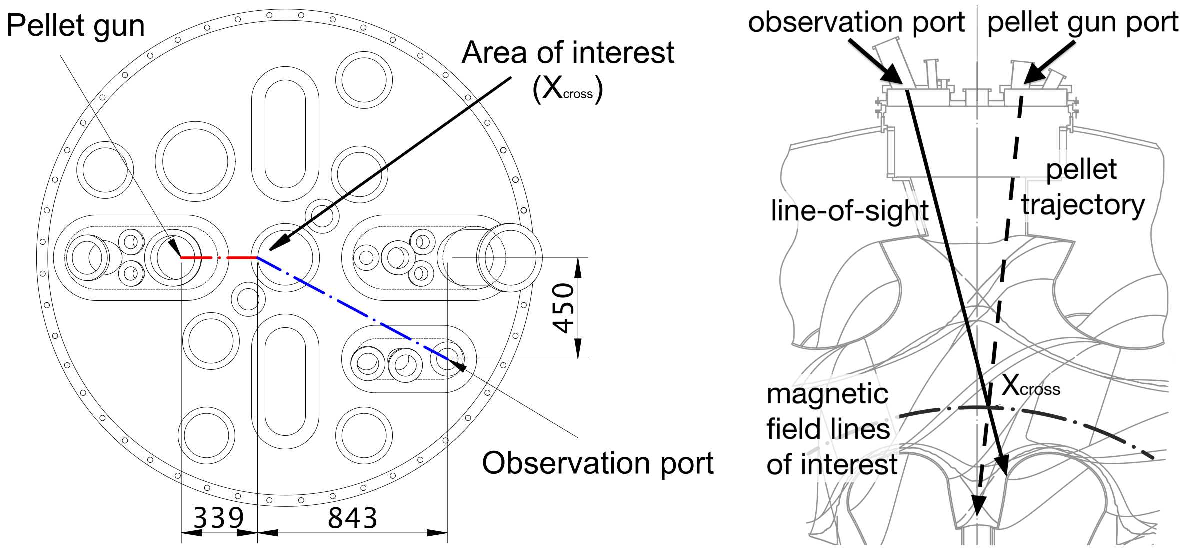

Figure 2.10: LHD 3-O diagnostics wall viewed from the front (left) and vacuum vessel section viewed from the top (right) (unannotated dimensions are given in mm)

can recognize the layout of the pellet injection experiment presented in fig. 1.2. The pellet trajectory represented by the long dashed arrow meets the magnetic field lines of interest represented by the dash-dotted line in a defined region of interest in the background plasma of the LHD. The region of interest, or X_{cross} set at $R_{\text{ax}} = 3.6$ m has been chosen accordingly to the needs of the experiment given in the first section of this chapter. The notable additions to the figure are the location of the observation port and the line-of-sight (continuous arrow) of the observation system. The line-of-sight of the observation system needs to be as such that it meets the pellet trajectory at X_{cross}. Whereas the pellet trajectory is just an horizontal line that makes an angle of approximately 6° with the median axis of the diagnostics wall 3-O, the line-of-sight of the observation system needs to take a more complicated path to reach X_{cross}. Indeed, as can be seen from the right figure, the observation port the optics are fixed on is not only on the opposite side of the wall, but it is also on a different horizontal plane than that of the pellet gun. With that said, a support flange has been built to direct the diagnostics toward the X_{cross} region.

2.3.2 X_{cross} and support flange

The support flange has been built with the intent to direct the line-of-sight of both the optics of the observation system and of the imaging diagnostics toward the X_{cross} region.

This specific X_{cross} is chosen because it is a region where the magnetic field lines appear to be almost perpendicular from the point of view of the observation port. Moreover, although the core region is not often visited by plasmoids as they dissolve into the background plasma before being able to reach it, those that do are susceptible to be in a stable and non expanding phase. This is of importance because it is preferable for the plasmoids to not change while they are being measured (cf. first section of chapter 2). An important point to precise is that this X_{cross} at $R_{\text{ax}} = 3.6$ m is not relevant in every configurations in LHD. Indeed, a detail that has not been given is that it is possible to change the location of the core plasma in the vacuum chamber of the LHD. Among all of the different magnetic configurations possible, $R_{\text{ax}} = 3.6$ m has been chosen because it is one of the magnetic configurations that is used the most. That being said, it is now time to introduce the support flange.

Figure 2.11 shows the side view of the support flange. It consists of a main cylindrical block of stainless steel in which a series of holes have been pierced. There are 7 diagnostics holes in total. A principal hole which is located along the major axis of the cylinder and six smaller holes that are symmetrically spread around the principal one. Optics can be inserted into the holes to have access to the inside of the vacuum vessel of the LHD. The central hole is reserved for the optics of the spectroscopic diagnostics while the peripheral ones are for the imaging diagnostics. The angles of inclination are determined from a datafile that contains the magnetic field lines configuration in the vacuum vessel of the LHD when $R_{\text{ax}} = 3.6$ m. In addition, the support flange of another experiment was

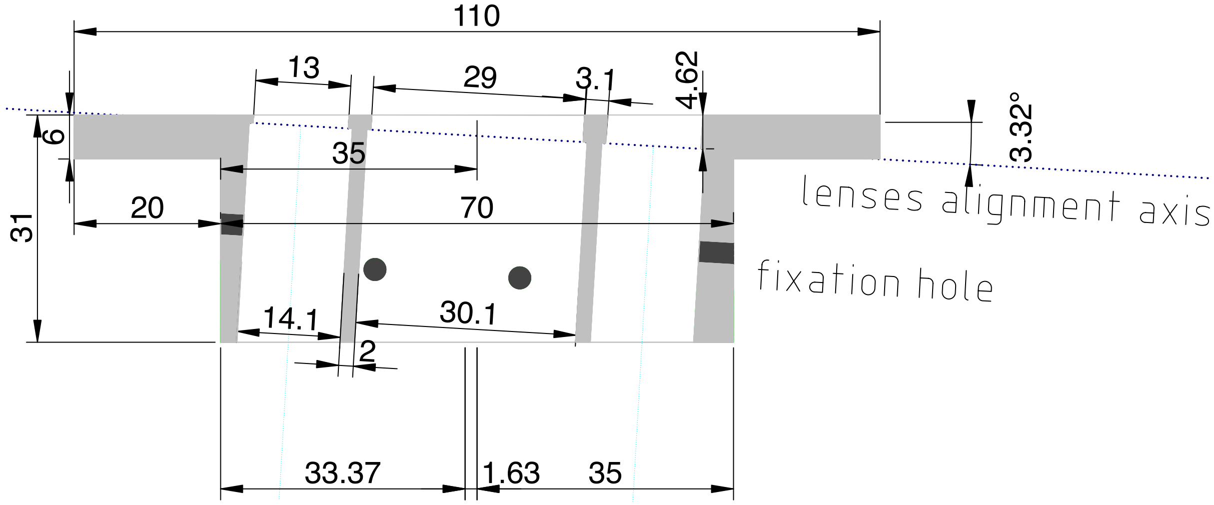

Figure 2.11: Side view mid-cross section of the schematics for the optics support flange (unannotated dimensions are given in mm)

already fixed on the observation port, prior to this one. In order to let the possibility to switch rapidly between the two experiments, the original support flange has not been taken off. It means that the angles of this other support also needed to be considered into the calculations. Datafiles of the magnetic field configuration, the other support flange as well as the fiberscopes of the imaging diagnostics have all been provided by Dr. Gen Motojima.

In figure 2.12, the adapter flange, a component dedicated to host the support flange is also observable. It is a ring shaped aluminum component that is pierced so that its orifices match with the support flange and the observation port it is fixed on. Graduations to indicate the angle of rotation of the block are also observable, carved into the component (marked on the right side of the support flange). It can be seen from fig. 2.11 and 2.12 that the adjustments of the support flange are done via two angles. The most important adjustment angle is built-in into the main block, fixed at about 3.3° to the right. This angle has for role to compensate the angle that the support flange already installed has. The second angle is an adjustable roll angle destined to correct the “up-down” orientation of the optics. It works by rotating the main block in the clock-wise or counter-clockwise direction. It possesses a leeway of ± 5°, with a theoretical sweet-spot calculated to be between 1.6° and 1.7° in the clockwise direction.

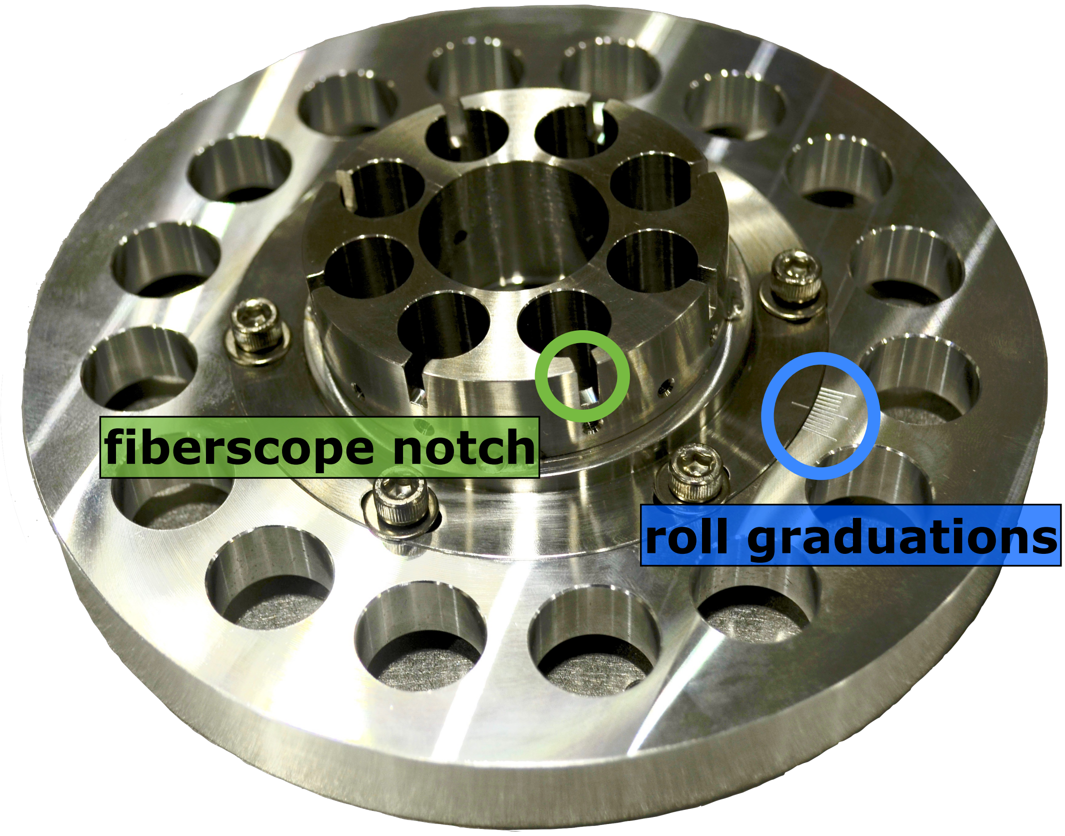

Figure 2.12: Picture of adapter flange fixed on its support flange

Roll angle considerations and fine-tuning

The roll angle can also be used to fine-tune the orientation of the FOV of the observation system to compensate for any eventual misalignment. It is not necessary to use it as the same function can done by adjusting the position of the tube that contains the optics of the spectroscopic diagnostics. However, the latter option is not advised as the support flange was not designed for this to happen.

Indeed, by design, the “up-direction” of the fiberscopes have been set so that they are directed outward of the main block via notches. The notches can clearly be seen on the main block in fig. 2.12. When placed correctly, the up-down direction of the two fiberscopes at the top and bottom of the central hole are supposed to be aligned to the up-down direction of the cylindrical lens of the optics. Like so, it is possible to process the output of the imaging diagnostics relatively easily so that it corresponds to what is also observed by the spectroscopic diagnostics. Such step is actually conducted in chapter 4 to confirm the spatial resolution capability of the observation system.

Obviously, a misalignment between the optics and the fiberscopes can not be corrected with the roll angle. Such misalignment needs to be corrected manually, by rotating appropriately the tube that contains the optics of the spectroscopic diagnostics. Sadly, such manipulation is difficult, or even impossible to do when experiments are conducted.

Chapter 3

Calibration and preprocessing of experimental data

Raw spectra produced by the experimental system have to be converted into a physical unit before being spectroscopically analyzable. Raw spectra are given in digital number (or count) per pixel. It is necessary to convert into a unit which is understandable by the spectral model that will be introduced in chapter 5. The calibration process is split into two phases. On one hand, the per pixel basis of the dataset needs to be converted into the unit of a wavelength range (e.g. [nm]). For that reason, an experimental approach as well as a ray tracing method are used. The experimental approach relies on the analysis of the spectra obtained from hydrogen plasmas during their recombining phase. Such events are relatively well known and are of common occurrence in LHD. The ray tracing method which is mostly used from confirmation purposes uses the blueprint of the spectrometer as reference. On another hand, the digital number basis of the dataset needs to be converted into the unit of spectral power (i.e. [$\mathrm{W.m^{-1}}$]). To do so, a calibration lamp of known spectral radiance is used. A point to consider is that the unit of spectral radiance is usually written as [$\mathrm{W.m^{-2}.nm^{-1}.sr^{-1}}$]. The spectral radiance is conveniently avoiding the "geometrical aspect" associated to the measurement of the light emitted by the calibration lamp. However, this aspect has to be taken into account when processing the data obtained from the observation device. While this calculation step is not directly linked to the calibration procedure, it is more related to the pellet injection experiments themselves. Nonetheless, choice has been made to implement such calculation into the final calibration frame to simplify the data analysis process done later on in the study (cf. chapters 5). An additional information can be extracted from this calibration procedure. Indeed, it is actually possible to derive the instrumental function of the observation system from the spectra collected in the recombining phase.

The third chapter is divided into three sections. The first section is dedicated to the wavelength calibration procedure. The second section is dedicated to the intensity calibration procedure. Eventually, the calibration frame used on the data is also reproduced. The third section is dedicated to characterize the instrumental function of the observation system.

3.1 Wavelength calibration via experimental and rays tracing methods

In this section, two wavelength calibration procedures are conducted on the data of the observation system with the intent to produce a wavelength calibration frame. Firstly, the calibration is done experimentally from spectra obtained by recording the recombining phase of a LHD plasma discharge. Secondly, the calibration is done via a rays tracing method for verification purposes.

3.1.1 Wavelength calibration: experimental approach

When the spectrometer of the observation system records data, the collected photons are output in a datafile on a "count number by pixel" basis. Lets write the previous statement as C(pixel), where (pixel) represents the unit with which the count number C is sorted. For any datafile to be properly interpretable, a first required step consists of converting the data so that C(pixel) → $\mathrm{C}(\lambda)$, where $\mathrm{C}(\lambda)$ is now sorted with the unit of wavelength [nm].

However, even if such conversion can be done directly relatively easily, what is actually happening might not be that evident to grasp completely. On one side, there is the unit of pixel, a discrete entity which possesses a measurable and finite size. On the other side, there is the unit of wavelength which is mathematically continuous and theoretically infinite. The logical source of this discrete/continuous dichotomy is that one pixel can cover a theoretically infinite gradient of wavelengths that are comprised between a certain wavelength range $\lambda \pm d\lambda$ such that

$$\mathrm{C}(\mathrm{i}) = \int_{-d\lambda_\mathrm{i}}^{+d\lambda_\mathrm{i}} \mathrm{C}(\lambda)\, d\lambda\,, \tag{3.1}$$

where i and λ_i represents the considered pixel number and the limits of its wavelength range, respectively.

Put into context, the value of $d\lambda$ is linked to the size of its associated pixel, and, when photons emitted from a plasma are collected by an array of pixels, some distinctive patterns may appear. For example, in the case an hydrogen plasma discharge observed in the visible range, it is highly probable to find concentrations of adjacent pixels with a higher count number than others. In a spectroscopic language, such event is referred to as an emission line, and the analysis of its intensity, shape and location is an important aspect on the research of plasma spectroscopy. The wavelength λ_0, located at the center of these emission lines can be determined very accurately with a theoretical model. Sadly, the same cannot always be said about the spectroscopic data because of the aforementioned discrete/continuous dichotomy that exists between C(pixel) and $\mathrm{C}(\lambda)$. To illustrate that point, lets consider a packet of photons which corresponds to a certain emission line hits an array of pixels. The probability that the photons of wavelength λ_0 hit the center of a pixel is very unlikely. As a result, packets of photons will be collected by adjacent pixels in such a way that the observed emission line does not correspond to the real one. This phenomenon is problematic when trying to rebuild the wavelength axis of a dataset via the analysis of the relative distances between different emission lines as is attempted in this section. Hopefully, it is possible to mitigate this offset by fitting the observed emission lines with an appropriate function (e.g. gaussian distribution function) and, ultimately, build a relatively accurate C(λ) profile (i.e. spectrum over a complete array of pixels).

Another phenomenon linked to the way the spectrometer used work needs to be considered. As is the case here, spectrometers can rely on the properties of at least one diffraction grating to project spectra on a camera. However, because of how photons are refracted when changing medium, the diffraction angles of the photons depend on their wavelength. As a result, spectra projected on the array of the camera is non-linearly spread. In the spectroscopic world, a relation frequently used to formalize this phenomenon is referred to as the reciprocal linear dispersion, and is expressed as

$$D = \frac{d\lambda}{dx} = \frac{cos(\beta)}{Nmf}\,, \tag{3.2}$$

where D is the reciprocal linear dispersion given in [nm.mm^{-1}]. β corresponds to the angle of the diffracted photon beam relatively to the grating normal. N, m and f are the grooves frequency parameter of the grating, the order of diffraction considered and the focal distance between the grating and the camera, respectively.

Ultimately, it is possible to verify the validity of the wavelength calibration procedure via a comparison of the experimentally derived reciprocal linear dispersion coefficients (obtained from the experimentally built C(λ) profile) with the theoretically estimated ones (obtained from the equation 3.2).

3.1.2 Case of study: LHD plasma discharge #142281

With the observation system appropriately configured, the wavelength calibration procedure can be conducted with the support of recorded spectra of the recombining phase of an especially bright LHD plasma discharge.

Eventually, all MCF plasmas will lose their confinement properties, announcing the termination of a discharge. When this happens, the plasma in the vacuum vessel will go through what is referred to as a recombining phase. Under certain situations, the recombining phase happens so abruptly that a very intense visible light can be observed. During a recombining phase, the electron temperature and density of the plasma drop drastically, decreasing its ionization level. In plasmas composed of isotopes of hydrogen, nuclei and electrons recombines into neutral particles via relatively intense radiative processes in the visible spectrum range. The produced emission lines are very useful for wavelength calibration purposes due to their very thin lineshapes. Indeed, with a low electron density, the Stark-broadening is reduced. In addition, the temperature drop implies that the so-called Thermal Doppler broadening is reduced as well. Plasmas like these are ideal for calibrating observation systems that have a low spectral resolution power such as the one used here.

Figure 3.1 shows the so-called waveform of a LHD plasma discharge selected for this wavelength calibration procedure. From top to bottom, the different plots represent the line averaged electron density in (red continuous line), the plasma electron temperature around the core plasma region at $R_{\text{ax}} = 3.6$ m (red dots) and the emission intensity profile of the plasma (black continuous line). All are expressed in function of time in [s], where the trigger time $t = 0$ s corresponds to the beginning of the shot #142281. It is supposed that the emission profile of the deuterium plasma is dominant because it can be seen in the lower graph that the ratios $\frac{\text{D}}{\text{H+D}}$ (pink dots) and $\frac{\text{D+H}}{\text{D+H+He}}$ (yellow dots) indicate that deuterium was the main component of the plasma for all the duration of the discharge. It is easily observable from the emission intensity profile that the recombining phase of this plasma happens between the 5.6 and 5.7 s marks. As expected from such phase, the electron temperature, and especially, the density plummet quickly. On the contrary, the radiative processes occurring in the plasma of deuterium peak significantly as the number of recombining events skyrocket and die out as fast as they have appeared due to a lack of ionized particles in the vacuum chamber of the LHD. The discharge #142281 seems to be an appropriate candidate for wavelength calibration purposes. Although the level of intensity involved during the recombining phase is brighter than what is usually expected for a background plasma, it is still far weaker than the light emitted by plasmoids. As such, the parameters of the spectrometer set to observe plasmoids are not adapted and

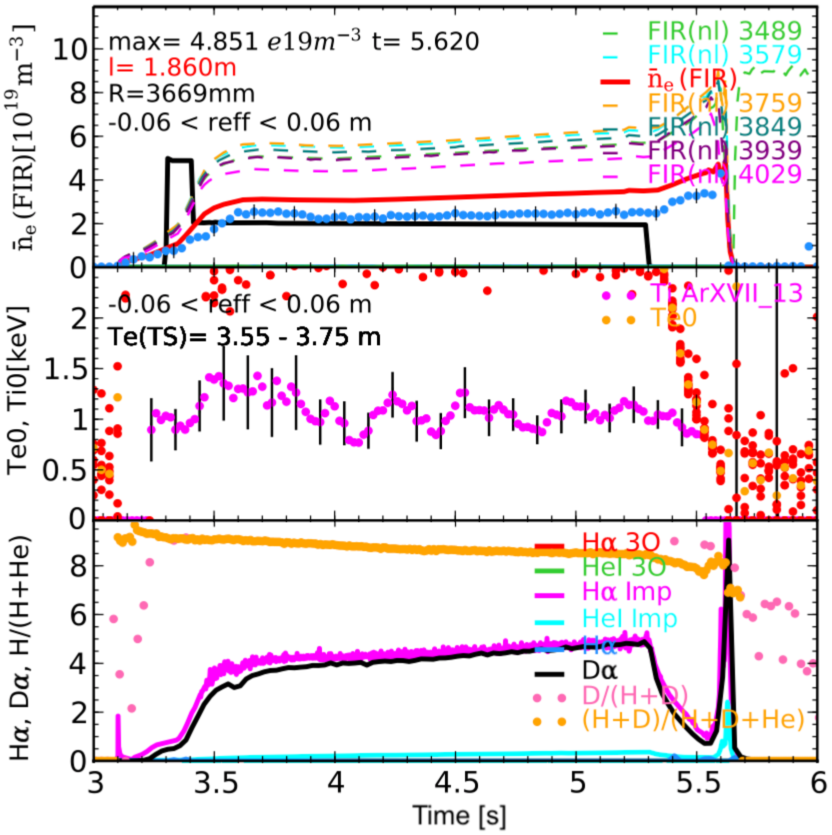

Figure 3.1: Electron density, electron temperature and light emission intensity waveforms of LHD plasma discharge #142281 with intense recombining phase

need to be switched to an acquisition and exposure times of 5.000 and 4.997 ms/frame, respectively.

Figures 3.2 show a spectrum recorded during the recombining phase for a deuterium plasma (discharge #142281) observed in LHD with the newly developed observation system. Raw spectra where the contribution of the dark-noise (DN) frame is kept (left) and removed (right) are plotted. A visual comparison of the two spectra hints at the unusual behavior of the dark-noise frame of the camera mounted on the observation system. The corresponding DN frame is shown in figure 3.3. The dark-noise, or DN frame, should not be confounded with the background plasma radiation. A DN frame corresponds to the frame that is output by a camera when no light is shone on its sensor, or pixels array. Three irregularities in the pixels array can be observed on the DN frame near the pixel numbers 250, 1000 and 1250, respectively. Overall it is possible to that the baseline of the signal can be split into three distinct regions. The central region found between the pixel numbers 750 and 1750, has a steeply sloped baseline and is surrounded by two plateau-like regions. The plateau-region found on the superior side of the central region is significantly noisy compared to the other one. The peculiar pattern of this DN frame is not without consequence for the rest of the study. Such pattern can be problematic under low-light conditions, especially in regard to the very noisy region. Because of the nature of pellet injection experiments, it can be difficult to analyze all of the spectra because of the poor signal/noise (S/N) ratio often encountered under low-light conditions. Indeed, low-light conditions and quick intensity variations are common occurrences in pellet injection experiments, especially a few moments before and after plasmoids are detected by the observation system.

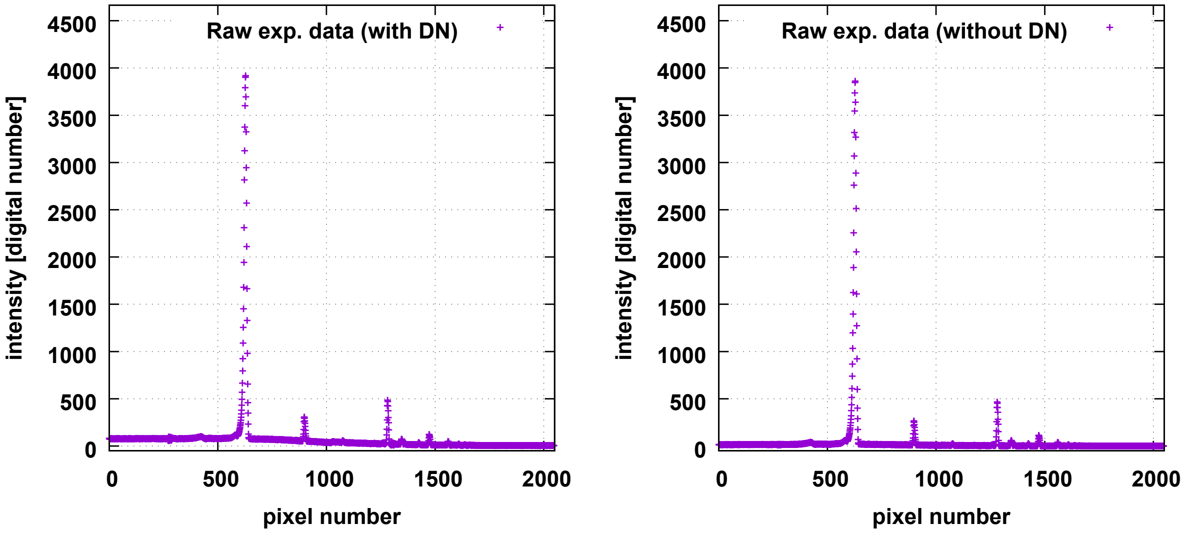

Figure 3.2: Raw data of spectrum collected from the recombining phase of LHD plasma discharge #142281 with (left) and without (right) the dark-noise contribution

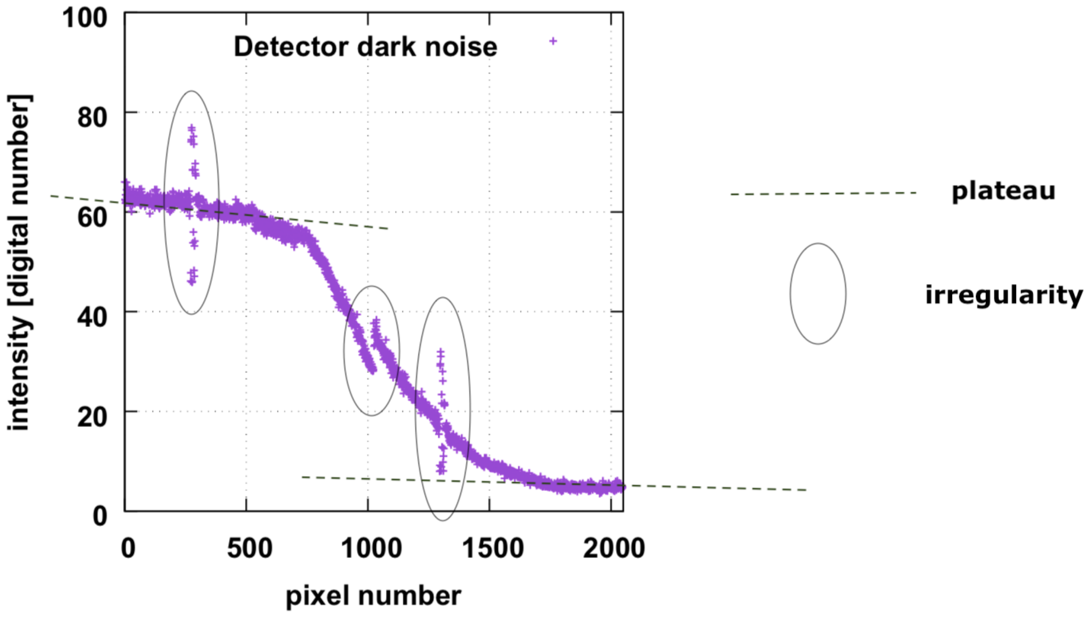

Figure 3.3: Dark-noise frame of Neopt camera set to 2x2binning mode and exposure time of 3.997 ms/frame (average of 500 frames)

Figure 3.4 shows the case without DN of the spectrum introduced in fig. 3.2 with the location of the emission lines center of the four first Balmer series emission lines. The contribution of a supposed linear continuum radiation is also subtracted from the spectrum so that its baseline is aligned with the x-axis origin. Locations of the peaks

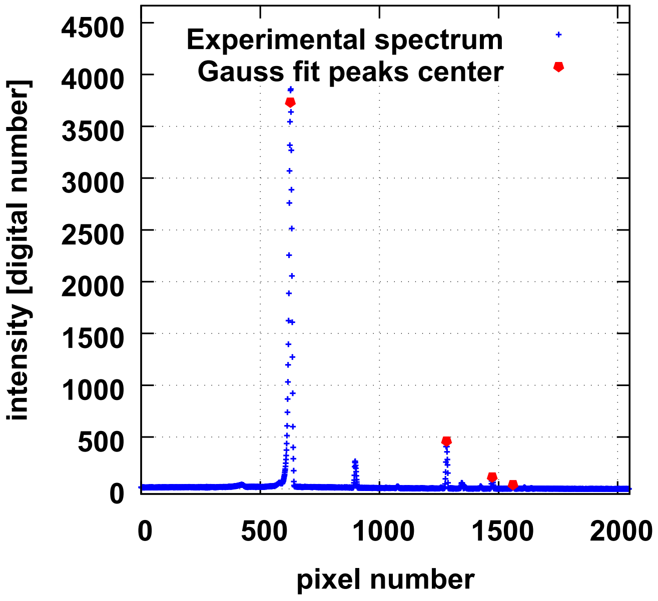

Figure 3.4: Raw data of spectrum collected from the recombining phase of LHD plasma discharge #142281 (without DN) with position of lines center

associated the emission lines are extracted from the spectrum as per the explanation given in the previous subsection.

Figures 3.5 show the isolated experimental spectra (crosses) of the Balmer-α, β, γ and δ emission lines with their gaussian fit (continuous lines). For the sake of simplicity, the lineshapes are supposed to be regular enough so they can be analyzed with gaussian fits irrespectively to their noticeable asymmetry. Thanks to the fitting results, each peak can now be associated to a more accurate real pixel number (i.e. not an integer but a real number). From this point, the identified peaks are associated to their respective wavelength. For example, the peak thought to correspond to the Balmer-β line located

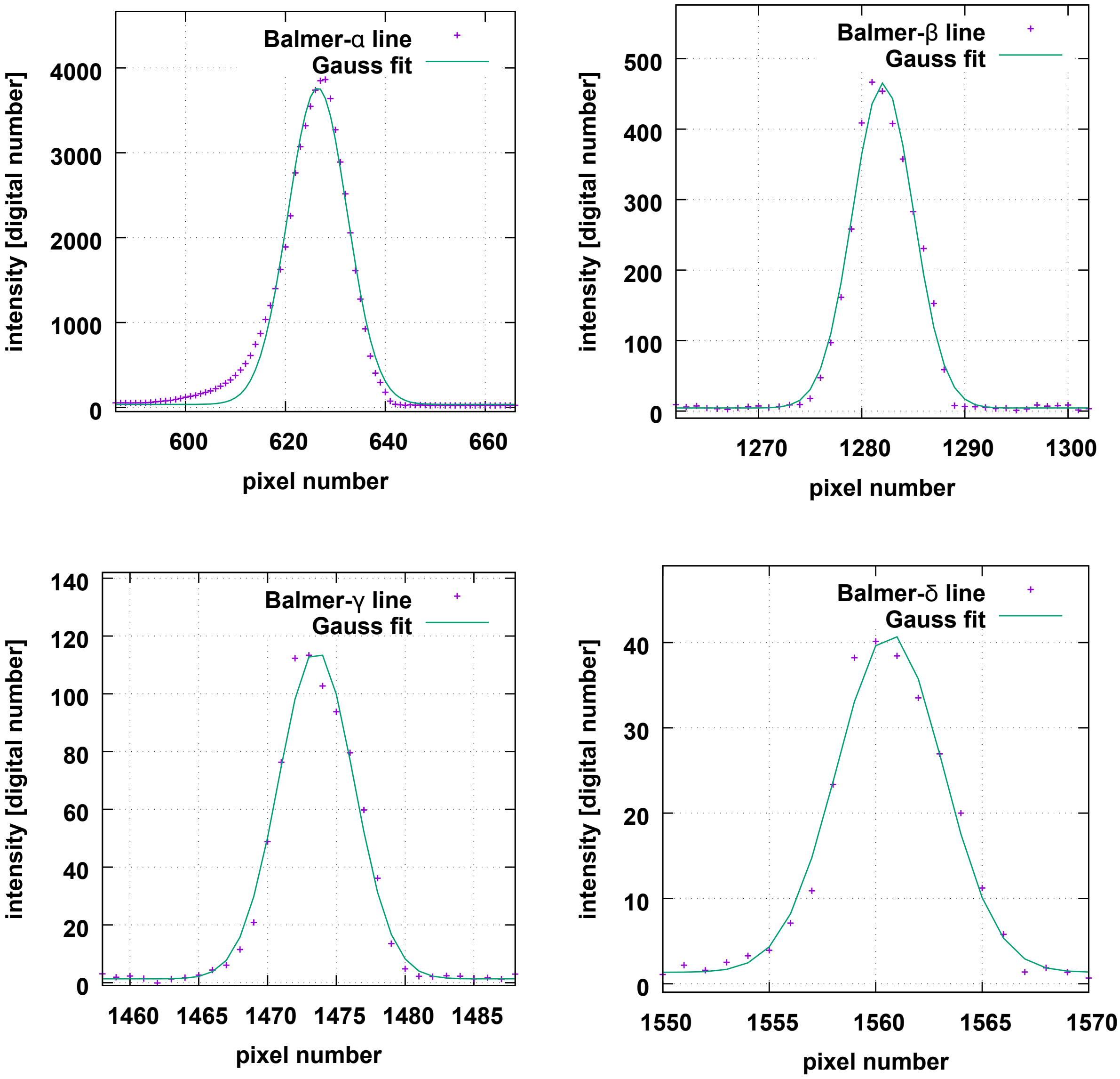

Figure 3.5: Balmer-α, β, γ & δ emission lines of raw data of spectrum collected from the recombining phase of LHD plasma discharge #142281 (without DN) with gaussian fit

on the real pixel number 1282.07 is associated to the wavelength 486.135 nm. Once all of the peaks are mapped, they can then be fitted with a polynomial function to build the wavelength calibration frame.

Figure 3.6 shows a third order polynomial reconstruction of the wavelength distribution on the pixels array of the camera of the observation system. The fit is done with a polynomial function because, as can be seen from the figure, the wavelength distribution on the pixels array of the camera is not linear. Thanks to this fitting result, it is possible to estimate the observed reciprocal linear dispersion of the system, anywhere on the pixels array. As such a reciprocal linear dispersion of 18.187 nm/mm is found near the Balmer-α line and values of 19.260 nm/mm, 19.550 nm/mm and 19.552 nm/mm are found near the Balmer-β, γ and δ lines, respectively. Theoretical estimations of the reciprocal linear dispersion in the same wavelength regions via equation 3.2 shows similar results with 17.586 nm/mm for the Balmer-α line and 19.140 nm/mm, 19.503 nm/mm and 19.654 nm/mm for the Balmer-β, γ and δ lines, respectively. The observed non-linearity is to be expected as it is in the nature of the type of grating used to have a non-linear reciprocal linear dispersion. Those that might be interested into understanding more about how gratings work can refer themselves to the website of the manufacturer of the grating (i.e. ref. [23]) or any other grating manufacturer (e.g. ref. [24]).

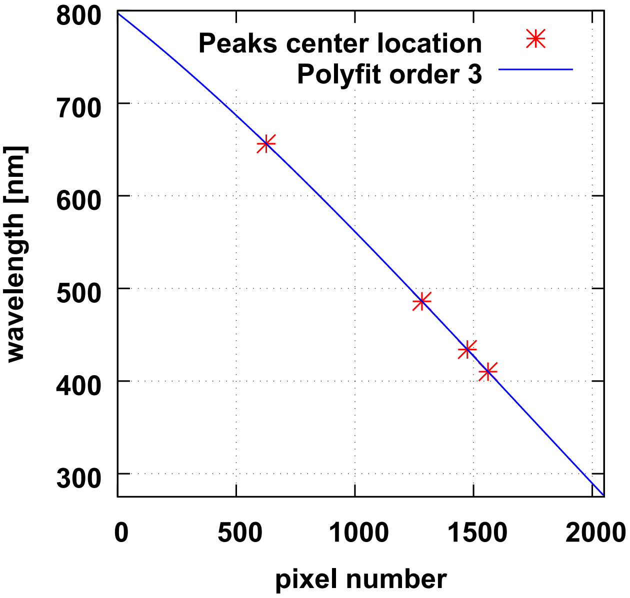

Figure 3.6: Plot of the pixel-wavelength correspondence with Balmer-α, β, γ & δ emission lines location and polynomial fit

3.1.3 Discrepancies: fine-tuning vs lineshapes asymmetry

Differences between the experimentally and theoretically obtained reciprocal linear dispersion values can be justified by more than one explanation. The first explanation involves the parameters used for the theoretical estimation. The previous calculations consider that the version of the spectrometer originally proposed by the manufacturer of the grating has not been modified. In fact, the spectrometer positioning has been slightly changed so that the spectra outputted by the camera include as many Balmer lines as possible. However, it is extremely difficult to determine exactly by how much the default configuration of the spectrometer has been modified after fine-tuning it (cf. fig. 2.9). With a pitch angle of 2.15 degrees in the outward direction from the grating normal, the gaps between the experimental the theoretical estimations are reduced to less than 1.0%. The reason why the pitch angle is considered here is because it was the one that has been modified the most during the fine-tuning phase. A difference of 1.0% is supposed low enough to consider that the other adjustment parameters (i.e. translation, yaw and roll) have a minimal impact on the results.

The second explanation is that the asymmetry observed on the emission lines corrupt the process of identification of the peaks center and cannot be neglected. The possibility that merged emission lines of deuterium and hydrogen are due to this asymmetry is highly unlikely because the quantity of deuterium present in the observed plasma is a lot more important than the quantity of hydrogen (cf. emission intensity profile in fig. 3.1). As can be seen in fig. 3.5, the lineshapes are more or less asymmetric. Granted, the data is still raw so calibrating it might fix a wavelength dispersion related problem and modifying the lineshapes on the same occasion. It is also possible that the lines are asymmetric because of the nature of components employed in the observation system. It is also possible that one or more misaligned component(s) is responsible for it. The consistent asymmetry observed on the Balmer-β, γ and δ lines is a familiar component related pattern which is sometimes observed in spectroscopy. Such asymmetry can usually be corrected with the implementation of elaborate fitting methods which require instrumental functions more complicated than a symmetric gaussian distribution. However, the asymmetry on the Balmer-α lineshape is particularly marked and radically different from the other lineshapes. The origin of this asymmetry may be due to a physical process that cannot be neglected.

3.1.4 Wavelength calibration: rays tracing approach

Values of the reciprocal linear wavelength dispersion function defined in equation 3.2 can also be used to reconstruct the wavelength axis directly from the blueprint of the spectrometer. Of course, It requires the knowledge of the design of the spectrometer and the exact path taken by the photons, from the entrance port to the CCD array of the camera fixed on the exit wall. Also, due to the important difference between the scales involved, the use of absolute dimensions is discarded to the profit of relative distances. It means that instead of giving the pixel value for such or such peak on the array of the camera, the distance between to peaks is given. with the unit of pixel value. A pixel value is defined as a real number which is proportional to the dimension of one pixel, i.e. 14 mm for the 2x2binning mode of the Neopt camera. The application of a rays tracing method using the blueprint of the spectrometer provided by the manufacturer of the grating (cf. figures 2.6 and 2.8) produces results similar to the experimental method in terms of pixels value. While the experimental method gives pixel values of 655.6, 191.5 and 87.1 between the first four peaks, the rays tracing method gives 640.8, 188.6 and

85.8. These results do not take into account the fact that the spectrometer has been fine-tuned from its default configuration. When the fine-tuning parameters mentioned in the previous subsection is used, the rays tracing method gets gives pixel values of 662.0, 192.5 and 87.2 for the discharge #142281. Identical analysis conducted on discharge #142273 gives similar results with pixel values of 660.2, 192.5 and 87.1.

In conclusion, it appears to be safe to suppose that the procedure of wavelength calibration yields accurate results. The best correspondence are obtained for the pixels gap between the Balmer-γ and Balmer-δ lines with a less than 1 pixel discrepancy between the experimental approach and the fine-tuned rays tracing method. The worst correspondence is obtained for the pixels gap between the Balmer-α and Balmer-β lines. It is possible that the previously mentioned asymmetry problem linked to Balmer-α line has something to do with this discrepancy. However, a 5-pixels discrepancy is judged acceptable for the purpose of this study.

3.2 Intensity calibration via integration sphere of known spectral radiance

In this section, an intensity calibration procedure based around the use of a calibration lamp of known spectral radiance is conducted on the data of the observation system. Eventually, a complete calibration frame for the system is produced. In addition, the geometry behind SRSM is formalized and included into the calibration frame. Ultimately, the instrumental function of the observation system is derived from the study of a calibrated spectrum.

3.2.1 Intensity calibration: formalism

The intensity calibration starts where the wavelength calibration ended. The datafile is now on a "count number by wavelength" basis. Lets recall of $\mathrm{C}(\lambda)$ and remember that C stands for the unit the data is expressed into, namely, the count number. The goal is to convert the data so that $\mathrm{C}(\lambda) \rightarrow \mathrm{L}(\lambda)$, where $\mathrm{L}(\lambda)$ is expressed with the unit of a spectral radiance [$\mathrm{W.m^{-2}.nm^{-1}.sr^{-1}}$] and is still sorted in [nm].

Through a calibration lamp, it is possible to reach $\mathrm{L}(\lambda)$ in a few easy steps. The calibration lamp is given with a frame of reference $\mathrm{R}(\lambda)$ which is expressed with the unit of a spectral radiance. When the signal of the calibration lamp is recorded, the data produced by the observation device, $\mathrm{M}(\lambda)$, is the equivalent of $\mathrm{R}(\lambda)$ but is expressed in count number instead. From here it is possible to associate the count number of $\mathrm{M}(\lambda)$ with the spectral radiance of $\mathrm{R}(\lambda)$ via the relation

$$\mathrm{X}(\lambda) = \frac{\mathrm{R}(\lambda)}{\mathrm{M}(\lambda)}, \tag{3.3}$$

where $\mathrm{X}(\lambda)$ is a calibration frame that can already be applied on any datafile $\mathrm{C}(\lambda)$, provided both $\mathrm{C}(\lambda)$ and $\mathrm{M}(\lambda)$ have the same exposure time t_{exp}.

If the exposure time of C(λ;t^C_{exp}) is not the same as the exposure time of M(λ;t^M_{exp}), it is necessary to insert a dimensionless weight coefficient T^{CM}_{exp} into the calibration relation so that it becomes

$$\mathrm{L}(\lambda) \,=\, \mathrm{C}(\lambda) \,\times\, \mathrm{X}(\lambda) \,\times\, T^{CM}_{\text{exp}} \,=\, \mathrm{C}(\lambda) \,\times\, \frac{\mathrm{R}(\lambda)}{\mathrm{M}(\lambda)} \,\times\, \frac{t^C_{\text{exp}}}{t^M_{\text{exp}}}\,. \tag{3.4}$$

It can be seen that the time variable required is called the exposure time. There are two programmable time variables by the observation system which need to be mentioned. These time variables are the acquisition time t_{acq} and the exposure time t_{exp}. The exposure time corresponds to the time length the camera collects photons and fill the buffer of its pixels. The acquisition time corresponds to the time length the camera takes to completely process one frame. This includes the exposure time as well as the time needed to process the collected data into a frame. The minimum time length needed for the camera to process the data into a frame is of 2.1 μs. However, due to some software limitation, the exposure time set for the observation system is actually programmed so that

$$t_{\text{exp}} \,=\, t_{\text{acq}} \,-\, 3\,[\mu\text{s}]\,. \tag{3.5}$$

For the sake of simplicity, the acquisition time will often be mentioned but it is implied that the exposure time should be considered instead.

3.2.2 Calibration lamp and intensity profiles

The calibration lamp used as reference is a Labsphere CSTM-US-080-SF, also referred to as an integration sphere. Figures 3.7 show the intensity profiles of the integration sphere reproduced as provided by the manufacturer (left) and the recorded intensity profiles outputted by the observation system (right) for three different acquisition times (i.e. for 1.0, 4.0 and 6.5 ms, respectively). The reference data is given in the unit of spectral radiance whereas the recorded data are still in count number. The recorded data are wavelength calibrated to match with the reference data. The dark-noise has also been removed. A comparison of the two figures indicates that the response of the observation system is highly reduced after 700 nm and almost non-existent before 400 nm. In addition, an abnormal waved pattern is present on most of the frames where the intensity reach a certain level. Also, the amplitude of the wave increases as the light collected by the system increases. It appears that this behavior comes from the camera of the spectrometer. The exact reason for this behavior is not entirely understood. Hopefully, the waves are almost completely removed when data is calibrated, saves for small artefacts located near the three irregularities present in the DN frame. That said, a calibration frame can be created from these data sets by following eq. 3.5. However, the question of which data set should be used to create the best calibration frame still needs to be addressed. The recorded data behave as expected in the sense that the longer the exposure time is, the more intense the recorded profile is. Signal saturation is noticeable on the dataset recorded with the highest exposure time between 650 and 700 nm. This should normally discard it as a possible choice for a calibration frame. Yet, the region between 300 and 500 nm turns this dataset into a pertinent option for low-light conditions. Provided the sensitivity of the camera is linear enough, it should be possible to merge two frames to build a hybrid calibration frame.

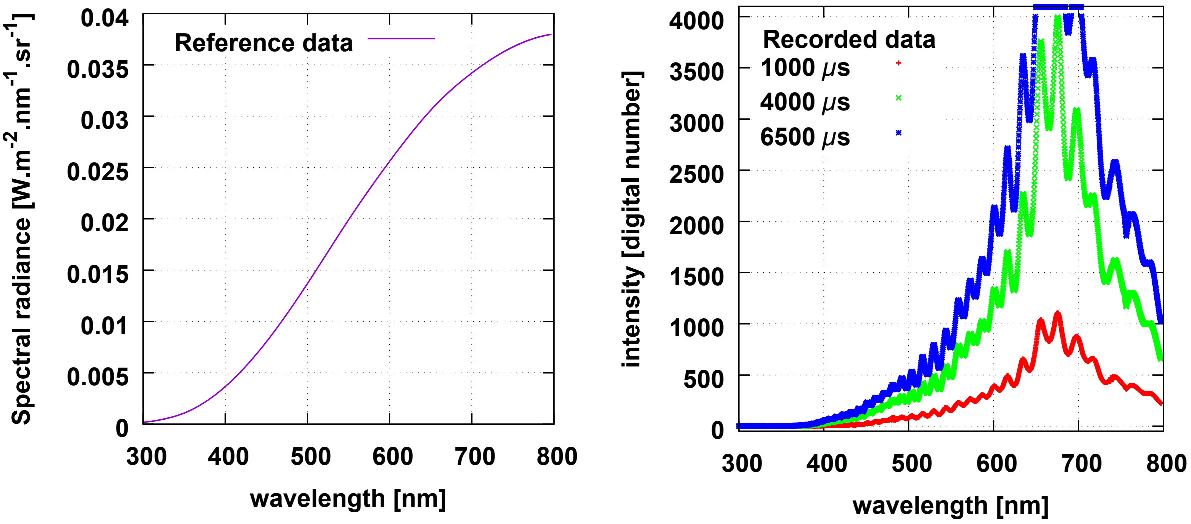

Figure 3.7: Reference data (left) and measured intensity (right) spectra of calibration lamp

3.2.3 Linearity of system response and calibration frame

Figure 3.8 shows a plot of the averaged integrated intensity values (circles) of recorded intensity profiles for ten different acquisition times going from 0.1 ms to 6.5 ms. The plot is fitted with a linear function (red continuous line) to assess the (non)-linearity of the sensitivity of the observation system. The integration calculation is done by adding the

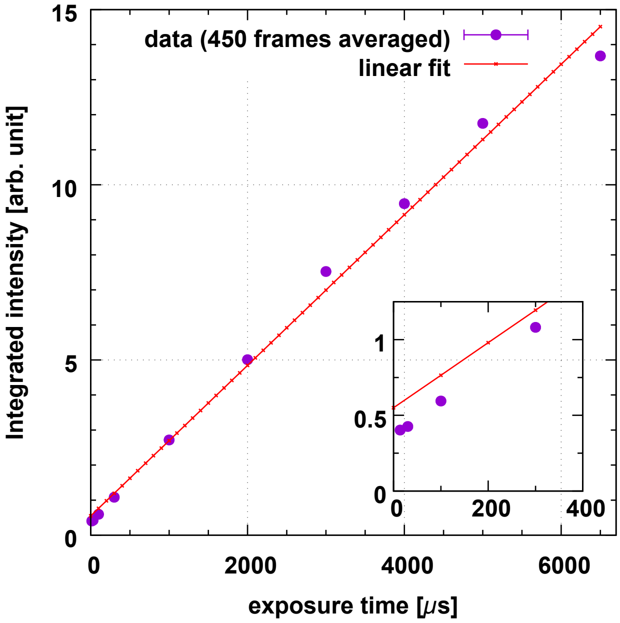

Figure 3.8: Plot of the integrated intensities of calibration frames in function of the exposure time and linear fit

count number of the pixel array except for the region which is known to saturate when the intensity is too high. Moreover, the integrated intensity values shown are obtained by taking the average of 450 frames to reduce errors that could appear due to the noise.

As can be seen from the results, the sensitivity response of the system behaves almost linearly. However, a slight increasingly sinusoidal trend is observable on the data point. This behavior can problematic especially under low light exposure where there seems to be a brief lag during which the camera under evaluates an already weak signal. In addition, the response of the system tends to saturate under intense light exposure conditions. This is not due to the saturated areas because they have been taken away from the calculations. Such behavior is not unknown to some type of cameras that tends to show such trend when the buffer of their pixels is close to get filled. A more thorough study would be necessary to explain the origin of the slight non-linearity of the system. However it is supposed that the sensitivity of the system is regular enough that, when exposed to a sufficient amount of light, it is deemed possible to merge frames with a simple linear correction coefficient.

Figures 3.9 show the calibration frames obtained from two datasets with different acquisition time (left) and the calibration frame built by merging them (right). In the left figure, calibration frames are represented by the green and blue curves for acquisition times of 4.0 and 6.5 ms, respectively. In the right figure, the hybrid calibration frame is shown between a reduced wavelength range of 400 nm and 700 nm. A narrower wavelength range is chosen for a few reasons. First, the low wavelength region is cropped because, as can be seen in the left figure, the calibration frames are not relevant under approximately 400 nm. Second, the high wavelength region is cropped because data obtained over 700 nm become irrelevant for the purpose of the study.

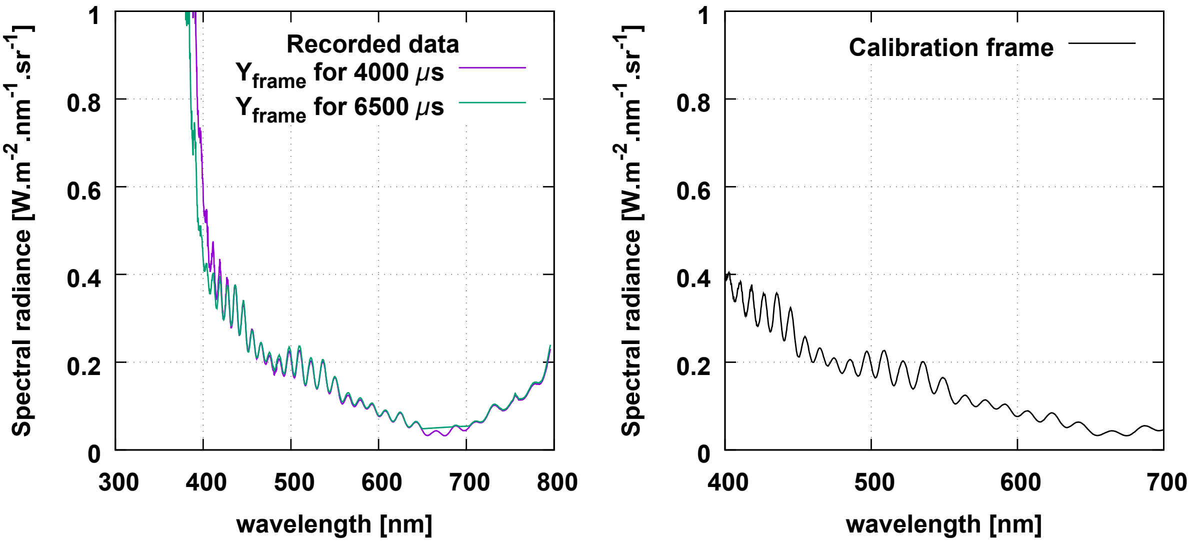

Figure 3.9: Plots of comparison between two calibration frames obtained from datasets with two different exposure times and hybrid calibration frame obtained by merging them

These calibration frames can be used to build a hybrid calibration frame that has an improved sensitivity in the lower wavelength range. To do so, a dataset with an acquisition time of 6.5 ms is used from up to approximately 450 nm, after which a linearly weighted version of a dataset taken with an acquisition time of 4.0 ms is used instead. The 4.0 ms dataset is weighted to the 6.5 ms dataset in a similar manner the T_{exp}^{CM} coefficient works. Although it has been seen that the system does not behave linearly when exposed to low and high amounts of light, it is supposed that the photons received by the pixels located on the low wavelength side of the 6.5 ms dataset is high enough to proceed as if they were behaving linearly. Such procedure is necessary to avoid erratic behavior in the low-intensity regions of the spectra, especially, in the low wavelength region. Not doing it leads to obtain unrealistic spectra that cannot be analyzed with the spectral model presented in chapter 5.

3.2.4 SRSM Geometry coefficient

For the data to be studied with a spectral model, both the data and the model obviously need to express the same physical quantity. To that end, the consideration of the geometry of the experiment is necessary. The unit required by the spectral model are of the total radiation power emitted by the slices of plasmoid which go through the FOV of the observation system, or, in simpler term, unit of spectral power [W.nm^{-1}] are needed.

To go from the unit of the spectral radiance L [W.m^{-2}.nm^{-1}.sr^{-1}] to the unit of spectral power T [W.nm^{-1}], it is necessary to understand the path the photons take from the time they are emitted by the plasmoid to the time they reach the camera of the spectrometer. The situation is mathematically a simpler than that as it is not necessary to consider the path photons take once they are inside the observation system itself. The reason being that the calibration frame used already contains this information.

Solid angle Ω

In optics, the solid angle Ω [sr] can be expressed as

$$\Omega = \frac{A}{R_{\text{obs}}}, \tag{3.6}$$

where A corresponds to the area of the lens that is passed through by photons that will eventually be projected on the optical fiber and R_{obs} corresponds to the distance the observed plasmoids supposed to be from the optics of the observation system when a measurement is conducted. The distance R_{obs} is closely related the location of the X_{cross} region detailed in chapter 2. In fact, R_{obs} is not a fixed value because plasmoids gradually move away from the observation port as they slides through the FOV. However, precision is not of necessity at this stage of the study so it seems reasonable to suppose that R_{obs} = 3.6 m. The determination of A is a more complicated to consider. Indeed, due to the nature of the measurements, not all of the photons that pass through the cylindrical lens will reach the optical fiber. As such, it is necessary to define a virtual rectangular-shaped area that corresponds to the region of the lens that is projected on the entrance of the optical fiber. Figure 3.10 illustrates where the surface $A = w \times H$ comes from. The

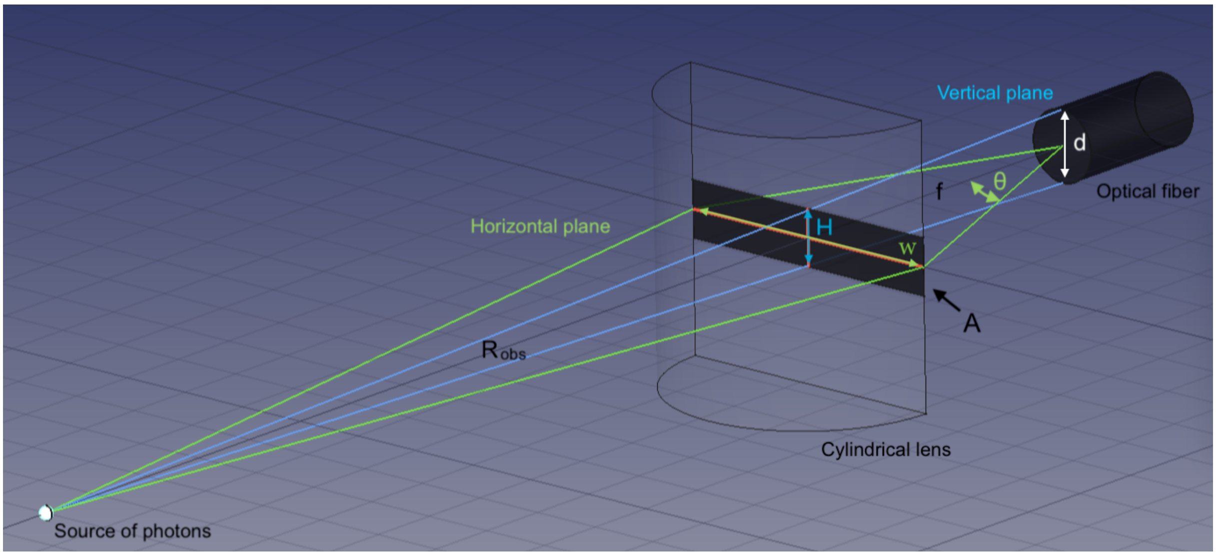

Figure 3.10: Illustration of the plasmoid observation for the solid angle calculation where the blue color and the green color are codes for the vertical and horizontal plane, respectively (figure not to scale)

meaning of the parameters used in the calculations is also presented. The width w of A is, at most, equal to the width of the acceptance cone of the optical fiber when projected on the cylindrical lens. Like so:

$$w = 2\,f\,tan(\theta)\,, \tag{3.7}$$

where θ is the aperture angle of the acceptance cone of the optical fiber. the factor f is the distance between the entrance of the optical fiber and the center of the plane side of the lens. The height H of A is defined by knowing that, by design, the cylindrical lens does not diffract the light in this direction. Consequently, only photons that will go straight into the entrance of the optical fiber are detected. Like so:

$$H = \frac{R_{\text{obs}}}{R_{\text{obs}} + f}\,d\,, \tag{3.8}$$

where d is the diameter of the optical fiber.

In fact, The real shape of the virtual area A is probably not of rectangular shape, but it has been deemed as a good approximation considering the order of magnitude of the dimensions involved. The way the height value is defined here does not take into account that the entrance of the optical fiber is more like a disk. In addition, if photons emitted from the source hit A with a vertical inclination that is too steep, they will not be refracted on the entrance of the optical fiber.

Power density W and spectral power T

The spectral radiance L can be expressed in function of the power density W [W.m^{-2}.nm^{-1}] such that

$$L = \frac{W}{\Omega}\,, \tag{3.9}$$

where W is the power density emanated from the slice of plasmoid and Ω is the solid angle defined by eq. 3.6.

The power density is Figure 3.11 illustrates the scale difference that exists between the observation area of the optics and the area that actually emits light. The observation area defined here consists simply in prolongating the acceptance cone of the optical fiber. The contribution of the lens is completely removed from the calculations. Also, R_{obs} is fixed for the same reason given for the calculation of the solid angle.

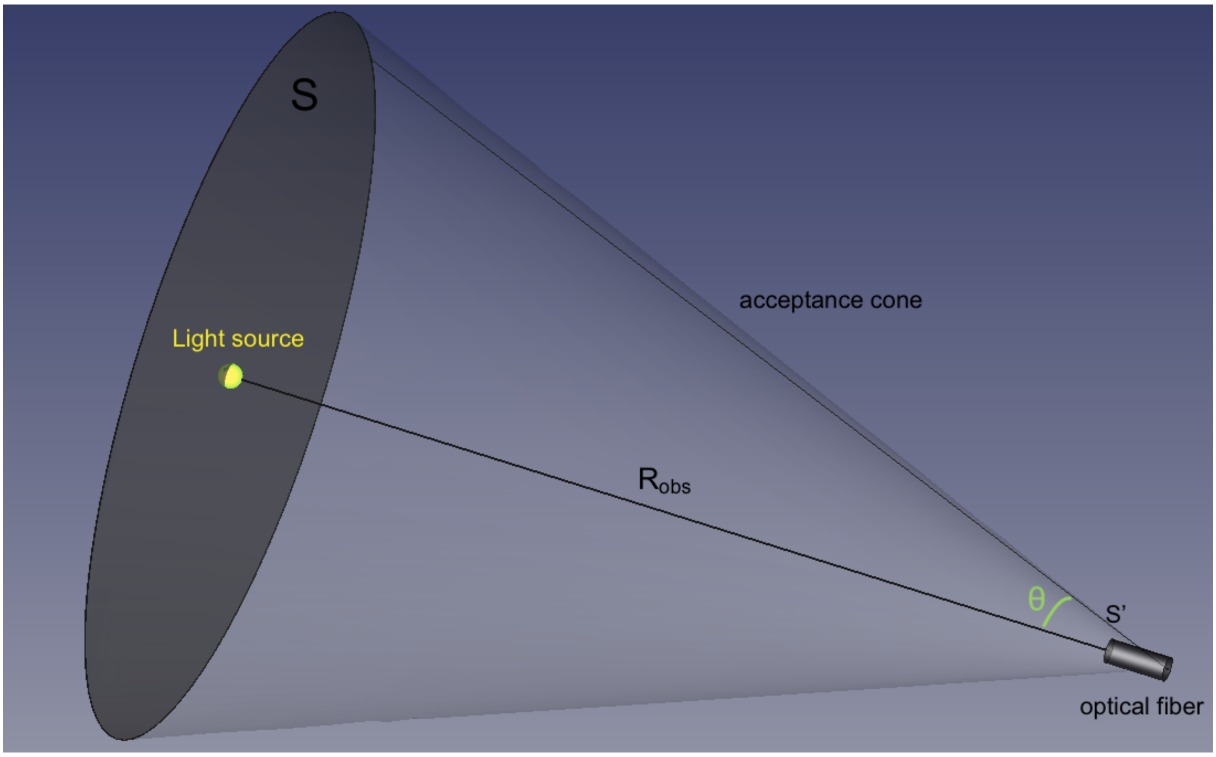

Figure 3.11: Illustration of the plasmoid observation for the spectral power calculation where the acceptance cone of the optics fiber is extended until the vertical plane the plasmoids are supposed to be found (figure not to scale)

Because the light source is supposed to radiate homogeneously in all directions, the spectral power T can be defined with an inverse-square law. By considering the surfaces the photons may be emitted from emitted and the surface it is received at, let T be

$$T = \frac{W \times S'}{R_{\text{obs}}^2} \times S\,, \tag{3.10}$$

where S' is the surface of the front end of the optical fiber, i.e. the area towards which all of the photons emitted by the slice of plasmoid is collected. The factor S corresponds to the maximal area covered by the acceptance cone of the optical fiber. The fractional term corresponds to the power density sent from the location the light source is and collected by the surface of the front end of the optical fiber. The optical fiber acceptance cone project a vertical plane at R_{obs}, where the photons emitted by the slice of plasmoid are supposed to come from.

With $S = \pi R_{\text{obs}}^2 tan^2(\theta)$, the spectral power becomes

$$T = W \times S' \times \pi tan^2(\theta) . \tag{3.11}$$

SRSM coefficient K

Equations 3.11 and 3.9 can be combined so that the spectral power is expressed into the form

$$T = L \Omega S' \times \pi tan^2(\theta) = L K , \tag{3.12}$$

where K is the SRSM coefficient.

3.3 Estimation of Instrumental broadening from calibrated experimental data

Now that it is possible to calibrate experimental data, it is necessary to estimate the so-called instrumental function of the observation system. When plasmas are observed with spectrometers, the produced spectra will always be corrupted by the observation system that made them. For example, a naturally broadened or a negligibly broadened emission line may appears broader than what it really is because of the instrument used for the measurement. Reasons behind the existence of this broadening phenomenon will not be treated here, but it still needs to be quantified and included into the spectral model.

To quantify the instrumental function of an experimental setup, a spectrum that contains at least one emission line with a physically induced broadening that is weaker than the one induced by the observation system. Such procedure is usually conducted via the use of lasers. However, it is also possible to proceed with certain types of plasma if the setup used for the measurement have a relatively low resolution power. As such, the observation system used for this experiment is of low resolution power, and the calibrated spectra of recombining plasma processed in this chapter happen to be, supposedly, negligibly broadened by physical phenomena.

Figure 3.12 shows a calibrated spectrum of a recombining phase collected during the LHD plasma discharge #142281. This spectrum is the calibrated version of the raw data shown fig. 3.2 (without DN). Figures 3.13 show the isolated and calibrated experimental spectra of the Balmer-α, β, γ and δ emission lines. These spectra are the calibrated versions of the raw data shown fig. 3.5. The Full-Width-at-Half-Maximum (FWHM) of the Balmer-α emission line is approximately 4.0 nm. The FWHM of the Balmer-β, γ and δ emission lines are all closer to 2.0 nm, with a decreasing trend clearly noticeable. Such behavior is expected as the instrumental broadening is wavelength dependent.

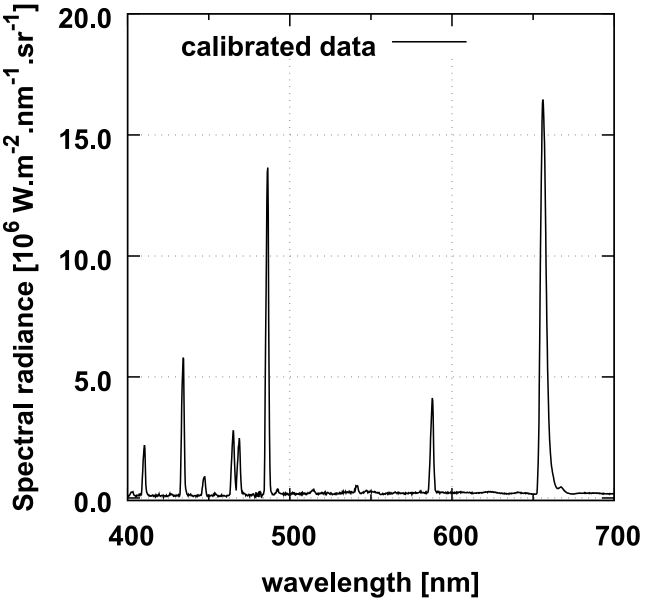

Figure 3.12: Calibrated spectrum collected from the recombining phase of LHD plasma discharge #142281

It is still not evident whether the broadening of the Balmer-α emission line is entirely due to the instrumental function of the observation system. In fact, it would be safe to suppose that a physically induced broadening phenomenon does have influence on the width of this emission line. Another detail which incriminates the Balmer-α emission line is that its asymmetry is unique to the observed emission lines. The previously emitted suspicion that the other emission lines are asymmetric because of the measurement seems to be confirmed as the calibration did not mitigate it in any way.

Because of how close the FWHMs of the successive emission lines are, it has been judged unnecessary to build an instrumental function, and to consider a fixed instrumental broadening coefficient of $w^{1/2}_{\text{inst.}} = 1.0$ nm instead.

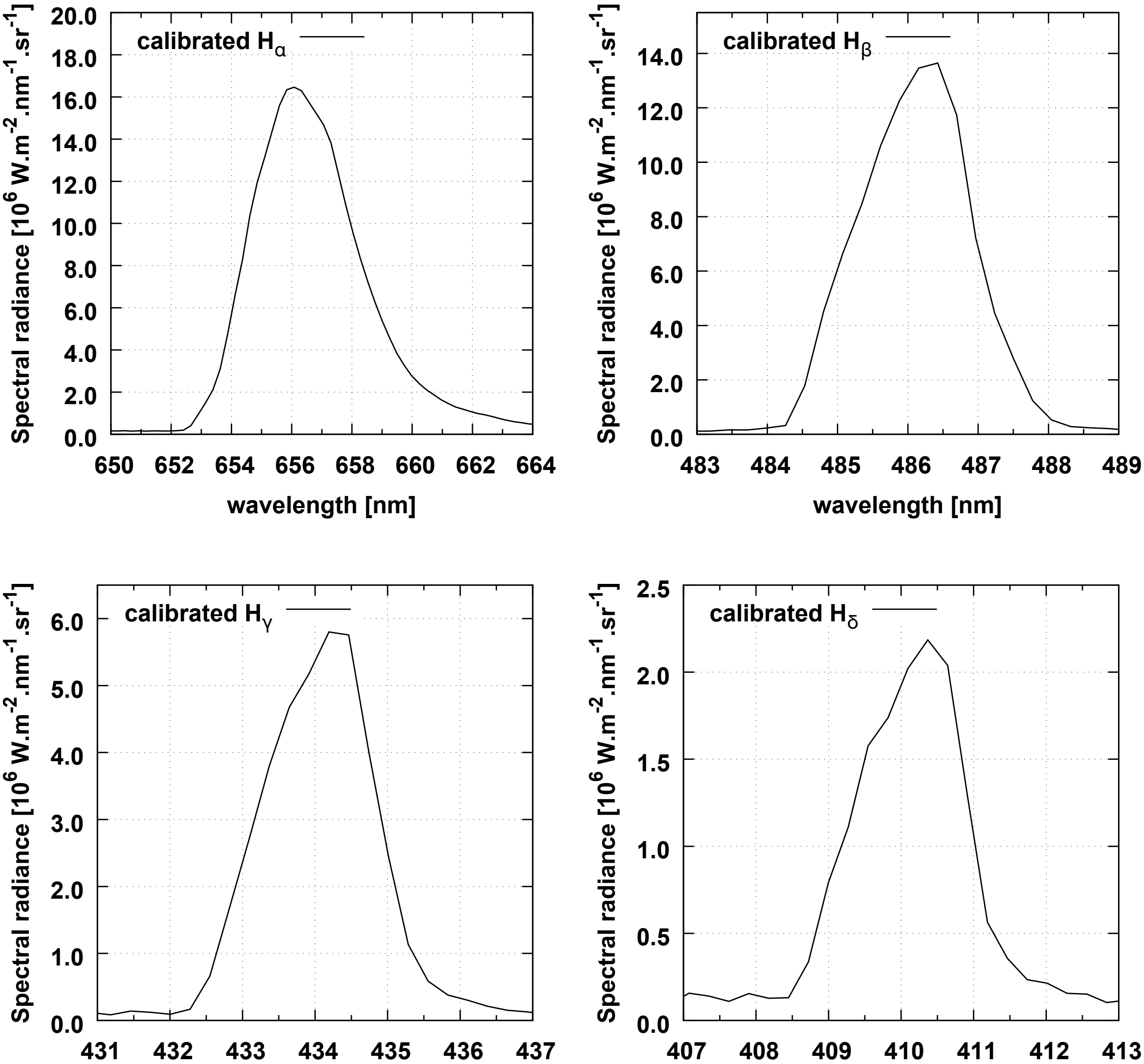

Figure 3.13: Calibrated Balmer-α, β, γ & δ lines of LHD plasma discharge #142281 in recombining phase

Chapter 4

Confirmation of Spatially-Resolved Spectral Measurements

It is necessary to verify that the data collected by the observation system are appropriate before going further with the analysis. At least two criteria need to be considered:

- Firstly, the collected spectra have to be of slices of plasmoid.
- Secondly, the observed plasmoid must not change while data is collected.

When both conditions are met, only then it is possible to proceed to the next phase, spatially-resolved spectral measurements (cf. chapter 5). To know if slices of plasmoid are correctly observed, the profile of the integrated intensity of the spectra is compared to (or with) the profile of the integrated intensity images of the fast camera. If both profiles match, it means that the spectrometer is correctly synchronized to the fast camera. Only then, it is possible to verify if the spectra correspond to slices of plasmoid. The behavior of a plasmoid depends greatly on the background plasma it is in. This is why it is necessary to known the configuration of the background plasma in the vacuum vessel and especially near the X_{cross} region. Parameters that have to be looked after are the heating pattern used to produce the background plasma, magnetic field lines orientation where the observed plasmoid supposedly goes through and the profile of the electron temperature of the background plasma in the vicinity of the plasmoid. A case of study which involve a plasma discharge conducted during the 2017 experimental campaign in LHD is analyzed. Results extracted from the analysis indicate that one instance of pellet injection can be used for spatially-resolved spectral measurements purposes. Other discharges from the same campaign are also analyzed to assess the reliability of the observation system. It appears that it is possible to use the system on a regular basis, but severe constraints do apply.

The fourth chapter is divided into three sections. The first section explains in details the different steps required to assess if spatially-resolved spectral measurements can be conducted. The second section introduces a case of study where an interesting pellet injection is observed. The third section adds more case of study to check the consistency of the observation system.

4.1 A method for the verification of the observation system SRSM capability

In this section, criteria of selection to identify SRSM-conform datasets are given. Firstly, the procedure used to verify the configuration of the background plasma is explained. Secondly, the procedure used to compare the integrated intensity profiles of the spectrometer and the fast camera is explained.

4.1.1 Consideration of background plasma for stability of plasmoid

It has been reported that the configuration of the background plasma can have a great influence on how plasmoids behave. For example, knowledge is that a higher electron temperature contributes to an increase of the consumption rate of plasmoids. Another example that can be given is the high susceptibility of plasmoids to asymmetrical neutral beam injection (NBI) heating pattern that can modify their trajectory drastically (cf. chapter 1). This is why it is important to think thoroughly about how the SRSM experiment needs to be conducted and to choose wisely the plasma discharge to study.

Plasma heating pattern and X_{cross}

As defined in chapter 2, X_{cross} corresponds to the region in the vacuum vessel where the observation of plasmoids is supposed to happen. X_{cross} is located at the core plasma region, when the magnetic field configuration of the LHD is set at $R_{\text{ax}} = 3.6$ m. There are many reasons as to why such location is picked over another. For example, the orientation of the plasmoids while being observed is realistically ideal only in X_{cross}. Due to the design of the fuel pellet injection experiments and the distribution of the magnetic field lines in LHD (for R_{ax} set at 3.6 m), the lines that are optimally perpendicular to the observation port are actually found on the inner side of the background plasma. The problem is that the pellets rarely go that far into the plasma. The second best choice is near the plasma core region, hence X_{cross}. Another pertinent reason to choose this location is because the magnetic field lines are almost parallel between each others in this region.

Stability of electron temperature

The electron temperature of the background plasma (T_{e}^{bg}) is a parameter that can vary a lot during a discharge. It often has a piked radial profile which is symmetrically distributed around the core plasma. It is crucial to avoid such behavior when observing plasmoids because it is susceptible to corrupt the measurements. As already explained, plasmoids are sensitive to changes of temperatures. When a variation of electron temperature becomes significant, Hopefully, the profile of T_{e}^{bg} is usually symmetric respectively to the magnetic axis, and is often flat-shaped near the core plasma region. However, spatial measurement cannot be achieved in discharges where the profile of T_{e}^{bg} is extremely narrow (i.e. no flat top) and for cases when the velocity of the plasmoid so slow that the background plasma configuration have the time to change drastically.

Provided the length of the studied plasmoid is known, T_{e}^{bg} can be estimated near the locations the slices of plasmoid are obtained from Thomson scattering measurements. By obtaining T_{e}^{bg} half the plasmoid length before and half the plasmoid length after R_{ax}, it should possible to assess how different the background plasma configuration is between the first and last observed slices of plasmoid. In reality, the angle of injection of the pellets and the angle of observation of the Thomson scattering diagnostics are not the same. It means that the values of T_{e}^{bg} where the actual observations are made is not exactly equal to the ones obtained from the TS database. Considering the distances involved, 6° can be considered as a small angle of deviation relatively to the dimension of the plasmoids (cf. chapter 2) They are however supposed to be close enough for the purpose of the study. The T_{e}^{bg} that are of interest are then, T_{e}^{bg35} (i.e. 10 centimeters before R_{obs}), T_{e}^{bg36} (i.e. at R_{obs}) and T_{e}^{bg37} (i.e. 10 centimeters after R_{obs}).

Overall, the confirmation that a balanced NBI heating pattern is used and that the electron temperature profile stays stable at X_{cross} are considered to be enough to find out whether SRSM can be conducted on the basis of the second criterion given at the beginning of the chapter.

4.1.2 Consideration of imaging data for profiles comparison

The observation system is equipped with two observation devices. The main device outputs spectroscopic data that are produced by collecting photons emitted from a certain region of the background plasma and sending them to a visible spectrometer. The mode of operation of this observation system is detailed more explicitly in chapter 2. The other device outputs imaging data that are produced by collecting photons emitted from the same region of the background plasma and sending them to a Phantom V7 fast camera. This operation system is based on the same camera used in the second experiment that is introduced in chapter 1. However, unlike the second experiment, the fiberscopes that feed the fast camera are not equipped with filters. Consequently, the images produced by the device are, similarly to the main device, observed in the visible range.

Observation of plasmoids with fast camera

The advantage of the imaging diagnostics over the spectroscopic one is that it outputs data in a format which is easy to understand for the eyes. This is actually why such device is used in this experiment. Because both devices look into the same direction, it is supposed that what is output by both correspond to the same event. Like so, it is possible to identify events that are likely to be of interest. Before going further, it is first necessary to verify whether the devices are really observing the same events. Doing so can be done by comparing the integrated intensity profiles of both devices. An integrated intensity profile consists of plots that represent the summation of the intensity values of some or all of the pixels of a frame (resp. spectrum) for some or all of the frames (resp. spectrum) collected during a plasma discharge. The summed intensity values of the data are then considered on a frame by frame basis to create a profile.

However, a direct comparison between the frames of the fast camera and the frames of the spectrometer is not possible because these devices do not possess the same field-of-view (FOV). Indeed, the fiberscopes that feed the fast camera with images has a wide FOV, whereas the FOV of the optics that feed the spectrometer is, supposedly, a narrow-band shaped FOV (cf. chapter 2). The data produced by the fast-camera need to be processed with a virtual FOV, identical to the effective FOV of the main observation device.

Virtual band-shaped FOV

A virtual band-shaped FOV can be created relatively easily. The raw data of the fast camera is given under the form of a giant matrix of 768 by 176 pixels. On this matrix, four images of 136 by 136 pixels each are projected in a line. The four fiberscopes at the origin of these images observe the same scene but from slightly different locations and very different angles (cf. chapter 2). In practice, only one image is to be processed. The image chosen corresponds to the fiberscope which is positioned directly on the bottom of the optics of the main observation device. By design, the up-bottom orientation of the fiberscope is aligned with the orientation of the narrow band-shaped FOV.

The way the virtual band-shaped FOV is created consists of discarding pixels from the isolated image of 136 by 136 pixels. Due to the theoretically favorable orientation of the fiberscope, the pixels to be kept from the summation should be located on a vertical rectangle. The width of the rectangle should correspond to the width of the effective FOV. The width of the effective FOV is known to be about 14 mm (cf. chapter 2). The resolution of the fast camera at R_{obs}, the expected distance between the observation port and the observed events, can be estimated from the reference [14]. It has been estimated that a band of 2 pixels wide located at the center of the isolated image is a good starting point for the virtual FOV. Corrections could be applied at a later depending on the results.

Profiles harmonization, synchronization and comparison

Because both devices have different range of operation, sensitivity to light and number of pixels, the magnitude of the integrated intensity profiles are also different. It implies that the integrated intensity profiles cannot be compared as is. This divergence is solved by normalizing both profiles. In addition, although both observation devices receive the same trigger from the LHD, the time are which they start acquiring data is different. In consequence, a delay is present when overlaying both integrated intensity profiles. This divergence is solved by shifting one of the profile until its barycenter coincide with the barycenter of the other profile. The time factor with which a profile needs to shifted with is derived from a fitting method that runs until the temporal barycenters of both profile is identical. The temporal barycenter t^o of a profile is equal to

$$t^o = \sum_t x(t) \times \frac{y(t)}{\sum_t (y(t))} \,, \tag{4.1}$$

where $x(t)$ and $y(t)$ are equal to the time stamp and the integrated intensity of a frame t, respectively.

After the normalization and synchronization procedures are finished, comparison of the obtained synchronized normalized and integrated intensity profiles can be conducted. At this point, the only information that is compared is the shape of the profiles. Nonetheless, provided the corrections obtained via fitting can be physically explained, the study of these shapes is enough to find out whether SRSM can be conducted on the basis of the first criterion given at the beginning of the chapter.

4.2 Case of study: LHD plasma discharge #135454

Figure 4.1 shows images of the sixth plasmoid recorded with the fast-camera at four different timings. The fast camera is set to output one frame every 20 μs with a 1 μs exposure time per frame. Although the direction of elongation of the plasmoid is slightly inclined from the horizontal axis of the observation system, its trajectory appears to be pretty straight. The shape of the plasmoid does not change significantly during the observation, except for the very first frames. It is however not a problem as the FOV of the system is located near the center of the frame. This plasmoid seems to be appropriate for conducting a spatial-resolution measurement. However, it is first necessary to confirm that the criteria given at the beginning of this chapter are fulfilled.

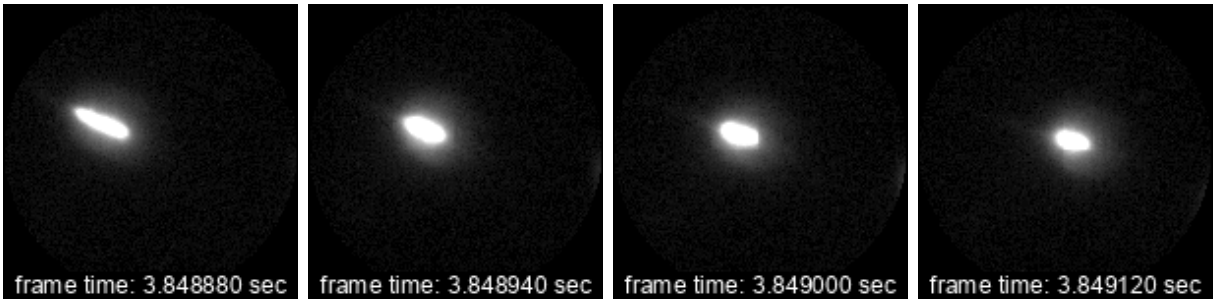

Figure 4.1: Fast camera images of a plasmoid obtained for discharge #135454 at four different timings [Raw data of fast camera generously provided by G. Motojima]

4.2.1 Background plasma

Figure 4.2 shows the electron temperature of the background plasma measured around X_{cross} just before and after the sixth pellet is injected in the LHD. Data for T_{e}^{bg} have been obtained from the Thomson Scattering (TS) measurements database of the LHD. The profiles of T_{e}^{bg35} (green), T_{e}^{bg36} (red) and T_{e}^{bg37} (purple) are drawn. The temporal evolution of the Balmer-α line of hydrogen obtained from a spectroscopic diagnostics different from the one introduced in this work is also drawn (black). From this kind of figure, it is possible to assess whether it is correct to suppose that the recorded slices of plasmoid have similar deposition rates, meaning that they can be interpreted as a slice of the same plasmoid. So If the change of temperature between T_{e}^{35}, T_{e}^{37} and T_{e}^{37} is too large, it may not be possible to interpret the slices of plasmoid entering and leaving X_{cross} as being emitted from the same plasmoid because the configurations of the background plasma between these two locations are too different. Knowing how an unperturbed plasmoid moves into the background plasma of LHD (cf. chapter 1), it is possible to estimate

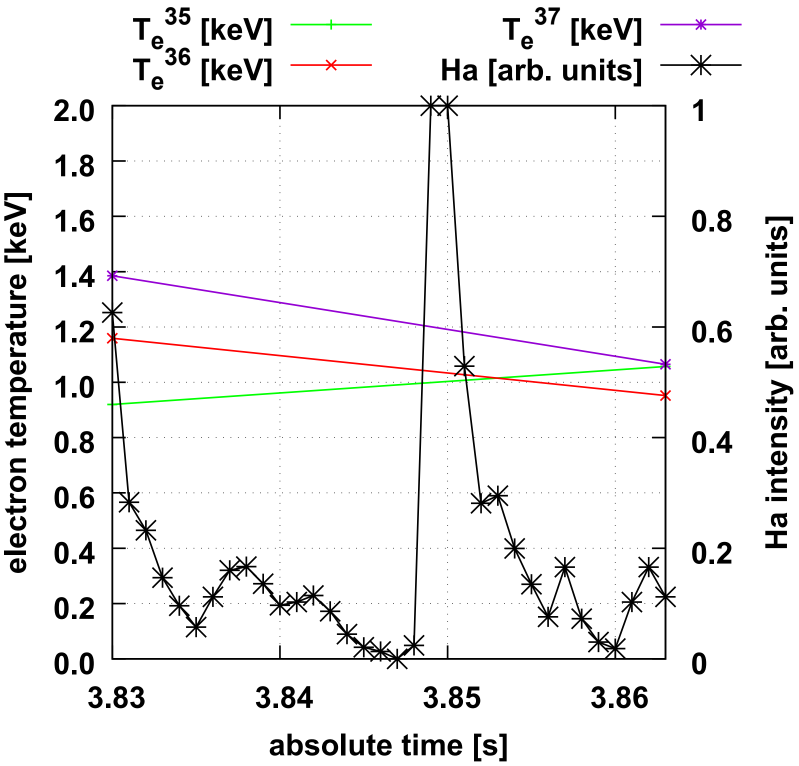

Figure 4.2: Electron temperature just before (T_e^{bg35}) at (T_e^{bg36}) and just after (T_e^{bg37}) X_{cross} and recording of the Balmer-α line emitted from the sixth plasmoid for the discharge #135454 in function of absolute time

when and where the slices of plasmoid will be recorded. Globally, T_e^{bg} is approximately kept around 1.0 ± 0.4 keV. Measurement of the plasmoid with the observation system is actually done just before the 3.85 s timestamp (cf. imaging data). Near that time, T_e^{35} and T_e^{36} are both pretty close to 1.0 keV, while T_e^{37} is just under 1.2 keV. The exact effects of a 0.2 keV difference on the ablation clouds is not known, but if the magnitude of temperature involved in plasmoids in considered (i.e. 1/1000 of keV), it is probably safe to suppose that the deposition profile of the plasmoid is not changed much by the gradient of T_e^{bg}.

4.2.2 Virtual band-shaped FOV

Figure 4.3 indicates the location of the virtual FOV with the two vertical white bands.

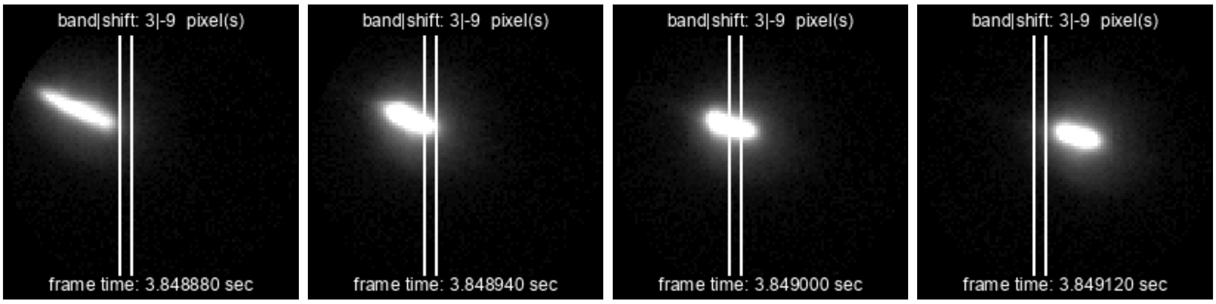

Figure 4.3: Fast camera images shown in fig. 4.1 with overlay of translated virtual FOV

The virtual band has been shifted a few pixels to the left to take into account a slight misalignment between the optics of the spectroscopic system and the imaging system. Specifics about the method used to calculate the shift is presented in the next subsection.

Figure 4.4 also shows the comparison between the normalized integrated intensity profile of the imaging data without the virtual band (purple line) and with the virtual band (green line). As expected, the integrated intensity profile that results from this procedure has a reduced time-length. The fact that the obtained peak does not end on the right edge of the unprocessed profile indicates that the observed plasmoid was not at the end of its life. The observation of plasmoid during the end of its life is not advised as it would be against the requirement that an ablation cloud must stay in a maximally expanded, pseudo-stable state while it is being observed (cf. chapter 1).

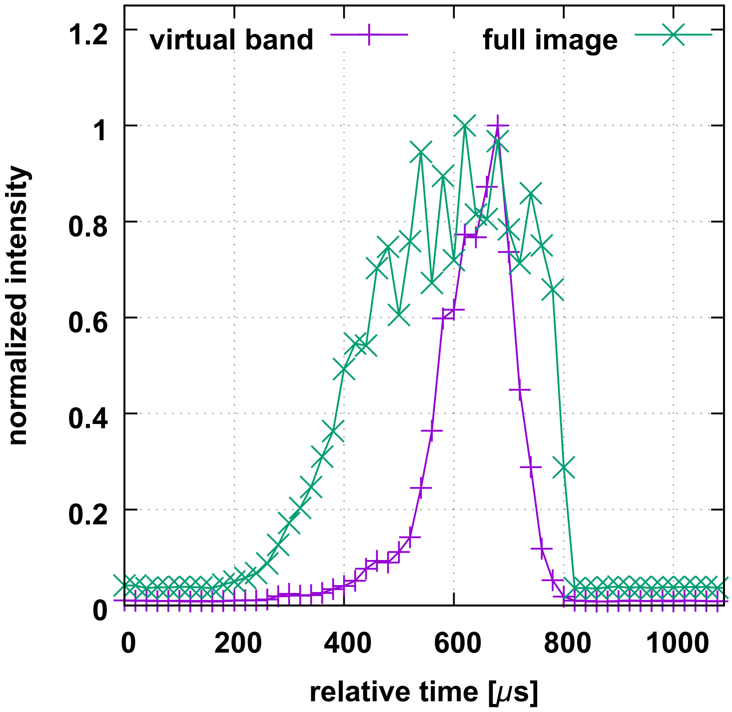

Figure 4.4: Comparison of imaging data integrated intensity profiles with (blue) or without (green) virtual FOV

4.2.3 Comparison between spectroscopic and imaging diagnostics

Figure 4.5 shows the comparison between the normalized and synchronized integrated intensity profiles of the spectroscopic data and the processed imaging data. The spectrometer is set to output one frame every 14 μs with a 11 μs exposure time per frame. Only the wavelength region near the Balmer-β line is considered. Mainly because the Balmer-α line saturates for most of the observation. By normalized, it is meant that the amplitude of the profiles have been normalized to one, same as the imaging data. This is

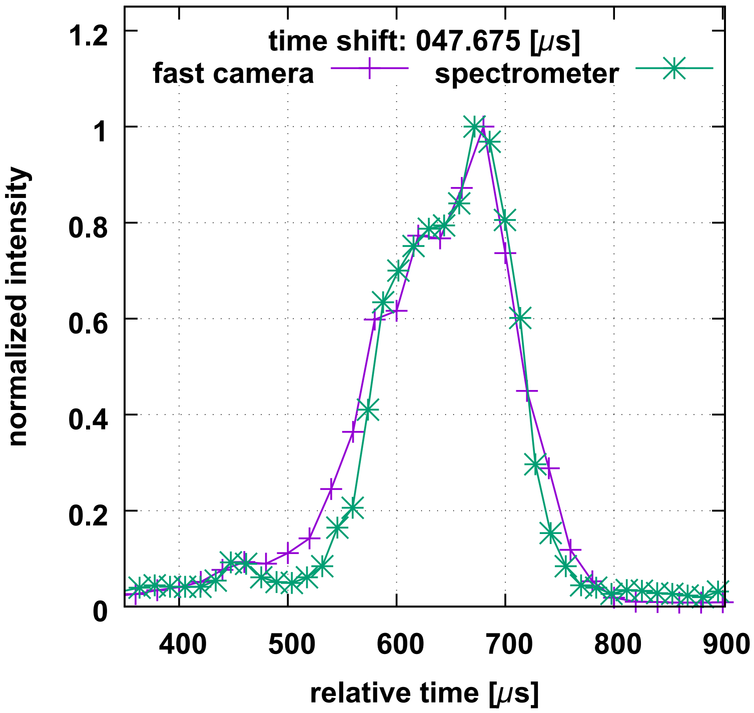

Figure 4.5: Comparison of normalized and synchronized integrated intensity profiles between imaging data (blue) and spectroscopic data (green) for #135454

done because the sensitivity and timings of both devices are different. By synchronized, it is meant that the profile of the spectroscopic data has been time shifted to have both profiles coincide with each other. The time shift is done via the temporal barycenter fitting method given in the previous section.

Comparison of the normalized and synchronized integrated intensity profiles of the spectrometer and fast-camera shows a good agreement. However, the profile derived from the imaging data is slightly wider than the profile of derived from the spectroscopic data. This difference cannot be corrected by modifying the width of the virtual FOV. The two pixels width that has been guessed from previous experiments where the fast camera was employed seems to be correct. The trajectory of the plasmoid appears to be slightly tilted in the imaging data. An angle of about 16° is measured between the trajectory of the plasmoid and the horizontal axis of the fiberscope. Considering how the fiberscopes and the observation system of the spectrometer are fixed on the support flange (cf. chapter 2), it is possible that, due to some inaccuracies during the preparation of the setup, the optics of the main observation device is not perfectly aligned with the fiberscope. If the rotation misalignment is such that the angle of penetration of the plasmoid with the effective FOV is different than the one with the virtual FOV, it could explain why the width difference of the profiles. A reasonable explanation for this phenomenon is that when the plasmoid penetrates a band-shaped FOV, the shape of the first slices of plasmoid that will be detected depends on the angle at which the plasmoid has reached the FOV. If the angle of penetration is normal to the FOV, the first observed slice of plasmoid will be a lot brighter than if the plasmoid had crossed the FOV with an angle. It seems that the spectroscopic data is are more like the former situation, whereas the imaging data are more like the latter situation.

Overall, results suggest that the observation system does indeed collected spectra that correspond to slices of plasmoid. With the results found in the previous subsection are taken into account, SRSM is confirmed, at least for the sixth pellet of the LHD plasma discharge #135454.

4.3 Benchmarks for results consistency

In this section, the consistency of the observation system with the test of more plasma discharges chosen to be as close as possible to the one done in the previous section. A case which highlights the presence of a rotational misalignment is also shown.

4.3.1 More cases of study: discharges #135455 and #135456

Figure 4.6 shows profiles comparison for the LHD plasma discharges #135455 and #135456. Both profiles also correspond to the sixth and last injected pellets of their discharge. A significant difference between the three discharges is the NBI heating patterns used. This partly explains why the profile-shapes are different.

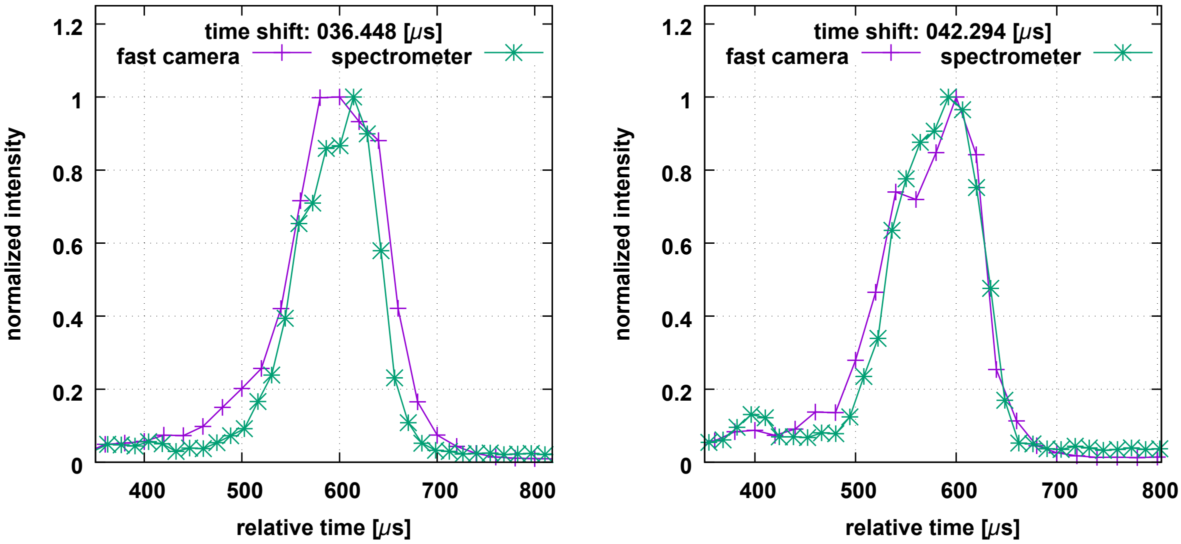

Figure 4.6: Comparison of normalized and synchronized integrated intensity profiles between imaging data (blue) and spectroscopic data (green) for discharge #135455 (left) and #135456 (right)

The time shifts derived from these analyses shows that virtual FOV is relatively accurate. The values obtained are not unrealistic. A time-length ranging between 36 and 48

μs corresponds to 2 to 3 frames of the fast camera or 2 to 4 frames of the spectrometer. The time-span the adjusted value shift between is even shorter than the time it takes the spectrometer to take one frame.

As can be seen in figure 4.7, background plasma configurations near X_{cross} for discharges #135455 and #135456 are similar to the configuration obtained for discharge #135454. The plasmoids are observed from almost the same time as discharge #135454.

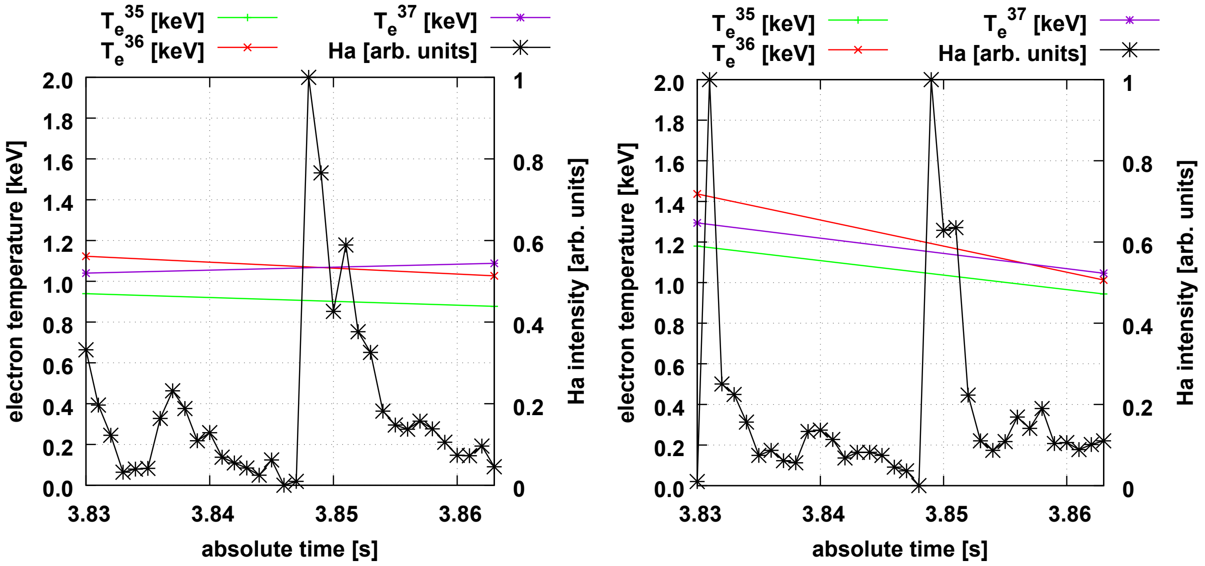

Figure 4.7: Electron temperature just before (T_{e}^{35}) at (T_{e}^{36}) and just after (T_{e}^{37}) X_{cross} and recording of the Balmer-α line emitted from the sixth plasmoid for the discharges #135455 (left) and #135456 (right) in function of absolute time

TS data shows that the profile of T_{e}^{bg} is even more stable than the one found in the discharge #135454. Even with a non-favorable NBI heating pattern, these two discharges present a lot of good points for them to be used in a SRSM. However, what makes them less appealing than that of the discharge #135454 is that their spatial resolution is not as high. With only about 10 datapoints against the 20 datapoints of #135454, the spectra obtained from #135455 and #135456 would not bring as much details about the inner structure of the ablation clouds.

Even so, results indicates that the developed method is able to efficiently verify whether a dataset can be used for SRSM or not. Results also show that it is possible to conduct SRSM on a regular basis, provided the spectral model used is good enough.

4.3.2 Plasmoid drift observation hints at rotational misalignment

Plasmoid drifts are bulk of matter that are ejected from plasmoids in regular intervals. These objects are a lot faster and produce significantly less light than the plasmoids.

Figure 4.8 shows that in addition to plasmoids, it is also possible to detect those plasmoid drifts (red arrows). The figure shows the same observation as the case of study #135454, but the contrast of the images have been increased compared to the previous ones in order to highlight the presence of the plasmoid drift. Plasmoid drifts are not easy to study with this observation system because the timings at which they are emitted is not clearly identifiable and their spectra are not evident to analyze. Their brightness is so very weak that the signal/noise ratio is not good enough for the continuum radiation of their spectra to be clearly defined. Thanks to the images provided by the fast camera, it is possible to identify a plasmoid drift from a plasmoid and process the data accordingly (i.e. discard the data associated to the plasmoid drift).

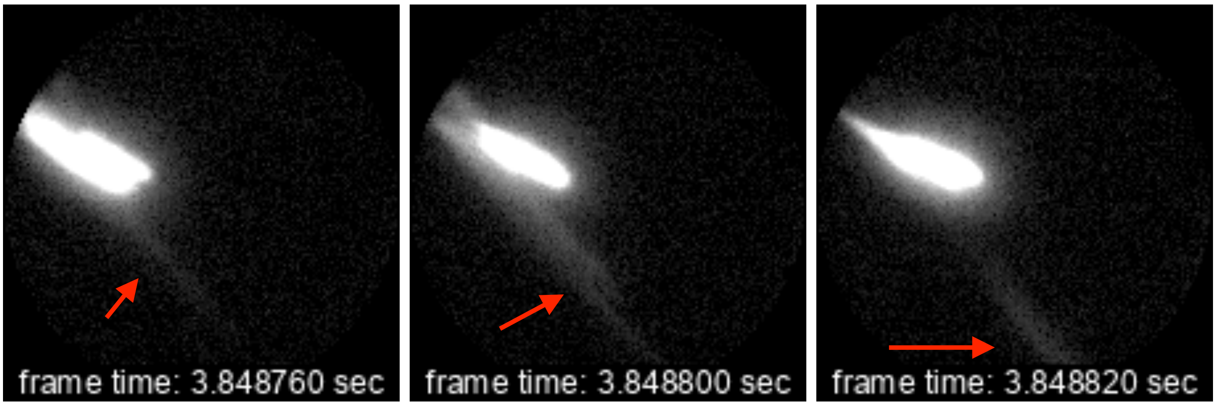

Figure 4.8: Plasmoid drift observation from imaging data of the sixth plasmoid for the discharge #135454 at three different timings

The observation of plasmoid drifts can also be used to underline a consequence of the rotational misalignment that has been briefly mentioned before. Figure 4.9 illustrates the difference between the virtual FOV used, i.e. a translational drift (red), and a proposed rotational virtual FOV (green). Analysis of the profiles, demonstrate that, because it is just translated, the virtual FOV suggests that the front region of the plasmoid and the

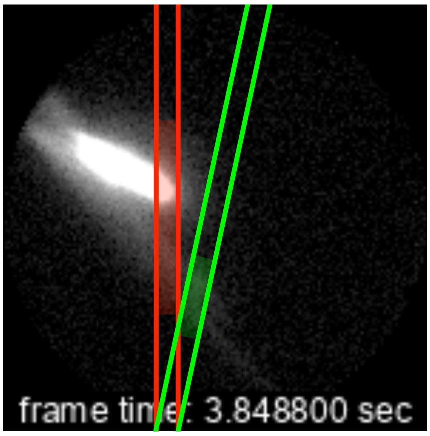

Figure 4.9: Plasmoid drift observation: rotation (green) vs translation (red) misalignment

back end of the plasmoid drift are both detected simultaneously for a brief moment. This is however not the case when observing the intensity profile obtained by the spectrometer. For the sake of exactitude, it is advocated to modify the way the virtual FOV is modeled to a rotation. However, the precision obtained with the current results is enough for its purpose so it has not been done.

Chapter 5

Characterization of fuel pellet ablation cloud via SRSM

Spatially-resolved spectral measurements are conducted on spectroscopic data that have been deemed adapted for SRSM analysis (cf. chapter 4). The goal is to learn more about the inner structure of plasmoids through the analysis of spectra obtained from photons emitted by slices of a same plasmoid. The method used to produce those spectra is not trivial, and is explained extensively in chapters 2 and 3. In addition, not all of spectra obtained via this method can be analyzed pertinently. So a procedure whose aim is to assess the capability of a dataset to be studied has also been developed (cf. chapter 4). Once a dataset is selected for analysis, its spectral profile is compared with a synthetic spectral profile obtained with a spectral model. The spectral profile in question refers to the series of spectra emitted by the successive slices of the observed plasmoid. The spectral model used to produce the synthetic spectra has been developed with the sole intent to reproduce the spectra emitted from fuel pellet ablation clouds, and is based on a model that has already been proven to fit accurately such spectra (cf. ref. [12]). The main originality of this study resides in the way one of its parameter is processed. An important conceptual inconsistency that has been raised in a previous study [14] led to the reassessment of a critical aspect of the theory on plasmoid modeling. The so-called Complete Local Thermodynamic equilibrium (CLTE) is put to the test, and its validity is denied in at least one case of study. An apparently more accurate model based on a non-CLTE approach is presented. The conceptual pivot of this model consists in breaking the strong dependence of few plasma parameters imposed by the CLTE approach. Thanks to this, more freedom is given to the fitting procedure, and better agreements are obtained.

The sixth chapter is divided into three sections. The first section presents the spectral model with a focus on the radiative processes involved in the photons production. Also, two different declinations of the spectral model are detailed. The second section presents the fitting procedure with a focus on the fitting parameters, the fitting method used and the expected behavior of the code in function of how its input parameters change. The third section contains the results and discussion of results of the study of the spectral profile for the case of study introduced in chapter 4.

5.1 A spectral model for hydrogen pellet ablation clouds

In this section, details about the different modules that compose the spectral model are given. Firstly, the supposed characteristics of the studied plasma are presented. Secondly, the different radiative processes that are supposed to contribute to the spectra emitted by ablation clouds are introduced one-by-one. Thirdly, some relevant processes that are supposed negligible and the reason(s) as to why they are neglected are also introduced.

5.1.1 Plasma of hydrogen pellet ablation clouds

Ablation clouds, or plasmoid are, by definition mostly composed of plasma. The real structure of plasmoid is, in fact more complicated than that as its core is a solid pellet. However, its dimensions compared to the gas that surrounds it and the fact that no light is actually produced by it makes it usual to not consider pellets in the theoretical spectroscopic models. Same can be said from the neutral gas directly surrounding the pellet, although more and more models that starts to appears do consider it. As of yet, and as far as the author is aware of, no observed spectrum have been able to be linked to a molecular emission coming from this layer of gas.

The kind of plasmoid studied in this chapter is not representative of all of the wide variety of plasmoids that can be found in MCF plasmas. However, far from having the pretension to explain how all the plasmoids have to be processed, the purpose of this thesis is to bring in more new elements which show that there is no one-size-fits-all approach possible in the study of the plasma of pellet ablation clouds.

Quasi-neutrality stands

For now, choices need to be made on aspects of the plasma that have been extensively treated already. For example, let the quasi-neutrality supposition stands. With

$$n_\mathrm{e} = n_\mathrm{i}\,, \tag{5.1}$$

such supposition is not unrealistic as the plasma considered is mainly composed of what the fuel pellets are made of, that is, pure hydrogen isotopes. Moreover, inside plasmoids, the plasma is considered to be in some sort of equilibrium which allows for the populations it is made of to stay equally and homogeneously distributed. The equilibrium meant here implies that the scale of the size of the system analyzed larger than that of the Debye length (cf. Debye shielding). Also, the scale in time the must be less or of the order of the plasma frequency for the interactions between the charged particles of the plasma to not be impeded by collisions with neutral particles.

Isotropic, strongly correlated plasma

Plasmoids observed in MCF plasmas can be considered as isotropic, high density plasma whose internal structure is highly collision driven. Let also the condition

$$T_\mathrm{e} = T_\mathrm{i} \geq T_\mathrm{a}\,, \tag{5.2}$$

stands. The relatively high density found in most plasmoids ensures that the collisions processes stay frequent and consistent. It results that the states of the particles composing a plasmoid are closely bounded by a strong coupling parameter. The coupling parameter Γ defined as the ratio between the Coulomb energy and the Thermal energy of the plasma studied is a convenient way to assess the state of a plasma in spectroscopy. It has just been mentioned that the plasma in plasmoid is supposed to be isotropic. Even though plasmoids are actively molded by the magnetic field surrounding them, it is supposed that the way the plasma inside them moves pretty much freely.

Nature of the slices observed

When volume of plasmas are observed, it is usual to attempt to spatially reconstruct the plasma from within. However, due to the nature of the experimental method, this procedure referred to as Abel inversion spectroscopy [22] is not possible to conduct. Indeed, when light is collected by the optics of the main observation system, the photons are indiscriminately packed together and sent to a spectrometer. It mean that any spatial information is lost during the recording process.

Hydrogen isotopes (hydrogen vs deuterium)

Since 2017 in LHD, the composition the fuel pellets are made of can vary between fully hydrogen of fully deuterium. In consequence, the kind of plasmas studied in LHD can be either or both of them. From a spectroscopic point-of-view, hydrogen and deuterium are extremely similar. Comparative studies conducted about them did not, as of yet, found any significant difference (e.g. ref. [15]). This supposition simplifies greatly the analyzes and, considering the low accuracy of the observation system used for this experiment, it seems reasonable to consider both as the same. From now on, when the term “hydrogen” is employed, it can mean hydrogen and deuterium in function on the context it is used in.

Spectroscopic analysis

The plasmas observed are turned into spectra ranging from 400 to 700 nm. It means that the study of the plasmoid(s) is focused on the so-called Balmer series emission lines and the surrounding radiative continuum. Due to some instrumental limitations and theoretical simplifications, the emission line located near 656 nm, also referred to as Balmer-α (H-α, D-α, etc) line is discarded from the procedural part of the analysis. Although some information can still be extracted from it, the fact that it often saturates (due to a low camera dynamic range) and that it is subjected to a radiative process not included in the spectral model (cf. subsection 5.1.4) have it so that this line cannot be studied accurately. In addition, the wavelength region where the Balmer series emission lines are so close that they become a continuum (referred to as transition to the continuum) are also discarded from the fit. Their observation is “doable” with this observation system, but the sensitivity of the spectrometer under low brightness signal is such that the signal/noise ratio gets ugly. Focus of the analysis is mainly put on the region between the Balmer-β and Balmer-γ lines as well as the continuum between the Balmer-α and Balmer-β lines.

5.1.2 Contributions to the radiative continuum

Radiative recombination continuum

The radiative recombination continuum is linked to the widely mentioned recombination process. A recombination process occurs when an ion and an electron recombine into an atom. This is a radiative process so a photon is produced in the process. The total spectral power radiated by a slice of plasmoid via this process can be calculated with the following relation:

$$\mathrm{P}^{\mathrm{rec}}(\nu) \;=\; \sum_n p^{\mathrm{rec}}_{\mathrm{n}}(\nu) \;=\; \sum_n n^2\,\Upsilon\,\sigma_{\mathrm{ion}}(n,\nu)\,\Big(\frac{1}{k_{\mathrm{B}}T_{\mathrm{e}}}\Big)^{\frac{3}{2}}\exp\Big(-\,\frac{h\nu\,-\,E^{\mathrm{ion}}(n)}{k_{\mathrm{B}}T_{\mathrm{e}}}\Big)\,\nu^3\,n_{\mathrm{e}}\,n_{\mathrm{i}}\,, \tag{5.3}$$

where:

- n corresponds to the level of excitation of the atom produced by the process
- $E^{\mathrm{ion}}(p)$ is given in [J] and corresponds to the ionization potential of the emitting particles found in the excited level n
- $\sigma_{\mathrm{ion}}(n,\nu)$ is given in [m^{-2}] and corresponds to the ionization cross-section for the atoms of excited level n
- $k_{\mathrm{B}}T_{\mathrm{e}}$ is given in [J] and corresponds to the temperature of the perturbing particles (electrons)
- hν is given in [J] and corresponds to the energy of the emitted photons considered, with the frequency ν is given in [Hz] and the Planck constant h is expressed in [J.s].
- Υ is a constant given in [J.m.s^3] and is defined by the relation $\sqrt{\frac{2}{\pi}}\,\frac{h^4}{m_{\mathrm{e}}^{3/2}c^2}$

Radiative attachment continuum

The attachment recombination continuum is linked to the less commonly mentioned attachment process. An attachment process occurs when an atom and an electron combine into a negative ion. This is also a radiative process so a photon is produced after the reaction. The total spectral power radiated by a slice of plasmoid via this process can be calculated with the following relation:

$$\mathrm{P}^{att}(\nu) \;=\; \Upsilon\,\sigma_{det}(\nu)\,\Big(\frac{1}{k_{\mathrm{B}}T_{\mathrm{e}}}\Big)^{\frac{3}{2}}\exp\Big(-\,\frac{h\nu\,-\,E^{AE}}{k_{\mathrm{B}}T_{\mathrm{e}}}\Big)\,\nu^3\,n_{\mathrm{e}}\,n_{\mathrm{a}}\,, \tag{5.4}$$

where:

- E^{AE} is given in [J] and corresponds to the energy required for an atom or ion to release an electron (e.g. 0.754 eV for hydrogen)
- $\sigma_{\mathrm{det}}(\nu)$ is given in [m^{-2}] and corresponds to the detachment cross-section for the negative ions

5.1.3 Contributions to the emission lines

Lineshapes I: Stark-broadening

The Stark-broadened emission lines are modeled from a database (cf. ref. [25]). The database contains tables of profiles of emission lines which have been synthesized with a code based on the Model Microfield Method (MMM). Half-profiles of lineshape can be derived from these tables from two input parameters: T_e and n_e. This database has initially been built with stellar plasmas in mind but it is applicable to a wide range of other applications as well. For example, this database has already been used to study MCF plasmas, such as in divertor plasmas (cf. ref. [26]) and plasmoid plasmas (cf. ref. [12, 14, 16]).

Limiting factors of this database are the so-called Inglis-Teller limit (cf. ref. [27]) and Hooper coefficient (cf. ref. [28]). Due to these limiting factors, it is important to note that it is not possible to study emission lines with high p if the electron density is too high and/or the electron temperature is too low. It is also important to note that no line shift and/or asymmetry is taken into account for this study (cf. subsection 5.1.4).

Lineshapes II: Instrumental-broadening

As demonstrated in chapter 3, the instrumental broadening due to the observation system is not negligible, and so must be included into the calculations. The instrumental broadening is added to a spectrum by convoluting the emission lines with a gaussian distribution function whose HWHM is $w^{1/2}_{\mathrm{inst.}} = 1.0$ nm.

Line-intensity: CLTE vs non-CLTE approach

The intensity of the emission lines is expressed in term of the radiant flux Φ [W]. A convenient definition of Φ can be found in the fourth chapter of ref. [17]. Considering a transition $p \rightarrow q$, where p is the principal quantum number of the upper level, and q is to the principal quantum number of the lower level, Φ is given as

$$\Phi(p,q) \;=\; hv\,A(p,q)\,n^p_\mathrm{a}\,V_\mathrm{s}\left(\frac{d\Omega}{4\pi}\right), \tag{5.5}$$

where:

- n^p_a is given in [m^{-3}] and corresponds to the density of the emitters (atoms in this case) found in the excited state p.
- A(p,n_{down}) is given in [s^{-1}] and corresponds to the Einstein spontaneous emission probability coefficient for the transition $p \rightarrow n_{down}$.
- V_s is given in [m^3] and represents the volume of the light source emitting the photons considered (i.e. the volume of the observed slice of plasmoid).
- $\frac{d\Omega}{4\pi}$ is given in sr^{-1} and is referred to as the solid angle. It is a dimensionless value that expresses how big the light source appears to be from the point of observation.

The absolute intensity of the lines directly depends on the population level of the neutral population through the n_{a}^{p} coefficient. It is possible to calculate the intensity of the lines (i.e. the population of the emitters) from two different approaches. The first method considers that the plasma studied is in the so-called Complete thermodynamic Equilibrium (CLTE) which allows one to find all of the population levels from their neighboring ones. The second method employ a more general approach referred to as a the collisional-radiative model (CRM).

The schema shown in figure 5.1 is a simplified illustration of the concept behind the CRM. At the left of the figure, an energy diagram indicates the states a particle can be in.

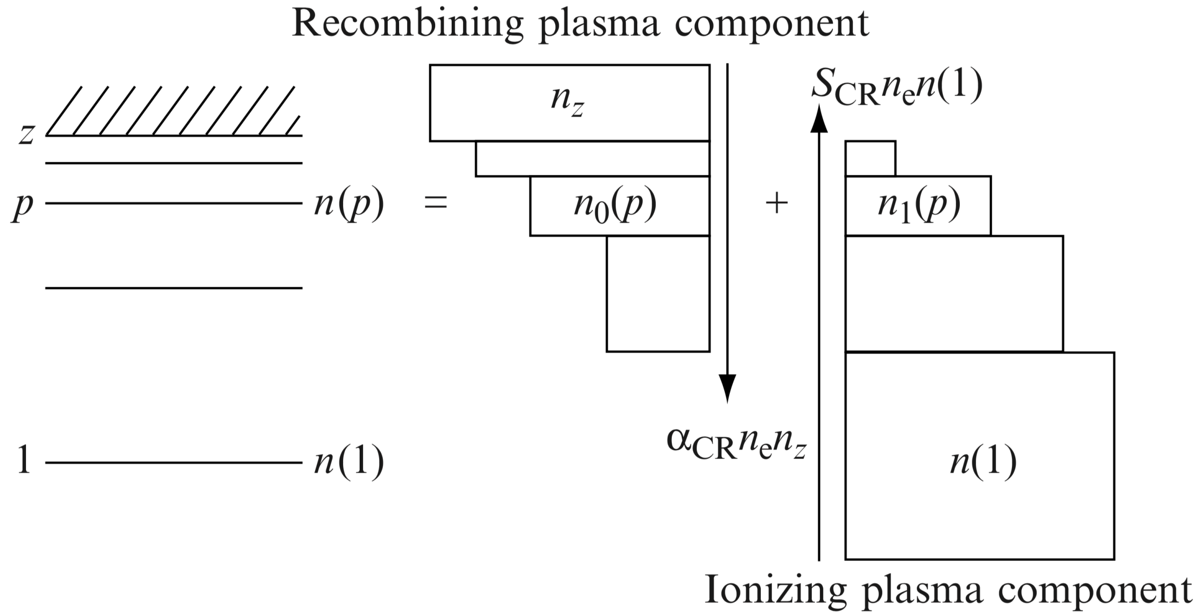

Figure 5.1: Decomposition of the neutral density into two components: one recombining component and one attachment component [source: “Plasma spectroscopy”, p.9 by T. Fujimoto (2004)]

To the state $n(1)$ which represents the ground state (i.e. particle not excited) to the upper limit n_{z} where the particle is considered to be fully ionized. At the left of the figure, it is explained with a figure that it is possible to virtually dissociate the particles that tend to ionize (going “upward” in the energy excitation scale, up to the fully ionized state), to the particles that tend to recombine (going “downward”in the energy scale, down to the ground state). As such, with this mindset, the parameter n_{a}^{p} can be defined such that

$$n_{\mathrm{a}}^{p} = \mathrm{R}_0(p)\, n_{\mathrm{e}}\, n_{\mathrm{i}} + \mathrm{R}_1(p)\, n_{\mathrm{e}}\, n_{\mathrm{a}}^{1}, \tag{5.6}$$

where $\mathrm{R}_0(p)$ and $\mathrm{R}_1(p)$ are the population coefficients related to the recombining plasma component and the ionizing plasma component, respectively.

When a plasma is dense enough, there is a point where it can be considered as being in a so-called Local Thermodynamic Equilibrium. In such case, it is possible to express the ionizing plasma component of the CRM in terms of the recombining plasma component alone so that n_{a}^{p} becomes:

$$n_{\mathrm{a}}^{p} = \mathrm{Z}(p)\, n_{\mathrm{e}}\, n_{\mathrm{i}}\,, \tag{5.7}$$

where $\mathrm{Z}(p)$ is the Saha-Boltzmann equation

$$\mathrm{Z}(p) = \frac{\mathrm{g}(p)}{2\mathrm{g}(1)} \left(\frac{h^2}{2\pi m k_{\mathrm{B}} T_{\mathrm{e}}}\right)^{3/2} \exp\left(\frac{R_{\mathrm{i}}}{p^2 k_{\mathrm{B}} T_{\mathrm{e}}}\right)\,. \tag{5.8}$$

The coefficients $\mathrm{g}(p)$ and $\mathrm{g}(1)$ correspond to the statistical weight of the excited level p and the ground state of the particles, respectively.

Different degrees of "LTE-ness" are possible. Extensive research has been and still is being done to find out how to consider which degree to choose when studying plasmas, account of this research can be found in the following references [17, 29]. In shot, such degree is supposed to be mainly linked to the density of the studied plasma. The denser a plasma is, the lowest p can be.
In extreme cases where the density is very high, the Saha-Boltzmann equation can even be applied to the ground state level where n_{a}^{1}. Under such circumstances, the plasma is considered to be the so-called Complete LTE.
Because plasmoids are usually extremely dense, it is usual to consider that they are in (C)LTE. However, in the wake of the results found in [14], it has been proposed that the degree of "LTE-ness" at which plasmoids are in might not be only decided by how dense they are. This is why the proposed spectral model possesses two different declinations, one base on the CLTE, and another based on the CRM (a.k.a. non-CLTE).

5.1.4 Some neglected contributions

Radiative continuum: Bremsstrahlung

The process associated to the Bremsstrahlung, or braking radiation, occurs when two charged particles collide and one of the particle ends up with less energy than what it had before the collision took place. The energy lost by the decelerating particle is emitted under the form of a photon. Neutrals are not directly involved in the photon emission process so the radiation emitted from the Bremsstrahlung is a continuum. In other words, because both colliding particles are not bounded to a nucleus, the level of energy they can take is ideally infinite. It implies that the photon emitted by this process is not limited by the quantic nature of a bounded particle (cf. the so-called "particle in a box" model). Different declinations of the Bremsstrahlung exists, but for non-relativistic, thermally equilibrated plasmas, the so-called thermal Bremsstrahlung is the dominant one. Considering the composition of the plasmoid studied, the braking radiation involve the deceleration of an excited electron after it crosses the path of a proton.
The power emitted by this radiation is proportional to $n_{\mathrm{e}} n_{\mathrm{i}}$, where n_{i} is the proton density and to $\sqrt{T_{\mathrm{e}}}$. Considering that $n_{\mathrm{e}} \sim n_{\mathrm{i}}$, this density dependence makes the Bremsstrahlung a potential contribution of interest for spectral modeling.

However, it has already been shown that due to the low cross-section of the collision process in the visible range, this radiative process is negligible compared to the other considered contributions (cf. ref. [12]).

Emission lines I: Zeeman Shifting

The Zeeman splitting is a process from which an emission line will split under the influence of the magnetic field strength surrounding the emitting particles. A simple way to express the splitting property of the Zeeman effect is via its perturbed Hamiltonian:

$$\mathrm{H} = \mathrm{H}_0 + \mathrm{V}_m \,, \tag{5.9}$$

where H_0 is the unperturbed Hamiltonian and V_m is the magnetic field induced perturbation

$$\mathrm{V}_m = -\vec{\mu}\,\vec{\mathrm{B}} \,, \tag{5.10}$$

where $\vec{\mu}$ and $\vec{\mathrm{B}}$ are the magnetic moment of the emitter considered and the magnetic field the emitter is subjected to, respectively.
$\vec{\mu}$ is intrinsically linked to the quantum mechanics properties of the emitter via its total angular momentum $\vec{J}$. So it can become complicated to calculate under certain circumstances where the magnetic field becomes too important, and the total angular momentum cannot be expressed via its straightforward way $\vec{J} = \vec{L} + \vec{S}$ (cf. LS coupling).

Thankfully, the plasma configurations studied here never reach that point, and the Zeeman split for, lets say, the Balmer beta line of hydrogen is found to be negligible in front of the instrumental function (i.e. approx. 1/100 of $w_{1/2}^{inst}$ at $\mathrm{B} = 1.5$ T).

Emission lines II: Thermal doppler broadening

The Thermal Doppler Broadening is a process from which an emission line will be broadened because the light sources (photons emitters) are moving away or forward the observation location (a.k.a. Doppler shift).
It is question of a thermal broadening because the emitters are moving due to the thermal agitation the plasma containing the emitters are in. Due to the randomness of the process and the great amount of emitting particles, the randoms shifts are seen as a broadening of the emission line. Supposing the particles considered follow a typical Maxwell-Boltzmann velocity distribution, and that the emitting particles are non-relativistic, The Line broadening can be explained by a gaussian with a HWHM that is equal to

$$w_{1/2}^{doppler} = \frac{w}{c}\sqrt{2\ln 2\,\frac{k_{\mathrm{B}}T_{\mathrm{a}}}{m_{\mathrm{a}}}} \,, \tag{5.11}$$

where T_{a} and m_{a} correspond to the temperature and the mass of the emitting particles. In the plasmoids considered in this study, this contribution is negligible (i.e. approx. 1/1000 of $w_{1/2}^{inst}$ for $k_{\mathrm{B}}T_{\mathrm{a}} = 1.0$ eV).

Emission lines III: Lines asymmetry

Any asymmetry that could be provoked by a physical process is not included into this version of the spectral model. Emitting particles can be perturbed in such a way that a certain number of them are influenced more than the others. Indeed, it is not uncommon to find cases where a too dynamic ionic population perturbs the emitters in such a way that they emit more photons of a certain energy, inducing some asymmetry to the wings of the emission lines. Or, in very dense plasmas, to have its molecular population perturbs emitted near the transition level and induces some asymmetry at the center of the peak of the emission lines.
Simply put, emission lines can be asymmetric for reasons other that an instrumental one. The study of lines asymmetry is not uncommon (cf. ref. [30]). It is relatively well understood and documented. However, from the previous results of spectroscopic observation of plasmoids [12], it has not been judged necessary to implement that aspect into the spectral model.

Emission lines self-reabsorption

When the plasma self-reabsorption, or opacity is mentioned, it means that the emitted photons with an energy close to the transition energy of other particles are recaptured. When the emission line of a plasma where this phenomenon occurs is observed, it appears as if its central region is lower and its wings more important than the emission line of a plasma where no self-reabsorption occurs.
A quantitative analysis of spectra emitted from plasmas similar to the ones studied here (hydrogen ablation cloud in the visible range) has already been conducted [12]. The study found that whereas the opacity on the Balmer-α line is consequent. However, it was also found that this phenomenon can be neglected for the other emission lines.
Plasmoid opacity is considered as negligible in this study as the Balmer-α line is not considered for fitting.

5.2 A fitting procedure for the spectral model

In this section, details about the fitting procedure used to analyze the spectra are given. Firstly, the fitting method at the base of the SRSM is presented. Secondly, the behavior of the spectra outputted by the model in function of the input parameters considered is detailed.

5.2.1 Behavior of spectral model

The plasmoid parameters to keep an eye on are the electron density n_e and temperature T_e, the neutral density of the ground state n_a^1 and the volume of the observed slice of plasmoid V_s.

Electron density n_e

The electron density contributes to every aspect of the spectral model, but its most significant contribution is via the Stark-broadening. When the density of a plasma increases,

the photon emitters (i.e. excited neutrals of the plasma) are stimulated more frequently. This leads the width of the emission lines to be wider.
While the radiative recombination continuum is n_{e}^{2} dependent (cf. eq. 5.3), the radiative attachment continuum is only n_{e} dependent (cf. eq. 5.4).

Electron temperature T_{e}

The electron temperature is, more or less, involved with all of the contributions. The full impact of this parameter is not evident to highlight, but its impact on the slope of the radiative continuum is clearly visible from eq. 5.3 and 5.4.

Neutral density of the ground state n_{a}^{1}

The influence of the neutral density is mostly integrated to the line-intensity aspect of the spectral model. As such, this parameter is fixed in the CLTE declination of the spectral model, and is determined from the Saha-Boltzmann equation (eq. 5.8). In the non-CLTE declination of the spectral model, n_{a}^{1} is considered as a fitting parameter via the equation 5.5.
The radiative attachment continuum is n_{a}^{1} dependent as well. If the radiative continuum between the Balmer-α and β lines is observed with enough clarity, this continuum constitutes an efficient way to estimate the value of n_{a}^{1} via the non-CLTE approach.

Volume of observed slice of plasmoid V_{s}

The volume of V_{s} acts as a correction coefficient for the spectra as all contributions are V_{s} dependent.

5.2.2 Least-squares fitting method

The spectral model is implemented into a fitting procedure. A fitting procedure (GNU Scientific Library: FMinimizer) is called from a ruby script that receives as input the path of a spectral datafile and initial parameters for n_{e}, T_{e}. V_{s} and n_{a}^{1} (non-CLTE fitting procedure only). The iterative fitting procedure is then started and then fed with the spectral data, and a new synthesized spectrum at every iteration until it find a best fit or reach the maximum amount of authorized iterations is reached. Synthetic spectra are produced by a spectral modeling code based on the spectral model given in section 5.1. The quality of the fitting is calculated via the χ^2 coefficient.

χ^2 minimization

The χ^2 coefficient chosen to fit the experimental data is

$$\chi^2 = \sum_i \Big(I_{\mathrm{Exp.}}(i) - I_{\mathrm{Syn.}}(i) \Big)^2 , \tag{5.12}$$

where, i corresponds to the data-points. $I_{\mathrm{Exp.}}(i)$ and $I_{\mathrm{Syn.}}(i)$ correspond to the logarithmic intensity values of the experimental spectrum and the synthetic spectrum, respectively.

This unusual definition is motivated from the fact that the observed spectra contain wide low-ceiling continuum and narrow high-peaked emission lines. The use of logarithmic values increases the contribution of the continuum in the fitting procedure that would otherwise have been buried into the high intensity values obtained for the lines.

A 2-steps fitting procedure

The spectral model can become unstable due to the number of fitting parameters. It is possible to ease the load of the code by fixing certain parameters which are already known. Hopefully, There is a way to determine the n_e parameter of a spectrum without requiring the intervention of any other parameters.
Figures 5.2 show normalized lineshapes synthesized from the Stehle database. The figure to the left corresponds to two lineshapes of the Balmer-β line obtained with T_e fixed at 1.0 eV. The black lineshape corresponds to $n_\mathrm{e} = 1 \times 10^{23}\,m^{-3}$ while the blue one corresponds to $n_\mathrm{e} = 2 \times 10^{23}\,m^{-3}$. The figure to the right corresponds to two lineshapes of the Balmer-β line obtained with n_e fixed at $1 \times 10^{23}\,m^{-3}$. The black lineshape corresponds to $T_\mathrm{e} = 0.5$ eV while the blue one corresponds to $T_\mathrm{e} = 1.0$ eV. The values used for the parameters correspond to values already measured in plasmoids (observed in LHD at least). It is clear from the figures that the Stark-broadening is mainly dependent on the n_e parameter that the T_e parameter can be fixed to any value close to 1.0 eV.
The 2-steps fitting procedure consists of fitting the isolated the Balmer-β line extracted from spectroscopic data, and to reuse the obtained n_e as a fixed variable to fit the complete spectrum. An application of the 2-steps fitting procedure is employed in section 5.3.

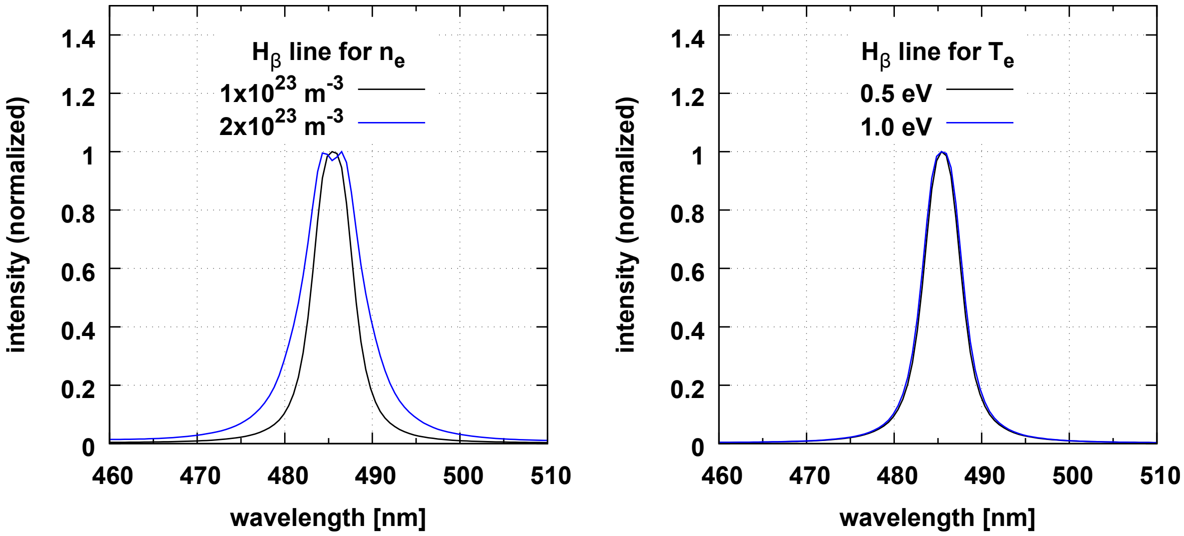

Figure 5.2: Stark-broadening: strong n_e, weak T_e dependence. (left) Normalized spectra of the Balmer beta line modeled by the Stehle database for two different electron density and a fixed electron temperature of $1.0\,eV$. (right) Normalized spectra of the Balmer-β line modeled by the Stehle database for two different electron temperatures and a fixed electron density of $1.0 \times 10^{23}\,\mathrm{m}^{-3}$

5.3 SRSM of case of study study #135454

In this section, the case of study which has been confirmed for SRSM in chapter 4 is analyzed. Firstly, an overview on the calibrated spectra that are analyzed is given. Secondly, results obtained from the study are shown. Thirdly, a discussion of the results is presented.

5.3.1 Calibrated spectrum

Figure 5.3 shows samples of calibrated spectra obtained from the light emitted from slices of the sixth plasmoid of the LHD plasma discharge #135454. In total four spectra whose spectral power is plotted in function of the wavelength are observable. Each spectrum correspond to a different slice of the plasmoid. Thanks to the imaging data, it is possible to associate each slices to a location in the plasmoid along its direction of elongation. From fig. 5.3, it is possible to see that the slices located at the edges of the plasmoid emit significantly less visible light than slices located in the inner body of the plasmoid. In addition, the widths of the lineshapes suggest strongly that the plasma parameters, especially n_{e}, vary along the direction of observation.

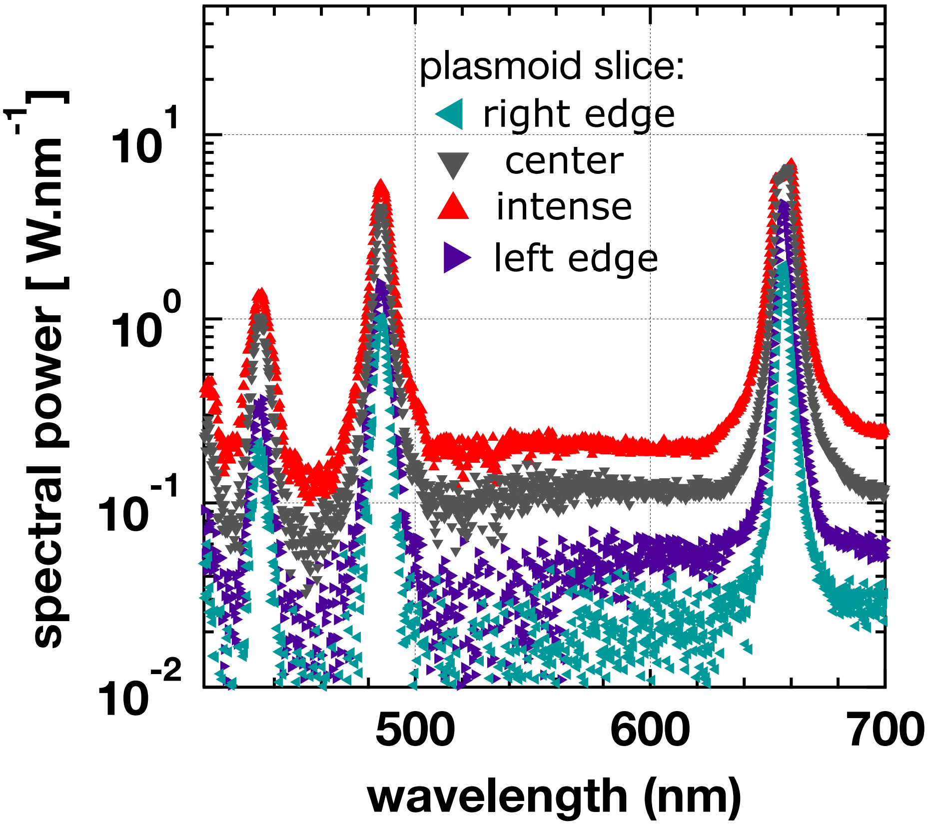

Figure 5.3: Calibrated spectra obtained from different slices of plasmoid where each spectrum corresponds to a different location in the plasmoid along its direction of elongation

5.3.2 Parameters profiles

Lineshape pre-fitting

Figure 5.4 presents samples of the results obtained following the 1st step of the 2-steps procedure detailed in section 5.2. The isolated Balmer-β line (where the continuum, supposed constant in this region, has been removed) is fitted with a simplified spectral model where the radiative continuum contributions has been removed and the intensity correction is only applied to one unique fitting parameter. A gaussian instrumental broadening

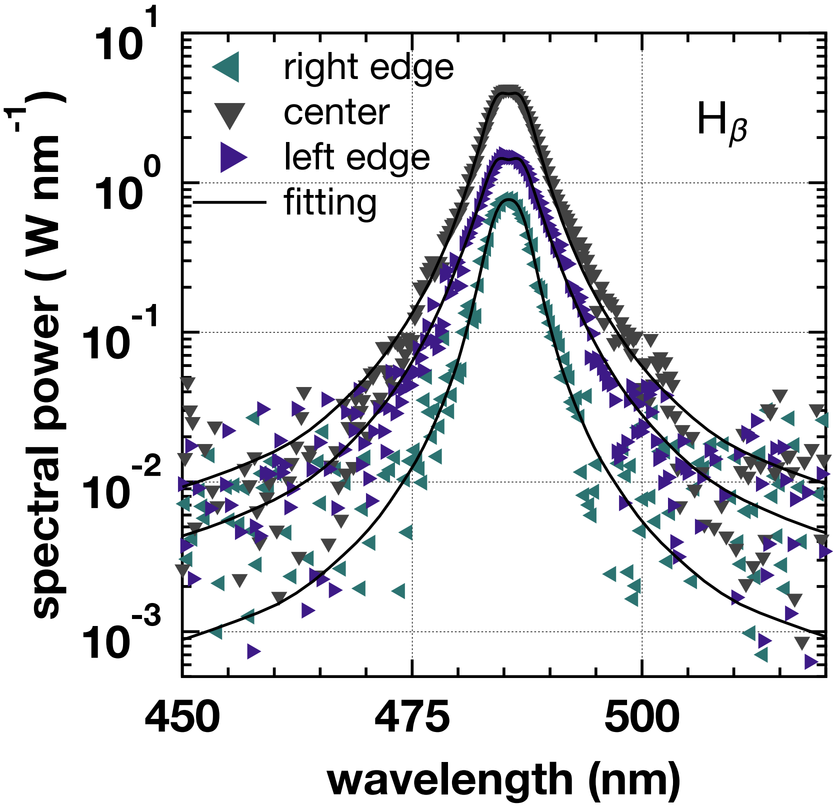

Figure 5.4: Stark-broadened spectral lineshapes fitting results for isolated Balmer-α lines at three different locations along the direction of elongation of the plasmoid. An instrumental broadening of 1.0 nm is added to the synthetic spectra

is also included in the calculations. Values of the electron density profile obtained from these fittings is shown in fig. 5.7.

CLTE vs non-CLTE

Figure 5.5 presents samples of the results obtained following the 2nd step of the 2-steps procedure detailed in section 5.2. The experimental data (gray dots) is fitted via least squares fitting using the two different approaches. The CLTE approach (blue dashed line) and the non-CLTE approach (red continuous line) yield diverging fit and can thus be compared. As can be seen from the results, the non-CLTE approach is more reliable than the CLTE one. The lines intensity of the synthetic spectrum is better represented by the non-CLTE approach. As importantly, the continuum between the Balmer alpha

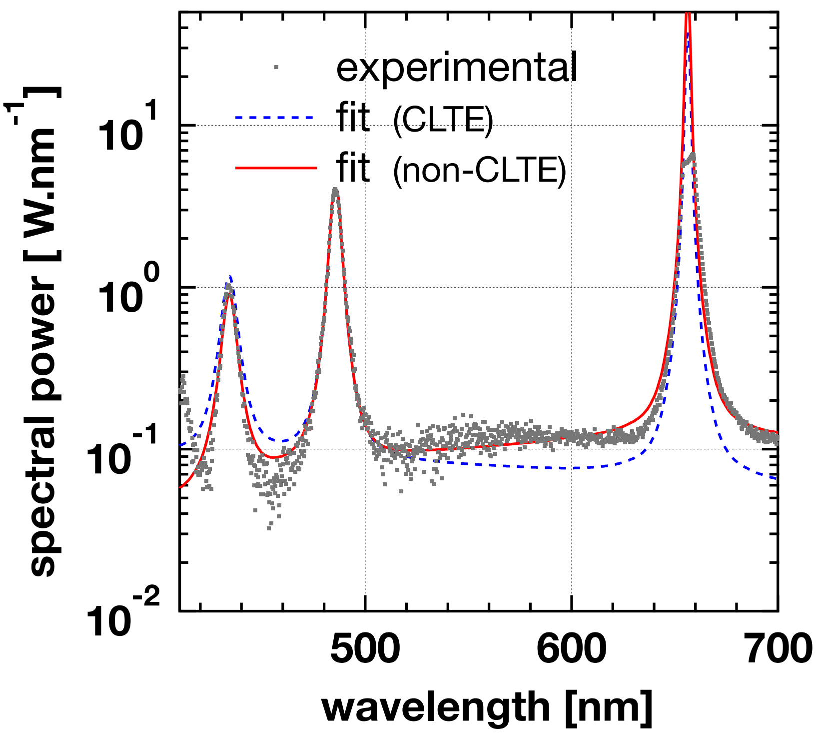

Figure 5.5: Spectral fitting results for CLTE vs non-CLTE approaches against the spectrum of the most intense slice of plasmoid recorded

and beta line is better justified by the non-CLTE too. The same tendency is observed for all of the spectra produced by the observation device. Results of the non-CLTE approach for this fit are $1.4 \times 10^{23}\,\mathrm{m}^{-3}$, 0.41 eV, $1.7 \times 10^{-9}\,\mathrm{m}^{3}$ and $3.2 \times 10^{26}\,\mathrm{m}^{-3}$ for n_{e}, T_{e}, V_{s} and n_{a}^{1}, respectively. The full profiles are shown in fig. 5.7 and 5.8. Results of the CLTE approach for this fit are $1.36 \times 10^{23}\,\mathrm{m}^{-3}$, 1.00 eV and $2.0 \times 10^{-8}\,\mathrm{m}^{3}$ for n_{e}, T_{e} and V_{s}, respectively. The n_{a}^{1} of the CLTE approach is calculated from the Saha-Boltzmann calculation (cf. eq. 5.8), hence depends on the parameters of n_{e} and T_{e}. The different results for T_{e} and the method n_{a}^{1} is derived with must be the reasons why the non-CLTE approach, by not being bounded to the Saha-Boltzmann calculation, gives better fitting results.

To put these results into contrast, the figure 5.6 presents a fitting result that have been obtained from the study conducted in ref. [12]. The figure shows the experimental spectrum (black dots) obtained from the temporal observation of the light emitted from a plasmoid, from the Balmer-α line down to the transition to the continuum and beyond. The synthesized spectrum (black continuous line) is also drawn with its main components the radiative recombination continuum (P_{R}), the radiative attachment continuum (P_{A}), the Bremsstrahlung (P_{B}) and the Stark-broadened emission lines (dashed lines). Also, the self-reabsorption effect has been computed for the Balmer-α line. Contrarily to the present case of study, the study was not a SRSM, and the plasmoid analyzed did not go deep inside the plasma of the LHD. In addition, configuration the MCF plasma was different from the case of study with, among others, a magnetic field strength significantly more important. As a results, the intensity ratios of the emission lines and the slope of the radiative continuum between the Balmer-α and Balmer -β lines represents exactly what should be if it was in CLTE.

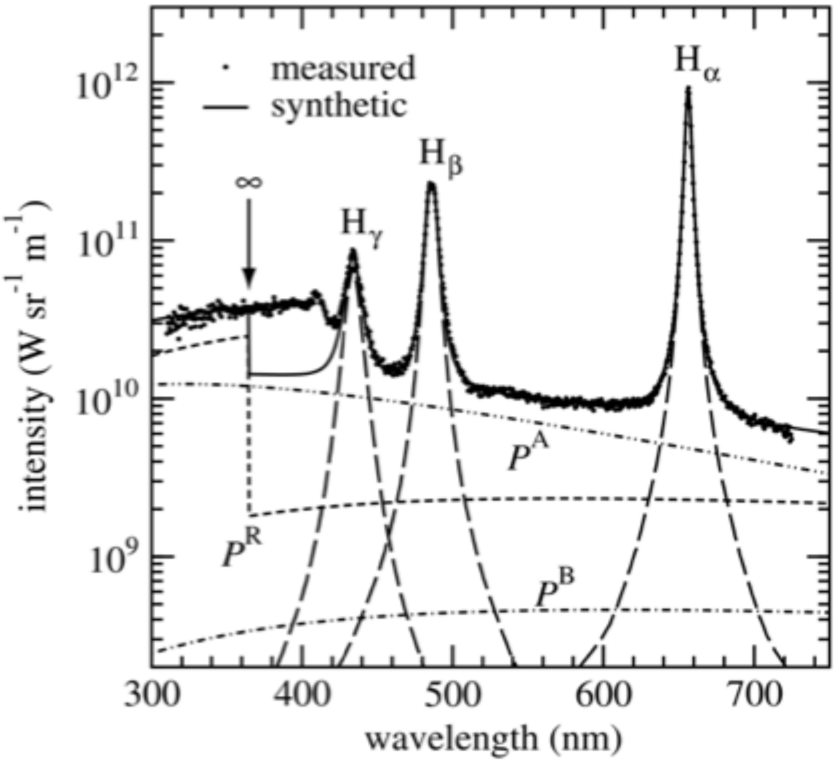

Figure 5.6: Successful CLTE spectral fitting results of plasmoid temporally observed in the edge region of LHD plasma (not a case of SRSM) [source: "Experimental verification of complete LTE plasma formation in hydrogen pellet cloud", by M. Goto *et. al.* (2007)]

Profiles of plasmoid parameters

Figures 5.7 show the profile of n_e (blue circle dashed line) and T_e (red square dashed line) in function of the slice of plasmoid analyzed. The bottom figure show the same results as the top one, but the axis of temperatures have been cropped to amplify the variation of the parameters. The profile of the electron density is globally more important inside than at the edges. This is to be expected considering that the ablating pellet located a the core acts as a source of hydrogen. When focusing on the internal structure of the plasmoid, an asymmetric hill shaped n_e profile can be observed. The maximum value of n_e is not at the center of the plasmoid but on its right wing. The left wing of the plasmoid slightly decreases toward the central region. Values for n_e obtained in the plasmoid are in the range of what has already been derived from previous studies conducted in LHD (e.g. ref [14]). Reasons to suppose that the small dipped area located near the center of the plasmoid is real because such observation has also been done with similar results in LHD [16] and elsewhere [15].

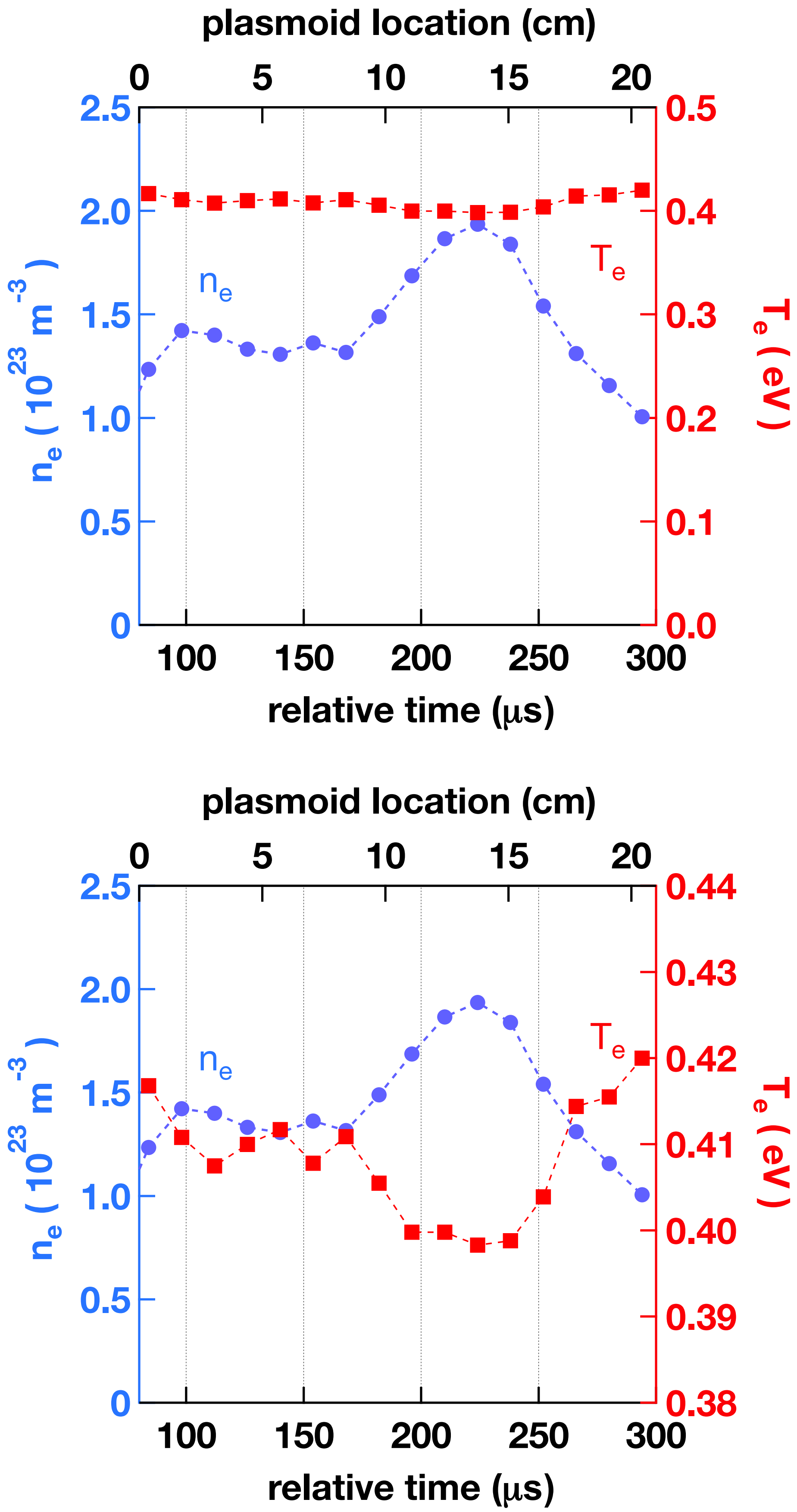

Figure 5.7: Profiles of n_e and T_e in observed plasmoid derived from the 2-steps fitting procedure

On a first glance, the profile of the electron temperature seems to be flat. However, with its shortened y-axis, the bottom figure reveals that the profile of T_e is actually varying. Moreover, the behavior of T_e is in exact opposition with n_e. Results of the profile of T_e derived from this study are in contrast with what has been found in past studies conducted in LHD. Whereas T_e is usually measured to be around 1.0 eV (e.g. ref. [14]), the present results puts T_e around 0.41 eV.
The behavior itself of T_e is also contradictory with what has been derived in ref. [14]. It does however more or less agree with at least one more recent study conducted on a plasmoid observed in the ASDEX-U tokamak [15] (cf. fig. 1.7).

Figure 5.8 shows the profile of the volume of the slices (black star dashed line) and the electron density (red square dashed line) in function of the slice of plasmoid analyzed. Inside the plasmoid, n_a^1 is about 3 orders of magnitude denser than n_e. The same dip observed in the profile of profile n_e can be outlined in the profile n_a^1. If it is supposed that V_s corresponds to the complete volume of a slice, it suggests that the plasmoid is not cigar shaped. It is not unusual to find asymmetrically shaped plasmoids in MCF plasmas [15]. However, analysis of the data obtained from the fast camera do not tend to corroborate such difference of volume between the left and the right halves of the observed plasmoid. There must be more into it than it appears to be (cf. ref. 5.3.3).

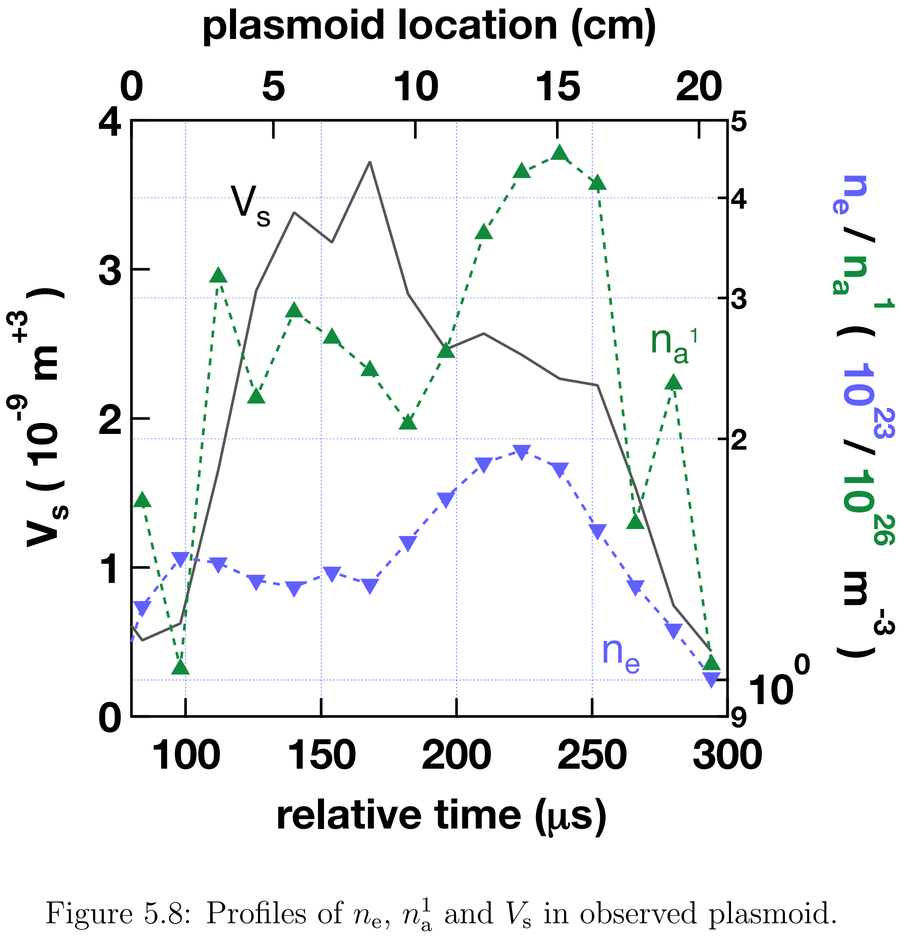

Figure 5.8: Profiles of n_e, n_a^1 and V_s in observed plasmoid.

About the "plasma location" and "relative time" parameters

It is important to note that the "plasma location" is derived from the number of frames the plasmoid has been detected in, with the knowledge of how long a frame is supposed to last (i.e. acquisition time), and how wide the effective FOV of the observation system is. The plasmoid is also supposed to travel through the FOV at a velocity of 1000 m/s. In fact, this supposition is very unlikely if the plasmoid is heavily perturbed and/or its trajectory is modified. Moreover, it has to be noted that the angle of observation of the plasmoid is such that its perceived velocity from the point-of-view of the observation port can be greatly modified. An over-estimation of the velocity (which is very likely) incur an over-estimation of the length of the plasmoid. When the perceived velocity of a plasmoid is slower, what happens is that a same region of a plasmoid may be recorded by more than one frame. Hopefully, this virtual-dilatation of the plasmoid does not change the fact that measurements are conducted all along its observed length of elongation.
The "relative time" is also derived from the number of frames the plasmoid has been detected in, with the knowledge of how long a frame is supposed to last (i.e. acquisition time). The first frame corresponds to a few frames before the plasmoid is effectively detected. Figures that show the profiles of the fitting parameters starts at $t_{\mathrm{rel.}} = 80$ μs. The reasons no data is available before that point are that fitting results are highly inaccurate due to the low intensity of the recorded spectra and the presence of a plasmoid drift (cf. section 4.3).

5.3.3 Discussion of results

Results obtained from this study suggest that the CLTE condition is not valid inside the analyzed plasmoid. Better fitting results are obtained from the non-CLTE approach (cf. fig. 5.5). The profiles of n_{e}, T_{e} and n_{a}^{1} derived from the non-CLTE version of the spectral model (cf. fig. 5.7 and 5.8) do not seem to be physically unrealistic and can even find some consistency when compared with some other sources (cf. ref. [16, 14, 15]).
The physical reason behind the n_{e} and T_{e} mirrored profiles is still unclear. It is be possible that this behavior is due to an attempt for the plasma in the plasmoid to conserve some kind of constant plasma pressure. However, the scale at which T_{e} vary is far too small to really be able to compensate for the variation of n_{e}.
There is still the question of the observed V_{s} and the possibility that it does not correspond to the complete volume of a slice of plasmoid. Indeed, because spatial information is lost when the measurement is done, it is not evident to determine if what is observed corresponds to full slices of plasmoid or to superficial layers of its visible side. Values of V_{s} obtained tend to agree with the latter. As indicated in fig. 5.8, the derived volumes of the slices are in the order of $10^{-9}\,m^{+3}$. By factoring in what is known about the slices of plasmoid (i.e. width of effective FOV is 14 mm) and by supposing that a simplistic cylindrical shape for the plasmoid, it would mean that its radius is a tenth of millimeter. This is of course an unrealistic result, unless, the volumes of slices of plasmoid observed do not correspond to the complete slice but only a slab of it. This would implies that photons emitted by the inner layers of the plasmoid are to reabsorbed or that they do not emit any photon at all.

Ground state neutral density and the binding power of the Saha-Boltzmann equation

Figure 5.9 shows a comparison between the profile of n_a^1 obtained via the non-CLTE approach (green triangles) of the spectral model (i.e. considered as a fitting parameter) and a “Saha-Boltzmann profile” of n_a^1 (pink triangles) that is obtained by feeding the Saha-Boltzmann equation with the n_e and T_e derived from the non-CLTE approach. This figure does not represent a profile obtained via the CLTE approach. What it attempts to show is that the T_e found to fit accurately the non-CLTE spectrum can not reasonably be obtained via the CLTE approach. For the CLTE approach to reach a $n_\mathrm{a}^1 \geq 10^{33}\,\mathrm{m}^{-3}$ when fitting a spectrum, it would mean that the plasma which emitted such spectrum is denser than a solid.

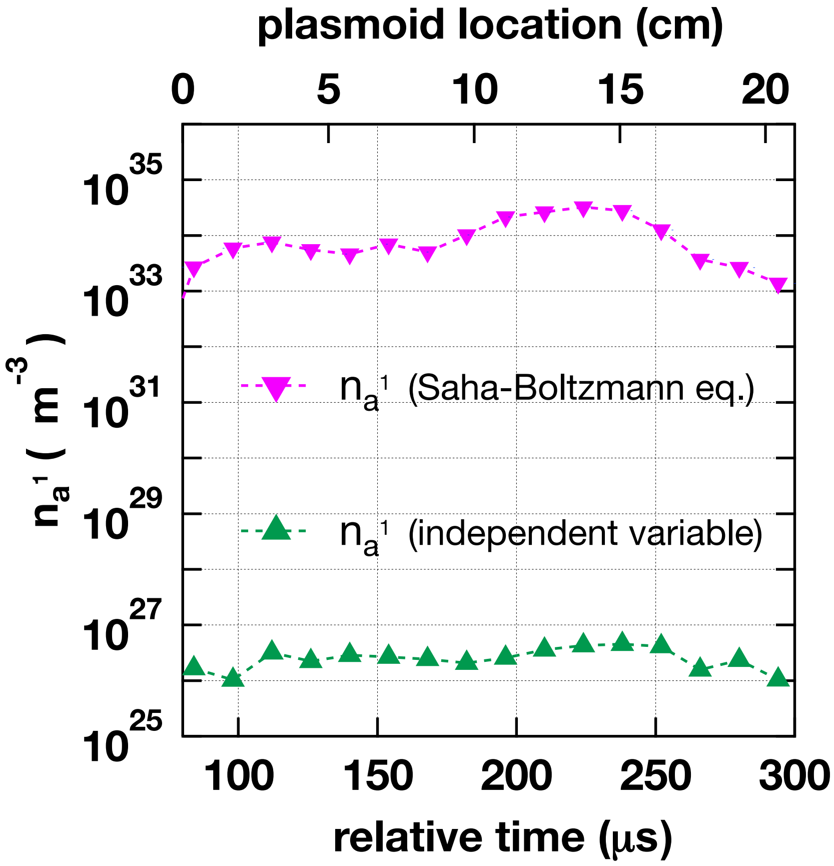

Figure 5.9: Comparison of the profile of n_a^1 when derived from the non-CLTE approach against for the profile of n_a^1 when calculated from Saha-Boltzmann equation with the fitting results of the non-CLTE approach as parameters

What the non-CLTE approach does is that it breaks the link between n_a^1 has with T_e and allows them to change independently from each other. This gives the spectral model more options to synthesize a spectrum, notably in regard to the slope the radiative continuum, and to the intensity of the emission lines.

Temperature parameter, case for a non-CLTE plasma: BYRON boundary

When T_e gets as low as what has been derived from this study, it is possible that the CLTE condition becomes invalid. Figure 5.10 maps the different phases the excited hydrogenic populations of a plasma can be in, in function of the their excitation p level and of what is referred to as the reduced electron density $lg(n_\mathrm{e}/z^7)$ for $T_\mathrm{e} = 1000$ K (source: reference [17]; p.10). This map is not entirely adapted to plasmas found in plasmoids as the given T_e is low. However, this configuration is convenient because the different boundaries are clearly visible. For example, if T_e is set to 1.0 eV (or 11605 K), the so-called BYRON boundary would have been closer to $p = 2$ and the lower right region of the map would have not been there. According to this BYRON boundary (cf. ref. [17] p.129)

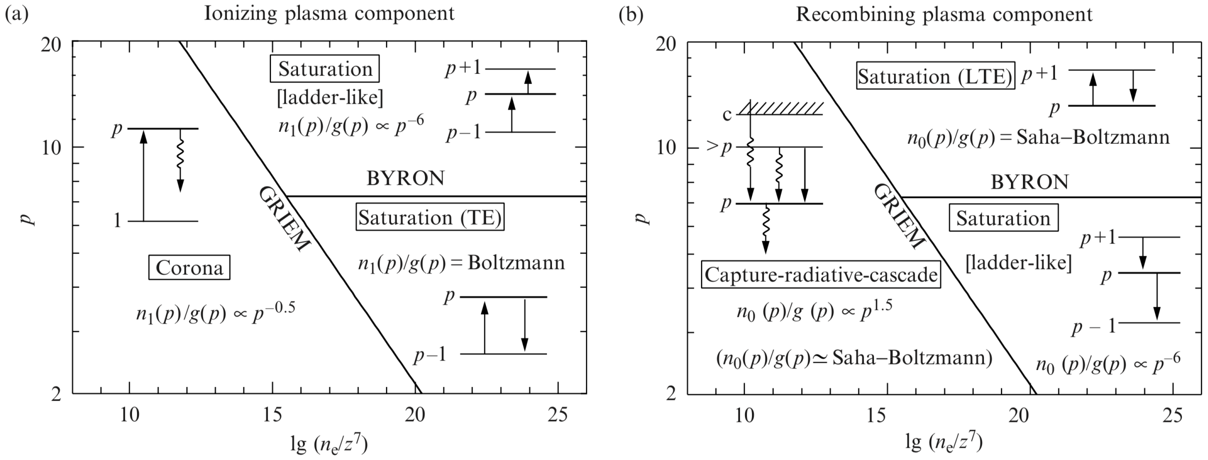

Figure 5.10: Plasmas conditions boundaries for recombining and attachment components [source: "Plasma spectroscopy", p.10 by T. Fujimoto (2004)]

When the profile of T_e derived from the non-CLTE approach is considered, the particles in the ground state of the plasmoid cannot be considered to be in LTE anymore (i.e. CLTE is not valid), because of the consideration of the BYRON boundary for the recombining plasma component. Indeed, the principal quantum number n_p^{BY} of the BYRON boundary is given by

$$n_\mathrm{p}^{BY} \sim \left(\frac{z^2 R}{3\, k_\mathrm{B} T_\mathrm{e}}\right)^{1/2}. \tag{5.13}$$

Applied to $T_\mathrm{e} = 0.4$ eV, $n_\mathrm{p}^{BY} \sim 3.7$. This result indicates that the analyzed plasmoid is within framework of the BYRON boundary, i.e. that the recombining plasma components under n_p^{BY} are not in LTE. Instead of CLTE, the so-called "sixth minus power distribution" has to be employed because of the ladder-like behavior of the recombining processes (cf. ref. [17]).

As such with $T_\mathrm{e} = 1.0$ eV, the BYRON boundary is set from $n_\mathrm{p}^{BY} = 2.1$, meaning that even in the passed cases of study, it would have been necessary to consider the plasmoids

as not being in CLTE. However, it is to be noted that eq. 5.13 is an approximation which tends to overestimate the value of n_{p}^{BY}, especially when $T_{\mathrm{e}} \leq 1.0$ eV.
Intrinsically, provided that the results found are correct, it would mean that more efforts need to be done to define the region near the BYRON boundary in the context of plasmoid-like plasmas.

Chapter 6

Conclusion

6.1 In regard to the observation method

Observation of the inner structure of ablation clouds

A new method to observe the visible light ($\sim$ 400-700 nm) emitted from hydrogen plasmoids has been developed. Optics composed of a plano-convex cylindrical lens and an optical fiber are used so that spatially-resolved spectral measurements (SRSM) of slices of plasmoids can be conducted. An observation system based on the present method has been installed in the Large Helical Device (LHD), and experimental data of the LHD 19th experimental campaign have been successfully collected.

Spatially-Resolved Spectral Measurements

The ability of the system to provide data favorable to the analysis of spectra emitted from actual slices of plasmoid has been confirmed. Data coming from an imaging device installed on the observation port, Thomson scattering data related to the electron temperature on the site of observation and knowledge of the magnetic field and heating configurations of the MCF device allow for the confirmation that conducting SRSM are possible.

6.2 In regard to the spectral analysis

A complete spectral model for ablation clouds

A spectral model for fuel pellet ablation cloud has been developed from and already existing one [12]. Two version of the model are considered. One version which uses a natively supposed approach which consists to consider that the plasmoid are in Complete Thermodynamic Equilibrium. The second version of the code does not suppose the CLTE has valid, and even has elements toward “freeing itself partially” from the LTE supposition altogether.

A fitting code based on a least-squares method has been developed and used. The procedure relies on a standard χ^2 minimization algorithm (albeit the χ considered is not a conventional one).

CLTE validity, a case for non-CLTE plasmoids

Fitting attempts conducted on spectra collected from the light emitted by the sixth and last plasmoid of a cherry picked LHD plasma discharge have been conducted. Results show that it is not possible to reproduce the experimental spectra using the CLTE approach, hence suggesting that the CLTE condition is not valid in the observed plasmoid. Fitting the spectra with a relatively good accuracy is however possible with the less strict non-CLTE approach.

If true, the “discovery” of a case of non-CLTE plasmoid in MCF plasma is a very rare if not unique event in the research community. A possible explanation for this is that the plasmoids observed in most studies where not pellet that reached the core plasma region of a MCF device, as was the case in this study. It might however explain why in a least one case [14], the spatial characterization of a plasmoid via a spectral model which considered a CLTE approach did not work as intended.

Another significant discovery of this thesis is the apparently very low electronic temperature which can be found in the central part of the observed plasmoid. Although a lower temperature at the center than at the edges is to be expected, what has not been expected is how low the temperatures derived from the data were.

If true, results found in this thesis would, at least, mean that the location plasmoids are when they are measured should be considered more carefully, at most, that an important re-thought of the inner structure of plasmoids.

Two papers [31] (published) and [32] (yet to be published, as of November 2018) present the results found with this study. The paper [31] is written about the SRSM capabilities of the observation system installed in the LHD and preliminary results about the possibility to derive the electron density profile of a plasmoid from this method. The paper [32] is written about the spectra fitting comparison between CLTE and non-CLTE approaches, and makes a case for the observation of a non-CLTE plasmoid in the plasma core region of the LHD.

6.3 Suggestions for future plans

Experiments

The field-of-view of the observation device being fixed, it has only be possible to study injection done near the core plasma. Although it is a very interesting area in term of magnetic field lines alignment and background plasma configuration, there are some disadvantages that could be addressed. Mainly, plasmoids seldomly reach the core plasma and when they do, they are mostly at the end of their lifespan (i.e. not stable phase).

Although non-CLTE plasmoids seem to have been observed at the core, it does not mean that it is the case everywhere in the vacuum vessel. Actually, most studies other than ref. [14] that conducted spatio-temporal diagnostics on plasmoids in regions other that at the core plasma of MCF devices found that CLTE was indeed valid. It would be interesting to test these findings with this experimental setup as well, in LHD, and elsewhere.

Observation system

The fixation system of the optical module could be improved. Especially, the alignment process of the optics of the spectroscopic device could be improved so that the alignment between the fiberscopes and the cylindrical lens can be controlled better.

The quality of the spectra recorded by the camera is weak. The camera has a problem of sensitivity when exposed to a signal with low brightness. This is especially problematic considering that the study of spectra of plasmoids involves section of very weakly emitting phases before and after a plasmoid is detected. Moreover, the response of the camera to light is not evident to clean. Although it reacts relatively linearly to the amount of light it receives, the sensor of the camera behaves strangely to it, with a wave-like pattern and slightly oscillatory signal.

The design of the box could also be slightly modified to correct some misalignments. The first one due to the shape of the box. Although it is of no real consequences, the angle the entrance wall has with the exit wall may impede the complete potential of the grating used.

Some minor additional modifications could be done, but what has been written here is, at least, the bulk of it.

Spectral model

In regard to the Stark-broadened lines, the MMM code is limited (cannot process higher that Balmer-δ because the found densities and temperatures are too high and low, respectively. Implementing another method of calculation, which could also take into account some kind of line asymmetry contribution (which is slightly observable in the results of the study) as well could be an interesting addition. Adding the contribution of the self-reabsorption effect for the lines, and eventually for the continuum would be wise. At this stage, Balmer-α cannot be studied efficiently with this system but, it is indubitable that some opacity effect intervene in the spectra. It may even be possible that Balmer-β is subject to it.

A very grazing work has been done in regard to the full consequences of the non-CLTE. Especially in regard to the so-called BYRON boundary and the way it could be exploited to simplify the spectral model. Maybe a more efficient approach than the one used here is possible, notably by what is referred to as the “sixth minus power distribution” mentioned in [17].

References

[1] L. Spitzer Jr, D.J. Grove, W.E. Johnson, L. Tonks, and W.F. Westendorp. Problems of the stellarator as a useful power source. Technical report, Princeton Univ., NJ Project Matterhorn, 1954.

[2] P.B. Parks, R.J. Turnbull, and C.A. Foster. A model for the ablation rate of a solid hydrogen pellet in a plasma. *Nuclear Fusion*, 17(3):539, 1977. https://doi.org/10.1088/0029-5515/17/3/013.

[3] C.A. Foster, R.J. Colchin, S.L. Milora, K. Kim, and R.J. Turnbull. Solid hydrogen pellet injection into the ormak tokamak. *Nuclear Fusion*, 17(5):1067, 1977. https://doi.org/10.1088/0029-5515/17/5/017.

[4] B. Pégourié. Review: Pellet injection experiments and modelling. *Plasma Physics and Controlled Fusion*, 49(8):R87, 2007. https://doi.org/10.1088/0741-3335/49/8/R01.

[5] B. Pégourié, V. Waller, H. Nehme, L. Garzotti, and A. Géraud. Homogenization of the pellet ablated material in tokamaks taking into account the ∇b-induced drift. *Nuclear Fusion*, 47(1):44, 2007. https://doi.org/10.1088/0029-5515/47/1/006.

[6] V. A. Rozhansky and I. Y. Senichenkov. On the ablation models of fuel pellets. *Plasma Phys. Rep.*, 31:993, 2005. https://doi.org/10.1134/1.2147645.

[7] Jyoti Shankar Mishra. *A study of pellet-plasma interactions using fast three-dimensional imaging in Large Helical Device*. PhD thesis, The Graduate University for Advance Studies, School of Physical Sciences, 2011. http://id.nii.ac.jp/1013/00002563/.

[8] H. Yamada, R. Sakamoto, Y. Oda, T. Hiramatsu, M. Kinoshita, M. Ogino, R. Matsuda, S. Sudo, S. Kato, P.W. Fisher, et al. Development of pellet injector system for large helical device. *Fusion engineering and design*, 49:915–920, 2000. https://doi.org/10.1016/S0920-3796(00)00342-2.

[9] R. Sakamoto, G. Motojima, H. Hayashi, T. Inoue, Y. Ito, H. Ogawa, S. Takami, M. Yokota, and H. Yamada. Twenty barrel in situ pipe gun type solid hydrogen pellet injector for the large helical device. *Review of Scientific Instruments*, 84(8):083504,

2013.
https://doi.org/10.1063/1.4816823.

[10] R. Sakamoto, H. Yamada, K.Tanaka K, K. Narihara, S. Morita, S. Sakakibara, S. Masuzaki, S. Inagaki, L.R. Baylor, P.W. Fisher, et al. Impact of pellet injection on extension of the operational region in lhd. *Nuclear fusion*, 41(4):381, 2001.
https://doi.org/10.1088/0029-5515/41/4/304.

[11] R. Sakamoto, H. Yamada, K.Tanaka, T. Tokuzawa, S. Murakami, M. Goto, S. Morita, N. Ohyabu, K. Kawahata, O. Motojima, et al. Observation of pellet ablation behaviour on the large helical device. *Nuclear fusion*, 44(5):624, 2004.
https://doi.org/10.1088/0029-5515/44/5/006.

[12] M. Goto, R. Sakamoto, and S. Morita. Experimental verification of complete lte plasma formation in hydrogen pellet cloud. *Plasma Physics and Controlled Fusion*, 49(8):1163, 2007.
https://doi.org/10.1088/0741-3335/49/8/005.

[13] T. Fujimoto and R. W. P. McWhirter. Validity criteria for local thermodynamic equilibrium in plasma spectroscopy. *Phys. rev. A*, 42(11), 1990.
https://doi.org/10.1103/PhysRevA.42.6588.

[14] G. Motojima, R. Sakamoto, M. Goto, A. Matsuyama, J.S. Mishra, and H. Yamada. Imaging spectroscopy diagnosis of internal electron temperature and density distributions of plasma cloud surrounding hydrogen pellet in the large helical device. *Review of Scientific Instruments*, 83(9):093506, 2012.
https://doi.org/10.1063/1.4751866.

[15] G. Cseh, G. Kocsis, P.T. Lang, B. Plöckl, T. Szepesi, G. Veres, and The ASDEX Upgrade Team. Pellet cloud characterisation, scaling and estimation of the material- and temperature distribution inside the cloud. *Nuclear Fusion*, 57(1):016022, 2017.
https://doi.org/10.1088/0029-5515/57/1/016022.

[16] G. Motojima, R. Sakamoto, M. Goto, H. Yamada, and LHD experiment group. Spectroscopic diagnostics for spatial density distribution of plasmoid by pellet injection in the large helical device. *Plasma and Fusion Research*, 5:S1033–S1033, 2010.
https://doi.org/10.1585/pfr.5.S1033.

[17] T. Fujimoto. *Plasma spectroscopy*, volume 123. Oxford University Press on Demand, 2004.
https://global.oup.com/academic/product/plasma-spectroscopy-9780198530282.

[18] V.Yu Sergeev, A.Yu Kostrukov, and S.A. Shibaev. Measurement of cloud parameters near hydrogen and deuterium pellets injected into t-10 plasma. *Fusion Engineering and Design*, 34-35:323–327, 1997.
https://doi.org/10.1016/S0920-3796(96)00533-9.

[19] B. V. Kuteev, A. Yu Kostryukov, and O. A. Bakhareva. Structure of luminous clouds near a sublimated hydrogen pellet. *Technical Physics*, 47(8):935–939, 2002.
https://doi.org/10.1134/1.1501670.

[20] E.H. Clark. Calculation of atomic data for fusion, 2009.
http://indico.ictp.it/event/a08151/session/6/contribution/3.

[21] T. Fujimoto. *Plasma Polarization Spectroscopy.* Springer Series on Atomic, Optical, and Plasma Physics, 2008.
https://www.springer.com/us/book/9783540735861.

[22] J. Glasser, J. Chapelle, and J.C. Boettner. Abel inversion applied to plasma spectroscopy: a new interactive method. *Applied optics*, 17(23):3750–3754, 1978.
https://doi.org/10.1364/AO.17.003750.

[23] Shimadzu diffraction gratings guide.
https://www.shimadzu.com/opt/guide/diffraction/index.html.

[24] Newport diffraction gratings guide.
https://www.newport.com/t/grating-physics.

[25] C. Stehlé and R. Hutcheon. Extensive tabulations of stark broadened hydrogen line profiles. *Astron. Astrophys. Suppl. Ser.*, 140(1):93–97, 1999.
https://doi.org/10.1051/aas:1999118.

[26] V. A. Soukhanovskii, A. G. McLean, and S. L. Allen. Near-infrared spectroscopy for divertor plasma diagnosis and control in diii-d tokamak. *Review of Scientific Instruments*, 85(11):11E418, 2014.
https://doi.org/10.1063/1.4891600.

[27] D. R. Inglis and E. Teller. Ionic depression of series limits in one-electron spectra. *Astrophysical Journal*, 90:439, 1939.
http://dx.doi.org/10.1086/144118.

[28] C.F. Hooper. Low-frequency component electric microfield distributions in plasmas. *Phys. Rev.*, 165:215–222, 1968.
https://doi.org/10.1103/PhysRev.165.215.

[29] J. Cooper. Plasma spectroscopy. *Reports on Progress in Physics*, 29(1):35, 1966.
https://doi.org/10.1088/0034-4885/29/1/302.

[30] M. Koubiti, Y. Marandet, A. Escarguel, H. Capes, L. Godbert-Mouret, R. Stamm, C. De Michelis, R. Guirlet, and M. Mattioli. Analysis of asymmetric dα spectra emitted in front of a neutralizer plate of the tore-supra ergodic divertor. *Plasma physics and controlled fusion*, 44(2):261, 2002.
https://doi.org/10.1088/0741-3335/44/2/309.

[31] G. Seguineaud, G. Motojima, Y. Narushima, and M. Goto. Spatially-resolved electron density measurement in hydrogen pellet ablation cloud. *Atoms*, 6(2):34, 2018.
http://dx.doi.org/10.3390/atoms6020034.

[32] G. Seguineaud, G. Motojima, Y. Narushima, and M. Goto. Non-clte spectral modeling approach for hydrogen pellet ablation cloud in the large helical device. *IOP Proceedings*, 2018∼2019?
yet to be published.